University of Leoben

Structural, Mechanical and Tribological Properties of (Ti,Al)N and (Ti,Al,Ta)N Coatings

Diploma Thesis

by

Jürgen Wagner

Leoben, 5th of March 2007

This work has been carried out in cooperation with CERATIZIT Austria G.m.b.H., CERATIZIT Luxembourg S.à.r.l. and Materials Center Leoben Forschung (MCL) at the Department of Physical Metallurgy and Materials Testing, University of Leoben, Austria

Acknowledgements

I would like to thank o.Univ.-Prof. DI. Dr. Helmut Clemens, Head of the Department of Physical Metallurgy and Materials Testing, for giving me the opportunity to carry out this work at his institute.

I also want to thank Ao.Univ.-Prof. DI. Dr. Christian Mitterer, Head of the Thin Film group at the Department of Physical Metallurgy and Materials Testing, for the supervision and expertise of this thesis.

My sincerest gratitude is due to my supervisor DI. Dr. Kerstin Kutschej for her guidance, for her endless patience and for her motivation, in times I needed it. And DI. Martin Pfeiler for his valuable support, for numerous discussions and for giving me the opportunity to work on this project.

Further I would like to thank Ao.Univ.-Prof. DI. Dr. Reinhold Ebner, Managing Director of the Materials Center Leoben, for giving me the opportunity to write this thesis within a MCL project.

Finally, I am very grateful to DI. Dr. Martin Kathrein at CERATIZIT Austria G.m.b.H, DI. Claude Michotte and MSc Mariann Penoy at CERATIZIT Luxembourg S.à.r.l. for their great support for this thesis.

1 Introduction

Materials for high-technology applications have to meet a huge number of requirements. In most cases, it is the surface of a component which has to sustain different loadings, not only of mechanical, but also of chemical and thermal nature. Moreover, surfaces have to fulfill electrical as well as optical properties. Also damage and furthermore possible loss of material starts from the surface of the product. Thus, for the specific adjustment of the surface properties, without changing the properties of the bulk material, thin film technology has been employed in a wide range of applications. Machining tools for cutting applications are just one example for high-technology applications, using thin films in the range of some microns to improve the properties of the contact area.

In this field, coating systems basing on nitrides or carbides are widely used, due to their superior mechanical properties. For a long time, the binary TiN coating system has been the basic hard coating for cutting tools. However, increasing requirements, like higher cutting speeds and longer lifetimes called for further improved coating systems. Alloying the element Al to the TiN system, resulting in the metastable $Ti_{1-x}Al_xN$ solid solution, has successfully been applied, due to its higher oxidation resistance compared to TiN. While TiN offers a sufficient oxidation resistance up to 500°C, the incorporation of Al increases this temperature to around 750°C, resulting in a higher wear resistance especially in high-speed, thus, high-temperature applications [1]. Commonly, these coatings are produced by physical vapor deposition (PVD) methods.

A high potential for improving the mechanical and thermal properties, as well as the tribological behavior has been found by alloying further elements (e.g. V, Si, Ta) to $Ti_{1-x}Al_xN$. V, for example, was found to improve the friction behavior and Si increases the microhardness [2][3]. Ta is also known to enhance the hardness of the coating and to improve the wear resistance and oxidation behavior, due to solid solution hardening [60].

In this work, the effect of different bias voltages applied during deposition on the morphology of the resulting film as well as the structural, tribological and mechanical properties have been determined. Furthermore, the influence of a small amount of hexagonal phase has been investigated by increasing the Al content. Therefore, two (Ti,Al,Ta)N coating types, differing in their Al content, have been deposited in an industrial scale cathodic arc deposition facility at different bias voltages. The mechanical, structural and tribological properties of the resulting films have to be

compared to conventional (Ti,Al)N coatings with the same Al/Ti ratios deposited by the same deposition conditions.

2 Deposition Fundamentals

2.1 General

Nowadays high technology applications often require materials, which offer properties that cannot be fulfilled by the bulk material alone. Thus, to satisfy such requirements surface modifications, resulting in properties differing from those of the bulk material, in order to protect the surface or just for decorative purpose are used. When a film is deposited onto the surface of the bulk material, the grown coating consists of a new material, whereas in case of e.g. in-diffusion of a material into a surface layer the layer consists of the parent and the added material. Thus, there is a wide range of applications, which call for adequate deposition technologies also concerning economical factors.
There are several ways to classify surface modification techniques, depending on the point of view. One possibility, given here, classifies into two main processes: *Wet Processes* and *Dry Processes.* Typical for *Wet Processes* is the transport of the deposition material from the material source to the substrate in the liquid state. These are technologies like

- Electroplating Deposition
- Electroless Plating Deposition
- Anodic Oxidation Deposition
- Sol Gel Deposition

including *Hot Dipping* (e.g. Galvanizing) processes which are popular in the automotive industry [4][5][6].

In *Dry Processes* the deposition material is transported in the vapor phase. Therefore the coating material has to be provided in the vapor state. Two basic ways of vapor deposition processes can be to distinguished [4]:

- Chemical Vapor Deposition (CVD)
- Physical Vapor Deposition (PVD)

The properties of a coating are not only defined by the properties of the material used, but also affected by the deposition process. Thus, all these processes have

their field of application and in order to enhance film properties, lots of research has been done. The PVD and the CVD processes are the most common methods to produce hard, ceramic coatings. Both techniques run three steps in the formation of the film. The first step is the synthesis or creation of the coating material by forming a vapor of the compound containing the film atoms (CVD), or the creation of a vapor phase via evaporation or sputtering (PVD). The next step is the transport of the vapor phase from the source to the substrate. Finally, a solid reaction product is formed on the substrate surface by condensation, nucleation and film growth [5].

2.2 The PVD Process

The basic PVD technique is not an invention of current time; it is already known since the late 19th century. Thomas A. Edison applied for a patent that described coating by evaporation in a vacuum by direct resistance heating or arc heating using a continuous current in the year 1884, which was granted in the year 1894. In the following decades, he also employed sputter deposition, which was used in the phonograph industry to deposit thin films of gold on wax phonograph cylinder masters [7]. The industrial importance of the PVD process has been tremendously increasing in the last decades, opening completely new applications.

2.2.1 General

PVD processes belong to the category of vacuum processes. The main applications of PVD films nowadays are found in optical, optoelectronic, magnetic and microelectronic devices. Moreover, PVD techniques are used for corrosion-preventing, heat-isolating, decorative and wear resistant hard coatings. The benefit of the processes is the wide range of materials, which can be used and the low process temperatures between 200°C and 500°C, independent from the deposition material [5][8]. Furthermore, there is a high process flexibility, concerning production parameters and performance of the process. Resulting from this, the microstructure of the film can be affected significantly. The achievable thickness of the layers reaches from Ångstrøm to millimeters under sputtering rates up to 75µm per minute. There are numerous PVD techniques to distinguish. However, there is a common way to categorize into three basic processes [5]:

- Evaporation
- Sputtering
- Ion Plating

Evaporation

In the evaporation process the coating material gets vaporized by heating up the material source (see Figure 2.1). There are numerous possibilities to do this, such as direct resistance, radiation, electron beam, laser beam or arc discharge heating. To avoid collisions of the atoms during migration to the substrate, the process is carried out under a pressure of typically 10^{-3} to 10^{-6} Pa, in line-in-sight process. Due to the temperature difference - the substrate is considerable cooler than the source - the atoms condense on the substrate surface [5][6][8].

Sputtering

In a sputtering process the surface of a solid material is hit by energetic particles, ejecting atoms and molecules from this surface. In the sputter process the source of deposition material, called target, is positioned in a high-vacuum chamber together with the substrate (see Figure 2.1). The bombarding species, mostly ions from heavy inert gases (e.g. Ar) is introduced to the chamber. An electric discharge is ignited by applying a negative DC voltage of 0.5 up to 5 kV resulting in a glow discharge between the cathodic target and the anodic substrate. If a high frequency voltage is applied (HF-sputtering) it is also possible to sputter not only electrical conductors but also semi- and non-conductors. The gas ionizes forming e.g. Ar^+ ions, which are accelerated towards the target, where they eject atoms, ions or clusters from the surface into the vapor phase. These particles migrate to the substrate surface where they are deposited. There are some possibilities to change the effectiveness of the basic sputtering process. Especially the method based on the interaction of electrical field and the magnetic field, the so-called *Magnetron Sputtering,* is of great industrial importance. Magnets, which are placed behind the cathode (target), affect the plasma by the generated magnetic field. This results in a more effective utilization of the electrons responsible for the increasing ionization density. The special benefits of magnetron sputtering are primarily the higher deposition rate and the large deposition area as well as the low substrate heating, compared to conventional sputtering [5][6][8].

Ion Plating

Ion plating represents a further development of basic vacuum evaporation and sputtering techniques. Similar to the evaporation process, the coating material is vaporized in a vacuum chamber. A working gas, typically Ar, is introduced, and a relatively high negative potential is applied to the substrate, a plasma is formed analogously to the sputtering process. A bombardment of the substrate with high energetic Ar^+ ions begins, thus the upper layers of the substrate are sputtered off. This procedure is used as a cleaning process, prior to the coating deposition.

Due to this ongoing bombardment during the following deposition process *resputtering* can take place. If the resputtering rate exceeds the deposition rate film growth is avoided. However, due to the high energy of the impinged ions the ion bombardment leads to a better adherence and modified residual stresses in the coating [5][6][8]. A schematic of the ion plating process is illustrated in Figure 2.1.
An important modification for all processes listed above, is the application of reactive gases (such as N_2 or CH_4) which lead to the deposition of nitrides or carbides. The process is known as *reactive deposition*. Thereby the reactive gas is introduced together with the working gas into the deposition chamber, where it is partially dissociated and ionized, due to the collisions with electrons. The activated gas now becomes incorporated in the growing film, forming a compound coating [9].

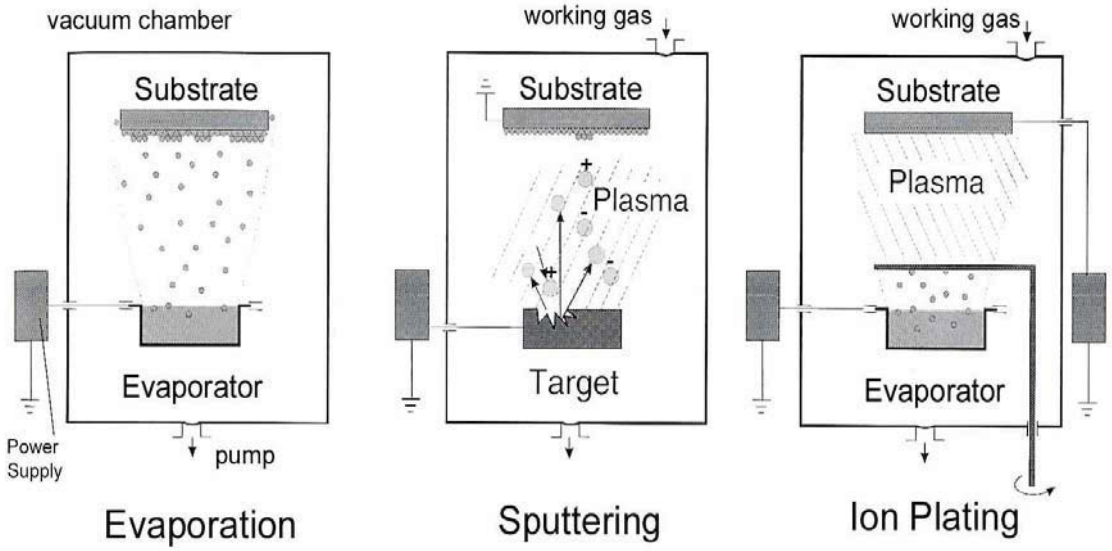

Figure 2.1: Schematic exposition of the basic PVD processes [8]

2.2.2 Gas Discharge

If electrical charges are transported in a gas or vapor via mobile charge carriers, namely electrons and ions, the phenomenon is called *gas discharge*. Thus, the gas discharge processes cover the generation of charge carriers, the movement of charge carriers in an electrical field and the charge carrier recombination. First of all, the charge carrier generation takes place. The most effective and fundamental mechanism is that neutral atoms are getting ionized, by inelastic collisions with accelerated electrons. Therefore, at least the ionization energy of the atom is required. To accelerate electrons, an electrical field is needed, which is generated by an external power supply. If the energy of the electron is not sufficient, i.e. less than the ionization energy, the ionization of neutral atoms is very unlikely. Furthermore, some charge carriers are removed by wall collision processes and recombination of positive and negative charge carriers. Both processes, the charge carrier generation and the charge carrier recombination, are working competing and simultaneously. If the generation process is predominant, the gas discharge is self- sustaining, otherwise additional charge carriers have to be inserted or generated and the process is referred to as dependent discharge [6].

To produce a gas discharge, electrodes are installed in an Ar atmosphere at a pressure of less than 10 Pa. There is a small number of free electrons existing, which origin either from photo effect or cosmic radiation. A voltage is applied and these free electrons cause a small current. With increasing voltage the energy of the electrons is increasing too, until the energy is sufficient to ionize atoms. When the collision process takes place, not only an ion is created, but also another electron. The positive ion now is accelerated towards the cathode and as a result of the impact further electrons (secondary electrons) are generated. These secondary electrons once more generate charge carriers on their way to the anode. Consequently, the ionization process causes a huge amount of electrons, which lead to a rapidly increasing current, while the voltage remains constant. This is called the *Townsend Discharge* and is visualized in Figure 2.2 [6][10].

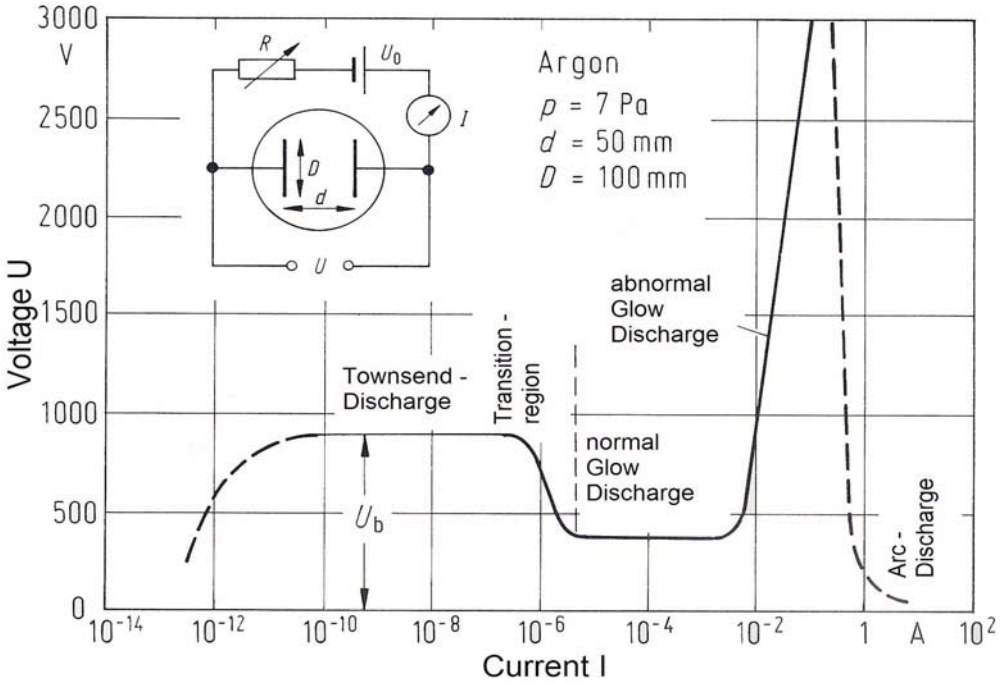

Figure 2.2: Current-Voltage characteristics of a gas discharge [6]

If the current is further increased, space charge effects favor the ionization and the voltage is decreasing. This is called the *normal glow discharge*. In this field the voltage as well as the current density is constant, while the current is proportional to the electrode area, which is covered by the glow discharge. If this electrode area is fully covered and the power is further increased, both, voltage and current increase significantly (see Figure 2.2). This field, the so-called *abnormal glow discharge,* is used for plasma assisted deposition processes. Both conditions, the normal as well as the abnormal glow discharge, are the so-called state of *plasma* [6], which is discussed in the following chapter.

When the current is increased to even higher levels, a transition from the glow discharge to an arc discharge takes place. Due to the high currents in an arc discharge, the electrons are predominantly thermally emitted from the cathode. This process is self sustaining and leads to high ionization rates, which make arc discharges very useful in ion based deposition processes [6][10].

2.2.3 Plasma

Plasmas are often employed in deposition techniques (PVD as well as CVD). However, the dynamics of film formation is not describable by equilibrium thermodynamics. A plasma is referred to as an ionized gas, containing equal numbers of positively and negatively charged carriers, as well as neutrals. Plasmas are in average electrically neutral, thus so-called *quasi-neutral*. The negative charge carriers are primarily electrons and the positive charge carriers are ions from the working gas. The mass difference of electrons and ions is of great importance. Since the electron mass is very low in comparison to the mass of the ions, the electrons are the dominant charge carriers in processing plasmas. The electron energy is typically in the range of 1 to 10 eV while the ion energy reaches only 0.02 eV to 0.1 eV. Due to the charged particles, the plasma is easily influenced by an external electric or magnetic field. Especially the electrons respond more quickly to external fields than the ions, because of their low mass. The mass difference is also the reason that the transfer of kinetic energy via elastic impacts of electrons and neutrals is nearly negligible. The ions and neutral particles consequently stay cold; thus low pressure plasmas are referred to as cold plasmas [17][9].

2.2.4 Cathodic Arc Evaporation

The Cathodic Arc Evaporation is a well known technology since many years and offers a wide range of applications. Films are used in machining tools as well as for decorative applications. Cathodic arc evaporation is based on the ion plating process. In an evacuated chamber, the arc discharge takes place between the cathodic deposition material (target), where high current is induced, and the chamber wall, which is on ground potential. The arc discharge generates the vapor to coat the substrate. The coating material is nearly completely ionized thus a high-energy plasma is formed (compare chapter 2.2.2). Applying a bias voltage between target and substrate offers the possibility to affect the velocity and thus the energy of impinging ions. Biasing the substrate influences film growth and as a result the properties of the coating [11].

The evaporated metal ions may be combined with reactive gas atoms. Thus, thin films of very high adherence and density can be produced; a great benefit of the cathodic arc evaporation process. The applications of arc evaporated films are coatings based on nitrides and carbides, especially for machining tools, such as TiN, (Ti,Al)N, (Ti,Zr)N, (Ti,C)N [6][10][19].

Cathodic arc spot

The cathodic arc spots present an important component in the cathodic arc evaporation process, thus they are discussed more in detail. The arc evaporates the deposition material, initiating local phase transformations from the solid state to an ionized plasma state. The arc is ignited between the cathode and the grounded chamber wall in vacuum e.g. via a trigger rod, which acts as an ignition electrode. Currents from 40 A up to more than 100 A are necessary, while the voltage ranges between 18 V and 30 V [8][19]. This concentrated high current forms locations of extremely high current densities in the order of 10^{12} A m^{-2} on the substrate surface [19]. These areas are called *arc spots*, which move fast and randomly (random arc mode) across the surface and create the vapor phase. The sensibility of the spots for magnetic fields enables to steer them when using a dynamic magnetic system, so that the cathode can be eroded homogeneously (steered arc mode) [8].

The ion bombardment on the cathode surface is concentrated on small areas, i.e. the elevated points of the surface roughness. Due to the electric field concentration on these exposed peaks, enhanced electron emission takes place. This causes a fast increase of temperature on the particular peak until a certain temperature is reached, and the "micro tip" is evaporated. A small crater, the so-called arc spot, is released on the surface and on its walls a melted phase is formed due to the extremely high temperatures. The crater has a power density of up to 30 W/μm^2, when the diameter is about 10 µm. Thus, the ionization rate of the plasma is increasing and the vapor pressure raises up to 200 bar, so that the plasma is accelerated into the chamber space. This is called the *plasma jet*. The velocities of the directed ions are supersonic and the corresponding energies range between 20 eV for light elements and 200 eV for heavy ones. This high ion energy is responsible for the different properties of films deposited by cathodic arc evaporation technique compared to other processes [8][19].

During this erosion process, the diameter of the cathodic arc spot is increasing and after about 5 to 40 ns, depending on the cathode material, the power of the arc and the applied magnetic fields, a critical diameter is reached. At this critical size, the power density is not able to maintain the arc-plasma any longer. Meanwhile, the molten phase piles up at the edges of the crater, due to the high plasma pressure and forms new micro tips. The height of these crater edges is about 5 up to 30 µm and the temperature of these micro tips is sufficient to generate a new arc spot. At a critical crater diameter between 2 and 50 µm, the speed of the arc spot results in 10 to 200 m s^{-1}. The series of arc spots is seen as the arc track (Figure 2.3) [8][17].

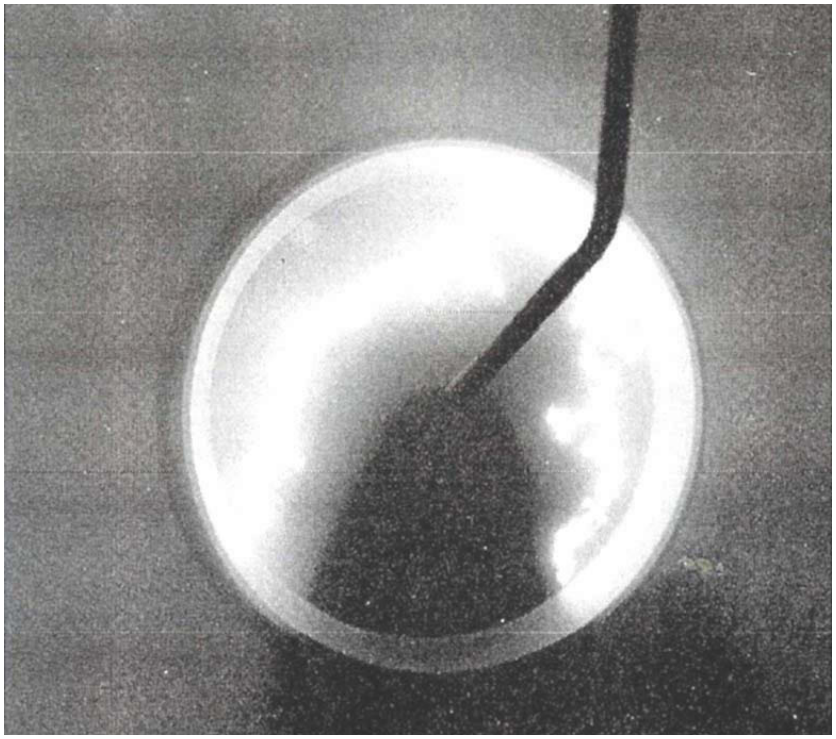

Figure 2.3: The arc track on a Ti cathode (random arc) [8]

Droplets

The cathode spots not only cause the fully ionized plasma but also macro-particles, which are also ejected into the chamber space and strike the substrate. The term macro-particles means particles that are much larger than ions, atoms and clusters. They are droplets and particles originating from the liquid phase on the crater walls. Due to the high plasma pressure in the crater, this molten material is placed at the edges of the crater and piles up (see Figure 2.4).

Figure 2.4: Particle formation at cathode spots [12]

These *droplets* are striped and accelerated up to a speed of 100 m s^{-1} by the plasma jet. It is reported that the size of these droplets ranges between < 0.1 up to 10 µm. Generally, the droplets are undesired in the cathodic arc evaporation process, because they end up as defects in the film. Size and number of the droplets depend

on the one hand on the vaporized elements themselves, more precisely on the melting point of these elements. For elements with low melting point, the droplet formation is favored, compared to elements with high melting point. On the other hand the arc current as well as the cathode geometry influences the droplet formation.
When running the process in the "steered arc" mode, an external magnetic field behind the cathode steers the arc in a closed circuit, thus reduces the droplet emission rate compared to the "random mode" [10][19][12].

Macroparticle filters

As mentioned above, the ratio of ions in the arc evaporation process is quite high and the plasma is nearly 100% ionized in contrast to other PVD processes, such as magnetron sputtering or electron beam evaporation, where neutral atoms form the deposition species. The small ratio of neutral vapor in the arc evaporation is generated by the undesired microparticles, coming from the liquid phase on the crater walls, as droplets. Therefore, the path of the plasma flow can be controlled by a magnetic field which leads to the ability to separate or remove the neutral droplets from the plasma stream [12][19].
In fact, there is a large number of filter types in use and numerous modifications of these types are reported. The type of *magnetic filters* is regarded as most common and represents an absolutely practicable technique. The magnetic filters represent a bent magnetic field, like the field in a curved solenoid, so that the electrons and the ions (thus the plasma) follow the curvature. The plasma now is guided out of the line-of-sight from the cathode's surface, while the macroparticles move along their almost straight path. This effect leads to the separation of the droplets from the plasma stream. An example of a filter, working in this way, is given in Figure 2.5.

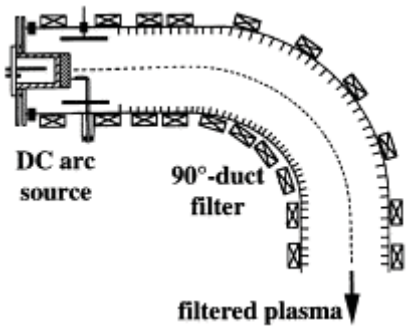

Figure 2.5: Schematic of a classic 90°-duct filter [12]

Beside the magnetic macroparticle filters, other techniques have been explored, too. Some filter types work mechanically to block microparticles when using blades and shutters. Another type has been published, working as a centrifuge. Thereby the cathode rotates at a speed of up to 4200 rev./min. in order to discard the particles (see Figure 2.6). Although these systems made an impact, they seem to be not practicable for industrial applications in contrast to magnetic filter systems [12][19].

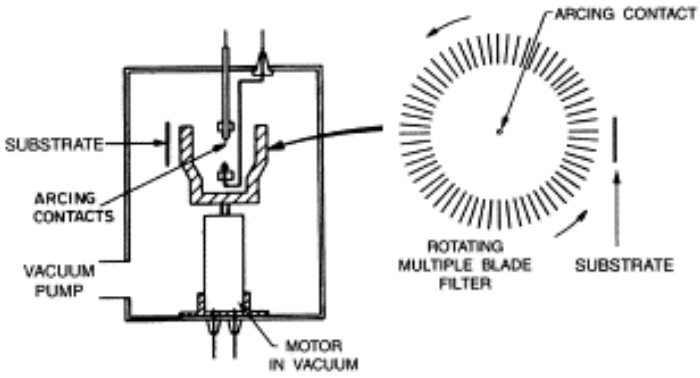

Figure 2.6: Rotating blade filter [12]

2.2.5 Deposition Parameters

Generally, PVD processes offer a large variety to design films, showing the required features. But not only the deposition method and the material used determine the film properties. Variations of the deposition parameters, listed below influence the microstructure and thus the properties of PVD deposited coatings [13][14]:

- Background and working gas pressure.
- Substrate temperature.
- Mass, energy, direction and flux of each species bombarding the growing film.
- Nature of the substrate material (e.g. chemical composition, surface roughness).

Thus, a brief overview about the main parameters, which can easily be controlled in PVD processes, is given.

Gas Pressure

There are different gas pressures (the background pressure and the partial gas pressures) to distinguish. In general, the background pressure in an evacuated chamber affects the concentration of impurities, which are incorporated in the film [15]. In deposition processes, the partial pressure of the inert gas as well as the reactive gas also influence the properties of films. For example, the influence of the nitrogen gas pressure during the deposition of (Ti,Al)N has been investigated by Lin et al. [16]. It has been reported that coatings deposited by cathodic arc deposition show a poor adhesion produced at low nitrogen pressures (< 1 Pa) and a good wear resistance is observed at nitrogen pressures of 5 Pa. Other investigations on sputter deposited (Ti,Al)N coatings also show a strong effect of nitrogen pressure on adhesion. In addition, it has been found that the nitrogen pressure strongly influences the Al content of reactive magnetron sputtered coatings. Due to increased coverage of the target with absorbed nitrogen, the deposition rate decreases with increasing nitrogen partial pressure. The effect of the working gas partial pressure on film morphology for magnetron sputtered coatings is generally shown in the structure zone model after Thornton, which is discussed in chapter 2.3.2. [1].

Substrate Temperature

In thin film deposition processes, elevated temperatures are used to enhance film adhesion, to control the morphology of films and to activate the reaction between metal and reactive gas in a reactive deposition process. In order to ensure good film conditions, theoretically, deposition processes could run at temperatures as high as the substrate can tolerate. The substrate temperature plays an important role during film growth (compare chapter 2.3.2). Generally, with increasing substrate temperature shadowing effects can be reduced by increasing diffusion, resulting in a denser morphology and a smoother surface [17]. Moreover, investigations on the influence of deposition temperature in cathodic arc deposited (Ti,Al)N coatings show that the deposition temperature promotes the formation of hexagonal (Ti,Al)N phase, resulting in a change of hardness [18].

Substrate Bias

Biasing the substrate means that a negative (with respect to the plasma) voltage is applied to the substrate, thus the energy of impinging ions can be adjusted. An increasing bias voltage leads to an enhanced ion bombardment. This bias voltage can reach up to tens of kilovolts (e.g. pulsed bias mode) [19]. When the ion energy is high enough, the ions are implanted into the surface of the substrate. This procedure is called *plasma immersion ion plating* (PIII) and leads to dense coatings with good mechanical properties, produceable at relatively low temperatures.

The effect of an applied bias voltage in sputtering processes is figured out in the structure zone model after Messier, which is further discussed in chapter 2.3.2. Also in case of cathodic arc evaporation, Messier's structure zone model explains the influence of the bias voltage, affecting composition as well as microstructure of the coating. Increasing the bias voltage leads to enhanced ion energy. The high energetic ion bombardment could lead to increased mobility of the atoms and hence to favored diffusion. Shadowing effects can be compensated and dense coatings are deposited even at low temperatures. However, at high bias voltages the bombarding ions tend to sputter loosely bond atoms from the surface. Thus, mainly strong bounded atoms dominate the adhesion mechanism [17].

2.3 Film Formation

2.3.1 Nucleation and Film Growth

The properties of a thin film are highly influenced by the microstructure of the coating. In the first stage of film formation, nucleation on the substrate surface takes place, which predominantly controls the microstructure of the films. Thus, the very first atoms that impinge on the surface are the determining factor for the following film formation and film adherence. When deposition material impinges on the substrate surface, the atoms loose energy to the surface and finally condense. Depending on the type and strength of interaction between these adatoms and the surface, a high density of nuclei (strong surface-atom interaction) is formed or, if the interaction is weak, widely spaced nuclei are formed [6][8]. There are three fundamental reactions occurring when an atom condenses on the surface (see Figure 2.7):

- the atom is bonded on the surface, forms clusters or nuclei, or accumulates on an already existing nucleus (adatoms)
- the atom is reflected promptly
- the atom is temporary bonded as an adatom, is able to diffuse a certain distance, until it is desorbed again (re-evaporation)

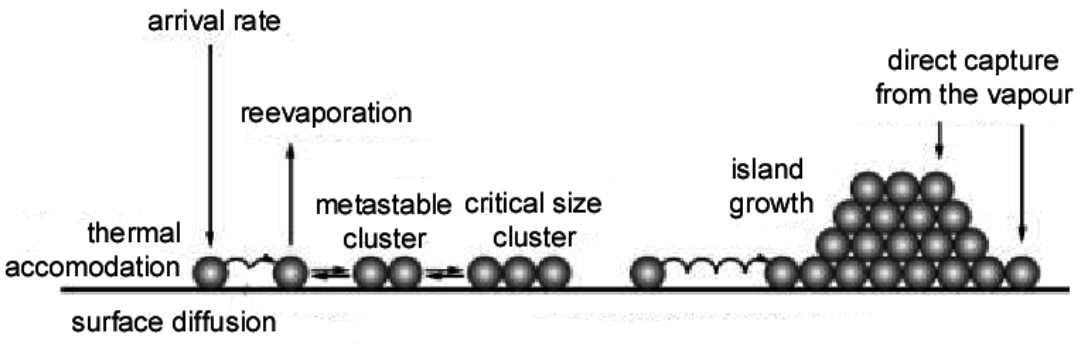

Figure 2.7: Fundamental reactions on the substrate surface [20]

The activation energies for diffusion and desorption as well as the impingement rate dominate these processes. The substrate temperature additionally influences the diffusion and the re-evaporation. If the impingement rate is small, an equilibrium between adsorption and desorption is established so that consequently too less particles are available for nucleation. At higher impingement rates the amount of atoms is sufficient to form clusters, reaching a critical size. This size can be formed by two or three atoms, so that nuclei can grow by diffusion or trapping of adatoms. Several nuclei now grow, get in contact with each other and coalesce. This leads to a continuous film growth [17].

During film growth, the energy of impinging atoms and the surface roughness play a decisive role. So called shadowing effects, caused by surface roughness, prevent a constant supply with coating material for the whole surface. There are some areas on the surface, which are shadowed from the particle stream by roughness tips or growing grains. These areas can only be filled by surface diffusion of the adatoms. Only atoms with sufficient kinetic energy are able to diffuse. For atoms with very high kinetic energy even bulk diffusion is possible. Moreover, the angle of incidence, the substrate temperature and mainly the pressure affect growth and morphology of the coating. Figure 2.8 shows the structure development during the evaporation process under various conditions. For a slightly varying flow direction and low temperatures, if no diffusion is possible, spherical nuclei grow and if coalescence occurs, a dense structure with columnar grains is formed (Figure 2.8a). For a parallel flow direction and low temperature, single free standing crystallites are formed. Shadowing effects, as described above, lead to an open, porous structure with high surface roughness (Figure 2.8b). Dense and smooth film structures are formed at higher substrate temperatures, due to the possibility of surface diffusion, even at parallel flow direction (Figure 2.8c). Figure 2.8d shows the structure, which is formed when repeated nucleation occurs. Which of these growing mechanism takes place, finally depends

on the activation energy for surface- and bulk diffusion, the surface roughness and the sublimation energy [21].

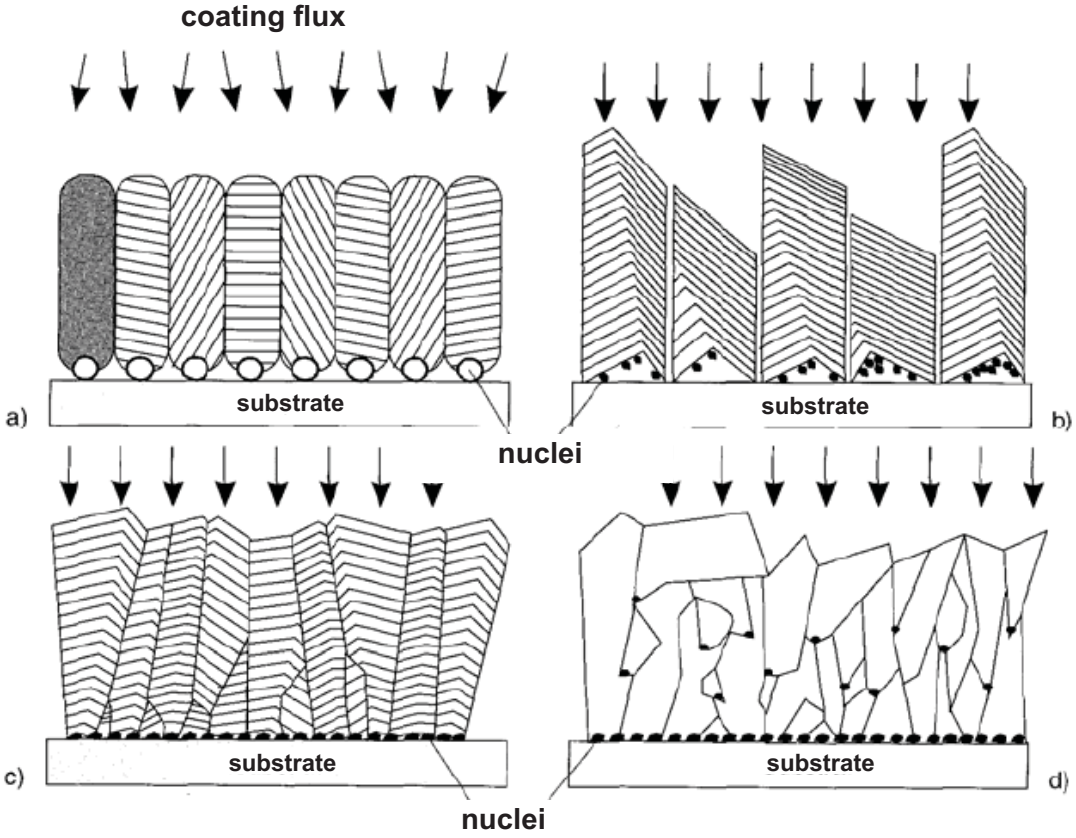

Figure 2.8: Structure development under various conditions [21]

2.3.2 Structure and Morphology Models

Generally, PVD coated thin films grow far away from thermodynamic equilibrium, thus the coatings have much more defects, like vacancies, precipitations, grain boundaries and dislocations. Basing on the influencing factors of shadowing effects, diffusion and desorption, several attempts have been made to quantify the parameters surface roughness, the activation energies for bulk and surface diffusion as well as the sublimation energy for modeling the growth process of films. Due to the strong correlation of these energies to the melting point of the material, the so called homologous temperature T_s/T_m is defined as the basis for *structure zone models*. Here T_m is defined as the melting temperature and T_s stands for the substrate temperature. *Movchan* and *Demchishin* found a correlation between structure and the normalized temperature T_s/T_m for several coatings, evaporated in

high vacuum [22]. Basing on these results, they published the first structure zone model (SZM) in 1969, which is displayed in Figure 2.9.

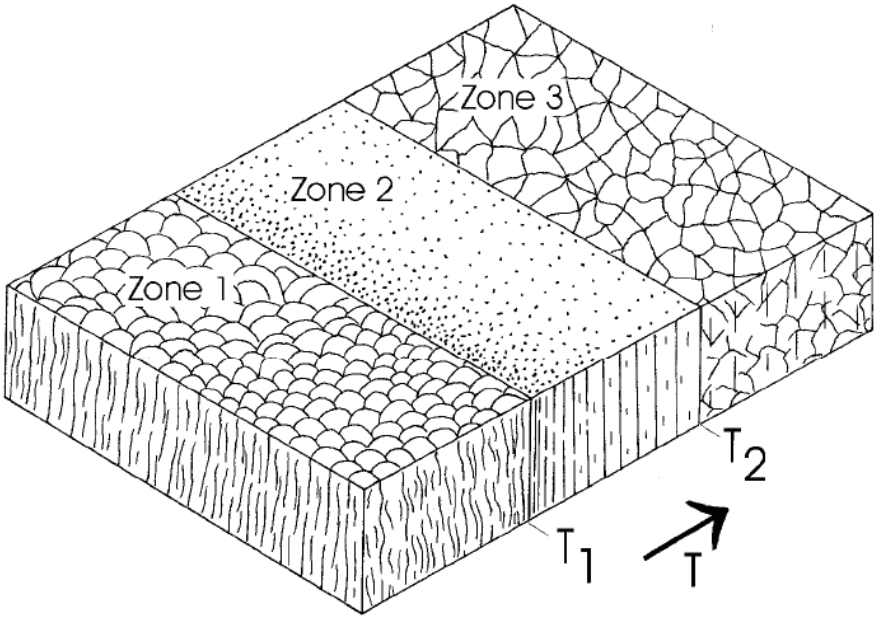

	Zone 1	Zone 2	Zone 3
Metals T_s/T_m	< 0,3	0,3 ... 0,45	> 0,45
Oxides T_s/T_m	< 0,26	0,26 ... 0,45	> 0,45

Figure 2.9: Structure zone model (SZM) by Movchan and Demchishin [22]

In **Zone 1** the substrate temperature is low, thus surface diffusion hardly occurs and shadowing effects can not be balanced. The structure is porous and is characterized by free standing columns with round tips. The dominating effect in **Zone 2** is the surface diffusion. The mobility of the atoms is increased by the temperature, therefore, a dense columnar structure is formed. The porosity decreases and the surface are smooth. With a further increase of temperature, bulk diffusion affects the growth of the film. Recrystallisation processes take place and a very dense structure is generated in **Zone 3**. In 1977, *Thornton* introduced another SZM, basing on the first one, for sputtered coatings (see Figure 2.10a). Thornton added a further axis to the diagram, which shows the influence of the pressure of the process gas (e.g. Ar). The zones are shifted to higher temperatures with increasing gas pressure. In the first zone, where temperatures are too low to allow surface diffusion, a small number of needle like crystals are developed. Due to the enhanced capture of vapor with increasing height, the needles are finally shaped like an upside down cone. Furthermore, he defined the **Transition Zone T**, which is characterized by occurrence of surface diffusion, so that shadowing effects are partly balanced. Thus

a denser structure, compared to Zone 1, is formed. Zone 2 and Zone 3 go widely along with the model of Movchan and Demchishin [21].

Both models only consider the thermally activated mobility of adatoms. Thornton's model indeed considers the gas pressure, but in deposition processes like sputtering or arc evaporation, the ion bombardment plays a more important role. Attributed to the formation of nucleation centers, smoothening the surface roughness or sputter-induced redistribution of film material the development of zone 1 is reduced. As a result, the transition zone is widened with increasing ion bombardment (adjusted by the bias voltage) at the expense of zone 1. Without ion bombardment the transition zone nearly disappears. This behavior is shown in the SZM of Messier et al., demonstrated in Figure 2.10b.

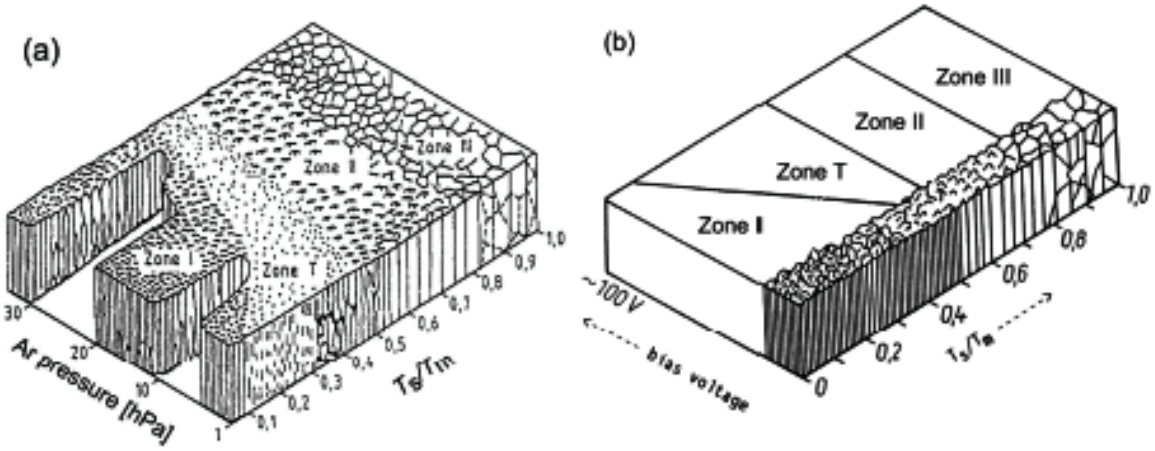

Figure 2.10: The modified SZM by Thornton (a) [23] and revised SZM by Messier (b) [24]

The width and boundaries of zone 2 and 3 remain the same. This is due to the fact that both zones are dominated by diffusion, while in the first zone as well as the transition zone shadowing dominates. All structure zone models describe film structures concerning substrate temperature, gas pressure, ion bombardment (bias voltage) [24]. Moreover, several other parameters like the position of the substrate in relation to the source (angle of incidence) or the pretreatment of substrates (e.g. cleaning) additionally influence the structure of films.

3 Tribological Properties

Tribology is an important field in thin film characterization, especially in case of wear resistant hard coatings. It deals with the fields of friction and wear but also the subject of lubrication. Tribology is generally defined as the science *of interacting surfaces in relative motion and related subjects and particles* [25].
As the result of tribological investigations two main parameters, the coefficient of friction and the wear coefficient can be determined. Both parameters are not material characteristics; they belong on a tribological system and can be independent from each other. Tribological systems consist of two defined materials (M_1, M_2) in a defined atmosphere. Elements involved are referred to as elements of the tribo system, for example velocity *(u)*, load (normal force F), geometry and environmental parameters like temperature *(T),* lubricant or wear debries (see Figure 3.1) [30].

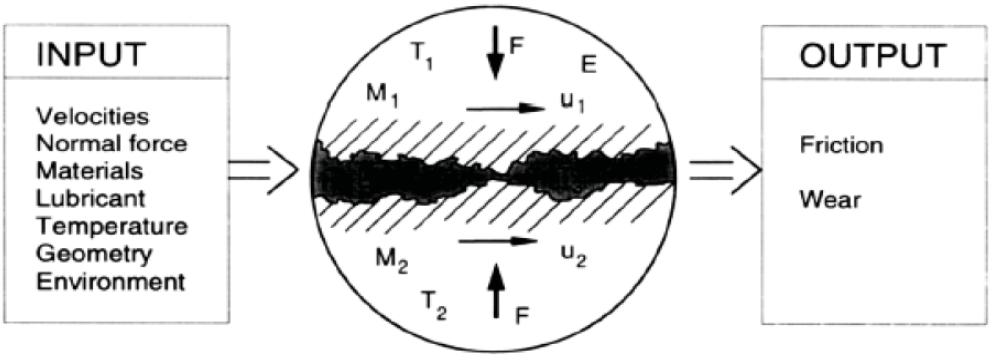

Figure 3.1: Illustration of a tribological system containing material contact condition and environmental input and output parameters influencing the tribo-physical/-chemical contact processes controlling friction and wear [30]

A very common method for testing a tribological system is the ball/pin-on-disc test. Thereby, the coefficient of friction is recorded during the whole test and both counterbodies (ball and disc) are investigated afterwards to determine the worn volume or the wear mechanism (see section 5.2.4).

3.1 Friction

Friction is understood as the resistance during the relative movement of two bodies in contact against each other [26]. There are a number of theories published about the mechanism of sliding friction. One common theory, by Suh and Sin [27] proposes three basic mechanisms responsible for friction. The first one is adhesion (Figure 3.2a) of flat areas of the sliding surface, which mostly plays a minor role. The second mechanism is ploughing, caused by hard wear particle (Figure 3.2b). Additionally, the deformation of asperities on the surface is the third mechanism which may influence the friction behavior (Figure 3.2c) [27][30]. These effects contribute to the friction coefficient which is defined as:

$$\mu = \frac{F_R}{F_N} \qquad \text{eq. [1]}$$

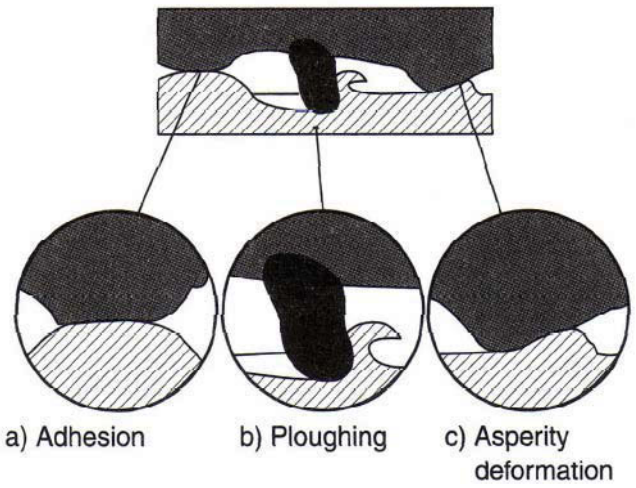

Figure 3.2: Three basic friction mechanism (a) Adhesion (b) Ploughing (c) Asperity deformation [30]

3.2 Wear

The loss of material from a solid surface by relative motion of two materials in contact is described as wear [30]. In general, four different wear mechanisms are distinguished:

- adhesive wear
- abrasive wear
- surface fatigue
- tribochemical reaction

Adhesive wear is understood as a selective welding of single points of the contact area. Due to the further motion, these points are sheared and break. If the welded area is strong enough to resist the further movement, the failure occurs in the softer material (Figure 3.3a).
Abrasive wear appears on one hand if hard particles are incorporated in one or both materials (e.g. surface asperities). This mechanism is called two-body-abrasion. On the other hand, abrasion may occur if hard particles freely move between the two surfaces. This mechanism is called three-body-abrasion (Figure 3.3b).
Surface fatigue occurs when the materials are exposed to permanent loading – unloading cycles. These cycles may cause the formation of subsurface- and surface cracks which result in stripping or breaking of the material (Figure 3.3c).
Tribochemical reactions base on tribological loading in a corrosive gaseous or liquid environment. One of the most common reactive species is oxygen (oxidative wear). If no motion occurs an oxygen layer is formed on the surface, which generally hinders further oxidation, thus acting as a protective layer. However, due to the movement, the oxygen film is worn away. Thus, the surface is not protected any more. Moreover, abrasive particles are formed, leading to enhanced abrasive wear (Figure 3.3d) [28] [29]. Wear is often quantified by Arhard's equation:

$$K = \frac{V_{tot}}{F_N \cdot s} \quad , \qquad \text{eq. [2]}$$

whereby K is called the coefficient of wear and V_{tot} is the total worn volume, load F_N as well as sliding distance s are parameters from the tribological test.

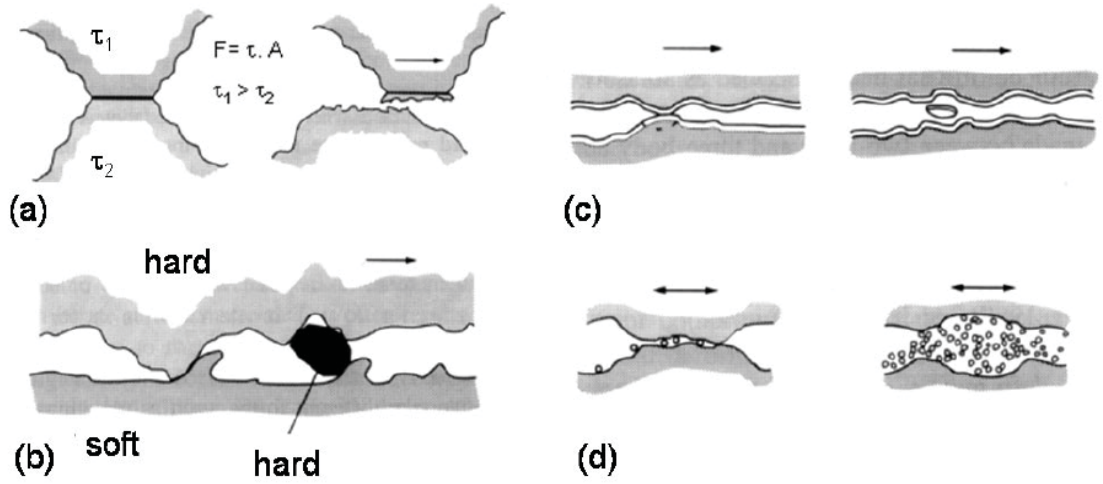

Figure 3.3: The four basic wear mechanisms: (a) adhesive wear, (b) abrasive wear, (c) surface fatigue, (d) tribo-oxidation [30]

Generally, a reduction of both values (friction and wear coefficient) is aimed to improve the tribological behavior and the lifetime of cutting tools [30].

4 (Ti,Al)N Fundamentals

Due to their mixture of metallic, ionic and covalent bondings, metal nitrides and carbides offer specific properties, which make them widely used for several cutting applications. In the last decades, especially TiC and TiN coatings were implemented in order to increase the lifetime of tools. Moreover, a further enhancement of the cutting parameter (e.g. higher cutting speed) is demanded to improve the productivity. Thus, there is a great interest in increasing tools lifetime and in reduction of downtime and thus enhanced productivity [31]. However, at high temperatures, arising in high speed applications, TiN hard coatings show a poor oxidation behavior caused by the formation of TiO_2 and thus a significant reduction of the mechanical properties. To enhance the properties of TiN films especially at higher temperatures, Al has been incorporated forming the metastable (Ti,Al)N phase. Al improves the oxidation behavior and the hardness and leads to a better thermal stability. But also the coefficient of friction is decreased by forming a thin Al_2O_3 layer especially at higher temperatures [1] [32]. In addition, a number of further ternary and quaternary coating systems have been designed in order to advance the basic TiN system. Ti-Zr-N, Ti-Al-V-N, Ti-V-N as well as Ti-Si-N or Ti-Al-Zr-N are only some few examples for coatings, which offer useful properties in different cutting applications [31] [33].

4.1 Microstructure

It has already been mentioned that the (Ti,Al)N coating system origins from the basic TiN system. TiN crystallizes in the face centered cubic (fcc) *B1* cell, also called *NaCl-* or *rock salt* - structure. In the equilibrium state, the ternary phase diagram (Ti,Al)N offers two phases occurring at 1000°C (see Figure 4.1a): the cubic *perowskite-type* phase (Ti_3AlN) and the hexagonal Ti_2AlN phase. Out of the ternary phase diagram, the quasibinary system AlN – TiN can be formed (Figure 4.1b) as an eutectic system where both phases, the fcc TiN and the hcp AlN, are separated over the whole temperature range showing a poor solubility limit of each phase in another [34][35][34].

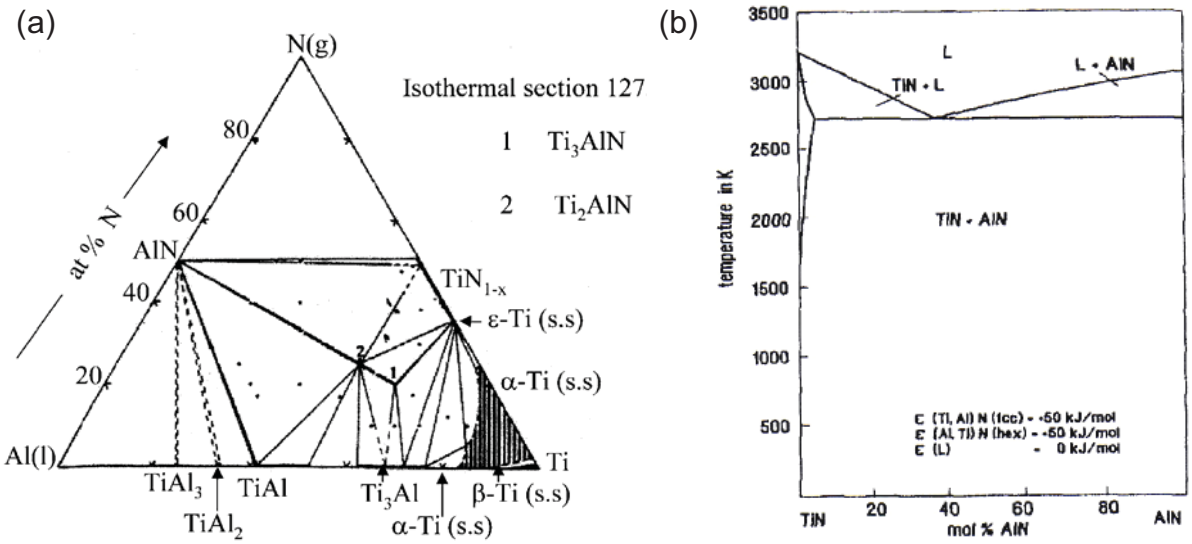

Figure 4.1: (a)Ternary phase diagram of (Ti,Al)N at 1000°C, (b) calculated quasibinary section of TiN – AlN [35]

It has already been mentioned that the films investigated within this thesis are deposited by cathodic arc evaporation. PVD processes are deposition techniques at low temperatures; hence, a thermodynamic equilibrium in the growing film is not likely. Moreover, due to high energetic (ion) bombardment during the deposition process, Al atoms can be incorporated in the cubic TiN lattice, resulting in a supersaturated metastable structure ($Ti_{1-x}Al_xN$). This phase is found at low and medium Al contents. However, at higher Al contents the hcp $Al_{1-x}Ti_xN$ phase is formed building a two phase structure, which deteriorates mechanical properties of the coating. Numerous investigations are published about the determination of the point where the crystal structure of $Ti_{1-x}Al_xN$ changes from fcc structure into the two phase fcc + hcp structure. The values range from 52% up to 70% Al content. In case of Al contents higher than 70 at%, a hcp single phase structure occurs. However, the optimization of the deposition parameters possibly shifts the precipitation of the hcp phase to higher Al contents, which might be an explanation for the broad varity of solubility limits published [36][37][38][46].

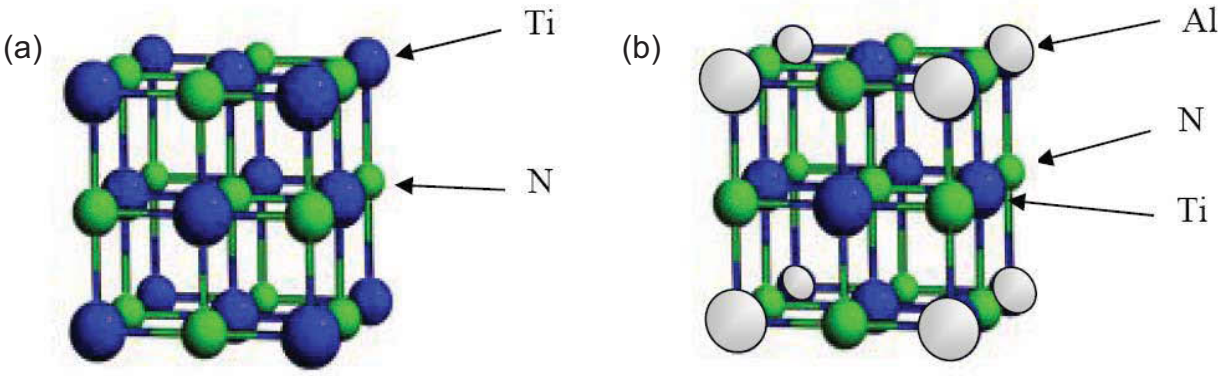

Figure 4.2: Schematic illustration of fcc crystal structure of (a) TiN, (b) $Ti_{1-x}Al_xN$ [53]

Figure 4.2a shows schematically the *B1 (NaCl)* structure of TiN. During the deposition process of (Ti,Al)N, some Ti atoms are replaced by smaller Al atoms, forming the fcc $Ti_{1-x}Al_xN$ cell (Figure 4.2b). The lattice parameter decreases with increasing Al fraction due to the smaller atomic radius of Al [53].

The Al fraction strongly influences the properties of the resulting film. If the coating is exposed to temperatures between 700°C and 1100°C, a two step phase transition ending in the equilibrium state takes place. In the first step, spinodal decomposition of the metastable fcc-(Ti,Al)N system into fcc-AlN and fcc-TiN takes place [39]:

$$\textbf{fcc-(Ti,Al)N} \rightarrow \textbf{fcc-AlN} + \textbf{fcc-TiN}$$

This mechanism has been proposed by Mayrhofer et al. [39]. The reason for this intermediate step might be the higher nucleation barrier of hcp AlN compared to fcc AlN, due to the larger atomic volume of the hexagonal cell and required incoherent grain boundaries with TiN. With increasing temperature, this step is followed by the transformation of fcc AlN into hcp AlN:

$$\textbf{fcc-AlN} \rightarrow \textbf{hcp-AlN}$$

Thus, the supersaturated solid solution decomposes completely in the stable equilibrium phases hcp AlN and fcc TiN, leading to a distinct change of the material properties.

4.2 Properties of (Ti,Al)N Coatings

4.2.1 Mechanical Properties

The hardness as well as the Young's modulus strongly depend on the Al content in the film. As Figure 4.3 shows, both mechanical properties are enhanced with increasing Al fraction up to a maximum value around 50 mol% Al. With further increasing AlN fraction, the hardness and Young's modulus rapidly decrease due to the formation of the hcp phase [40].

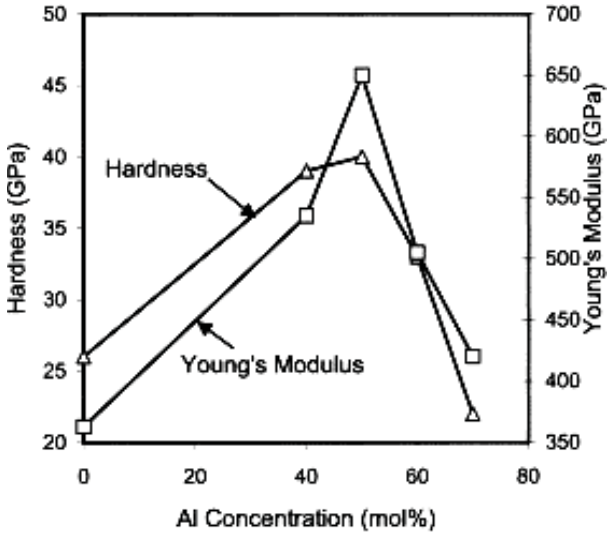

Figure 4.3: Hardness and Young's modulus as a function of the Al concentration in $Ti_{1-x}Al_xN$ films [40].

The reason for the increasing hardness from 20 - 25 GPa (for TiN) up to 30 - 35 GPa (for fcc $Ti_{1-x}Al_xN$) is the formation of the supersaturated solid solution due to the incorporation of Al in the TiN lattice [37][40]. The formation of the hcp phase tends to decrease the hardness values [1][37]. A further increase of hardness can be achieved by aditional alloying elements (e.g. Ta) in order to form solid solutions. Solid solution hardening is one of the basic hardening mechanisms in physical metallurgy. Atoms of two or more different elements can share one crystal lattice, if some criteria, like similar crystallographic structure, atomic size, electronegativity and valence state are fulfilled. Depending on the atomic size difference of the elements, there are different solid solutions formed. An interstitial solid solution is created, if the incorporated atom is significantly smaller (e.g. TiN) and a substitutional solid solution, when the atomic size of involved atoms is similar (e.g. (Ti,Al)N). Both forms of solid solutions can perform randomly or ordered [41]; the different models of solid solutions are illustrated in Figure 4.4.

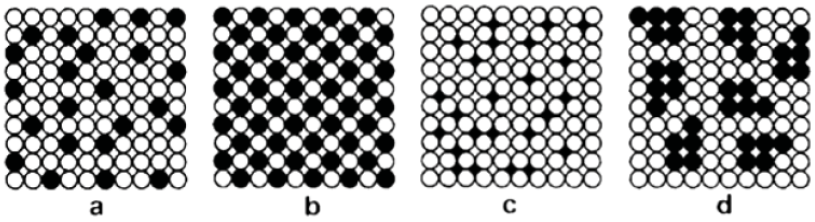

Figure 4.4: Illustration of four modes of solid solutions: (a) substitutional random, (b) substitutional ordered, (c) interstitial random, (d) solute clusters in solid solution [42]

The hardening mechanism itself bases on the interactions of the two different atom types. Strain fields are induced, due to the difference in atomic size, interacting with lattice strains in the vicinity of dislocation lines. Thus, a greater shear stress is required for dislocation movement than in pure metal. Moreover, the solid solution influences the shear modulus (G), due to changed binding energies. Thus, again the dislocation movement is reduced compared to pure metal. Additionally, there are chemical interactions (Suzuki effect) involved in the process of solid solution hardening [41].

The mechanism of precipitation hardening is also found in the field of thin films. Induced by adequate heat treatment, an alloy may decompose into two phases of different compositions. Nuclei are formed by thermal fluctuation, growing after reaching supercritical size and finally resulting in a phase composition according to equilibrium phase diagram (Figure 4.5a). Moreover, spinodal decomposition may occur, when small variations of concentration in an alloy gradually increase in amplitude. This spontaneous mechanism, so-called up-hill diffusion, is activated due to minimization of free energy (e.g. (Ti,Al)N, compare chapter 4.1). The equilibrium concentration is not immediately reached (Figure 4.5b). Both mechanism lead to the segregation of different phases, thus to precipitations. The interfaces of these precipitations can be coherent, semi-coherent or coherent in the matrix. Depending on the nature of these interfaces, there are different mechanism occurring, hindering the dislocation movement [41][43].

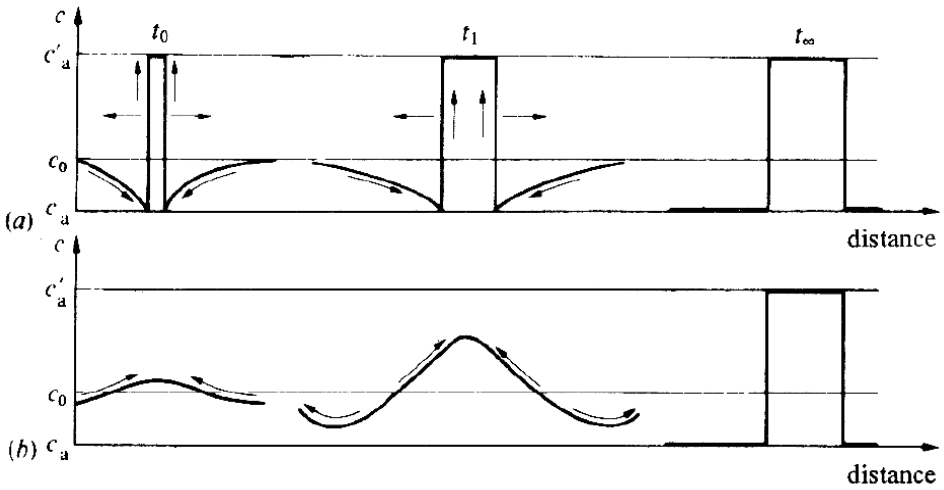

Figure 4.5: Two mechanism forming precipitates: (a) nucleation and growth, (b) up-hill diffusion (spinodal decomposition) [43]

Another way improving mechanical properties is found in decreasing the grain size. This hardening mechanism uses grain boundaries to hinder the movement of dislocations. Within grain boundaries slip planes are discontinuous and due to the different orientation of the neighbored grain, dislocations are unable to overcome these barriers. Hence, decreasing grain size leads on the one hand to increasing strength (hardness), on the other hand to increasing toughness [41]. Further decrease of grain size, to values lower than 100 nm, yields to nanocrystalline structure and the amount of grain boundary phase can exceed 50%. Beside the enhanced hardness, especially brittle materials show highly improved toughness, due to the mechanism of grain boundary sliding. However, if the grain size is too small, the hardness values decrease rapidly (see Figure 4.6) [44][45]. Super hard (Ti,Al)N coatings, reaching hardness as high as 47 GPa, are reported when a two-phase nanocrystalline (nc)-(Ti,Al)N/ amorphous (a)-AlN structure is produced [46].

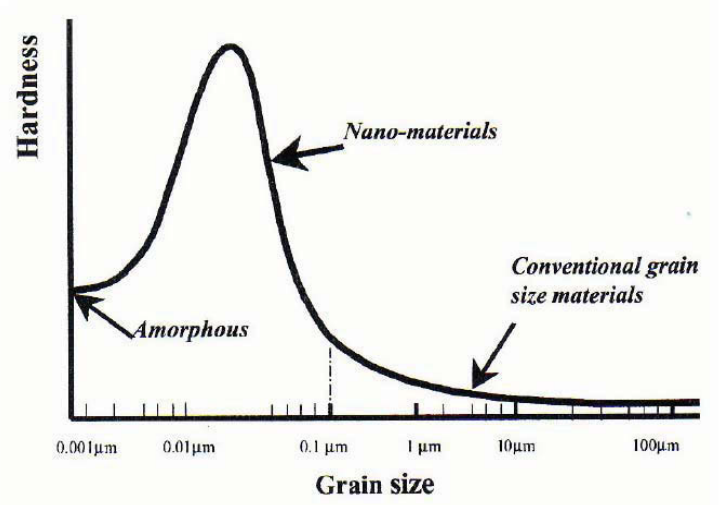

Figure 4.6: The dependence of hardness on the grain size [47]

4.2.2 Oxidation Behavior

Since hard coatings based on TiN are often used in conditions of high temperatures, like high speed cutting applications, an enhanced oxidation resistance is an important pre-requisite for increasing lifetime. TiN oxidizes at temperatures higher than 600°C, while coatings containing Al show superior oxidation behavior up to 800°C (see Figure 4.7) [1][48]. In case of TiN films an oxide layer of TiO_2 *(rutile)* is formed at temperatures above ~500°C. However, due to the large difference in molar volumes between TiO_2 and TiN the formation of a well covering layer is disabled and compressive strain occurs in the oxide. With increasing thickness of the oxide layer, the compressive strain increases and suddenly, the oxide peels off and the film is not protected any more [49].

The enhanced oxidation resistance of (Ti,Al)N films bases on the formation of a thin Al_2O_3 rich layer, which implicates two significant advantages. Al_2O_3 reduces the diffusion into or out of the film resulting in good oxidation resistance on the one hand and on the other hand in reduction of wear. Moreover, the resistance to oxidation can be improved with increasing Al content. It is reported that oxidation resistance in air up to 950°C is reached with Al contents of 60 at% - 70 at% [50][40].

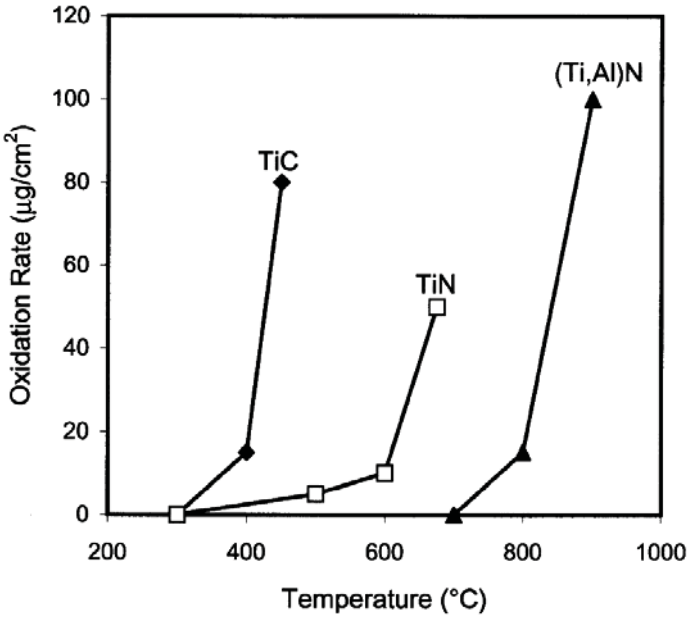

Figure 4.7: Oxidation rate of TiC, TiN and (Ti,Al)N coatings at different temperatures [48]

Numerous factors are influencing the tribological behavior of (Ti,Al)N coatings, such as microstructure, microhardness and the Al/Ti ratio. These factors are influenced by process parameters like coating composition, substrate bias and nitrogen partial

pressure [51]. In general, (Ti,Al)N coatings show superior results in cutting and drilling tests compared to other Ti based coatings such as TiN or Ti(C,N) [52][53]. The reasons for the better performance is explained by the formation of the surface Al_2O_3 layer, which reduces diffusion and oxidation wear (see above) [52]. Thus, high cutting speeds can be achieved [54]

4.3 Influence of Alloying Elements on (Ti,Al)N

It has been discussed, that Al has a distinct influence on TiN coatings. However, due to further alloying (Ti,Al)N, creating a quaternary system, further enhanced coating properties can be designed. On the one hand, the coefficient of friction can be improved. For TiN as well as for (Ti,Al)N coatings the friction coefficient against alumina is quite high in the range of 1 – 1.2, compared to Ti(C,N) with a value of 0.1 – 0.2 [1]. Vanadium has been known to form V_2O_5, Magnéli phase oxides, which offer easy shearable planes, acting as solid lubricants [55]. Thus, a Ti-Al-V-N coating concept has been created. Investigations at higher temperatures showed that the friction coefficient decreases with increasing temperature due to enhanced formation of V_2O_5 phases. At a temperature of 700°C a low friction coefficient of 0.27 is reached [2].
On the other hand, there is a great interest to improve hardness and wear resistance. Adding Cr or Y (Y causes grain refinement) to (Ti,Al)N coatings already showed success in improving mechanical properties [56]. Zr was found to stabilize the fcc TiN phase and forming an oxide layer in Ti-Zr-N systems, similar to Al in (Ti,Al)N. Furthermore, Zr alloyed coatings showed a better wear resistance compared to (Ti,Al)N, TiC or TiN [53][57]. Alloying the element silicon led to superior results in hardness as well as in thermal stability compared to TiN. The microstructure of Si containing coatings consists out of nanocrystalline (nc)-TiN surrounded by amorphous Si_3N_4. [3][58][59]. Also the quaternary system Ti-Al-Si-N has been investigated. Very high hardness values could be detected, due to grain refinement and prevention of grain boundary sliding [1]. Niederhofer et al. reported extremely high hardness values, when investigating nc-TiN/$TiSi_x$ films [58]. First investigations on Ta alloyed (Ti,Al)N coatings show the tendency, that Ta stabilizes the fcc phase, leading to higher wear resistance even at high temperatures. [60].

Thus, alloying elements influence the $Ti_{1-x}Al_xN$ coating system or (Ti,Al)N/(Ti,Al,X)N multilayer coatings. In most cases they improve mechanical and/or tribological properties. The varity of coating system is quite large, coatings specially designed for

certain applications are of great interest. Thus, further improvement of (Ti,Al)N coatings is the topic within this diploma thesis, where the influence of the Al content and the additional element Ta is investigated in detail. Moreover, the influence of the ion bombardment is investigated by changing the bias voltage during the deposition process.

5 Experimental

5.1 Coating Deposition

5.1.1 Substrate Material

Several substrates of different materials and geometries to meet the requirements of testing methods have been coated. For tribological tests, cemented carbide (cc) discs with a diameter of 30 *mm* and a thickness of 4 *mm* were used (grade *TSM33*). For the evaluation of microhardness as well as film thickness, cutting inserts (SNUN according to ISO 1832, grade *S40T*) were used. These samples were powder metallurgically produced by *Ceratizit Austria (CTA)*. Residual stress measurements have been carried out on single crystal silicon wavers, which had a rectangular shape of 21x7mm and a thickness of 0.38mm.

5.1.2 Deposition

The films have been deposited at *Ceratizit Luxembourg (CTL)*, using an industrial scale cathodic arc evaporation facility, termed *Balzers RCS*. A picture of the equipment is shown in Figure 5.1. The substrates have been fixed on a rotatable carousel. Two out of the six targets positioned inside the deposition chamber are pure Ti targets while the remaining four targets are TiAl or TiAlTa for the desired coating system. For this thesis, four different target compositions have been used for deposition. For each of these targets, the process bias voltage has been varied between –40 V and –160 V. The different runs concerning targets and bias voltage are summarized in Table 5.1

Table 5.1: Summery of the different targets and varying bias voltages

	Target composition [at%]			
BIAS voltage	**$Ti_{40}Al_{60}$**	**$Ti_{33}Al_{67}$**	**$Ti_{38}Al_{57}Ta_5$**	**$Ti_{31.7}Al_{63.3}Ta_5$**
-40 V	X	X	X	X
-80 V			X	X
-120V			X	X
-160 V	X	X	X	X

Figure 5.1: Balzers RCS industrial scale cathodic arc evaporation facility [61]

Coating Process

Prior to the coating process all cc - samples, which have been coated for this thesis, have been cleaned with ethanol before they were fixed on a magnetic sample holder, which has been placed on the rotatable carousel. The silicon samples were attached mechanically to the same holder.

The deposition process was divided into five steps

1. Evacuation
2. Heating
3. Ion etching
4. Deposition
5. Cooling

The schematic illustration of the process chamber and the position of the main components mentioned in the text below are seen in Figure 5.2. The process starts with the evacuation of the chamber to a pressure of 10^{-5} *mbar*. Afterward, the two mode heating process started. The first mode is heating up via radiation heaters,

which are installed inside the chamber (see Figure 5.2, Pos.14). The second and more efficient way to adjust the substrate temperature is via direct electron bombardment. In this process, an electron source is installed on top of the chamber. The carousel and consequently the substrates work as anode (Pos.12). The electrons are now accelerated towards the anodic substrate material. As a result of the electron bombardment, the substrates are heated up. For a higher efficiency, the electron beam is concentrated and steered by two magnetic coils, which are positioned on top and on the bottom of the chamber (Pos.6,8). Thus, the electron beam can be concentrated on top, in the middle or on the bottom of the recipient. In this way three levels in the recipient are heated alternately until the selected temperature is reached. After that, the ion etching process is activated. The recipient not longer works as anode. Another anode on the bottom of the chamber (Pos.4) is activated as a new anode and the recipient is the cathode. Argon is flowed into the chamber (Pos.3) resulting in the ignition of an arc. Ar^+ ions are created, and accelerated to the substrate surface which is hit by high-energy ions, sputtering off the very upper layer. This etching process constitutes the last step in cleaning the substrate surface before the deposition starts. At the beginning of the deposition run, two Ti targets (Pos.21) are ignited. The reactive gas (N_2) is introduced in (Pos.28) so that a thin TiN interlayer is deposited. After this, the four targets of the desired composition (Pos.16) are ignited and the main deposition process starts. An additional power supply is installed to apply the bias voltage to the substrates (Pos.13). The duration of the deposition run affects the thickness of the resulting film [62].

For all coating systems, a commercial deposition process at a substrate temperature of 450°C has been used. The deposition time has been chosen equal for all 12 systems lasting about six hours. As mentioned above, the bias voltage has been varied (see Table 5.1) representing one of the topics of investigations within this thesis.

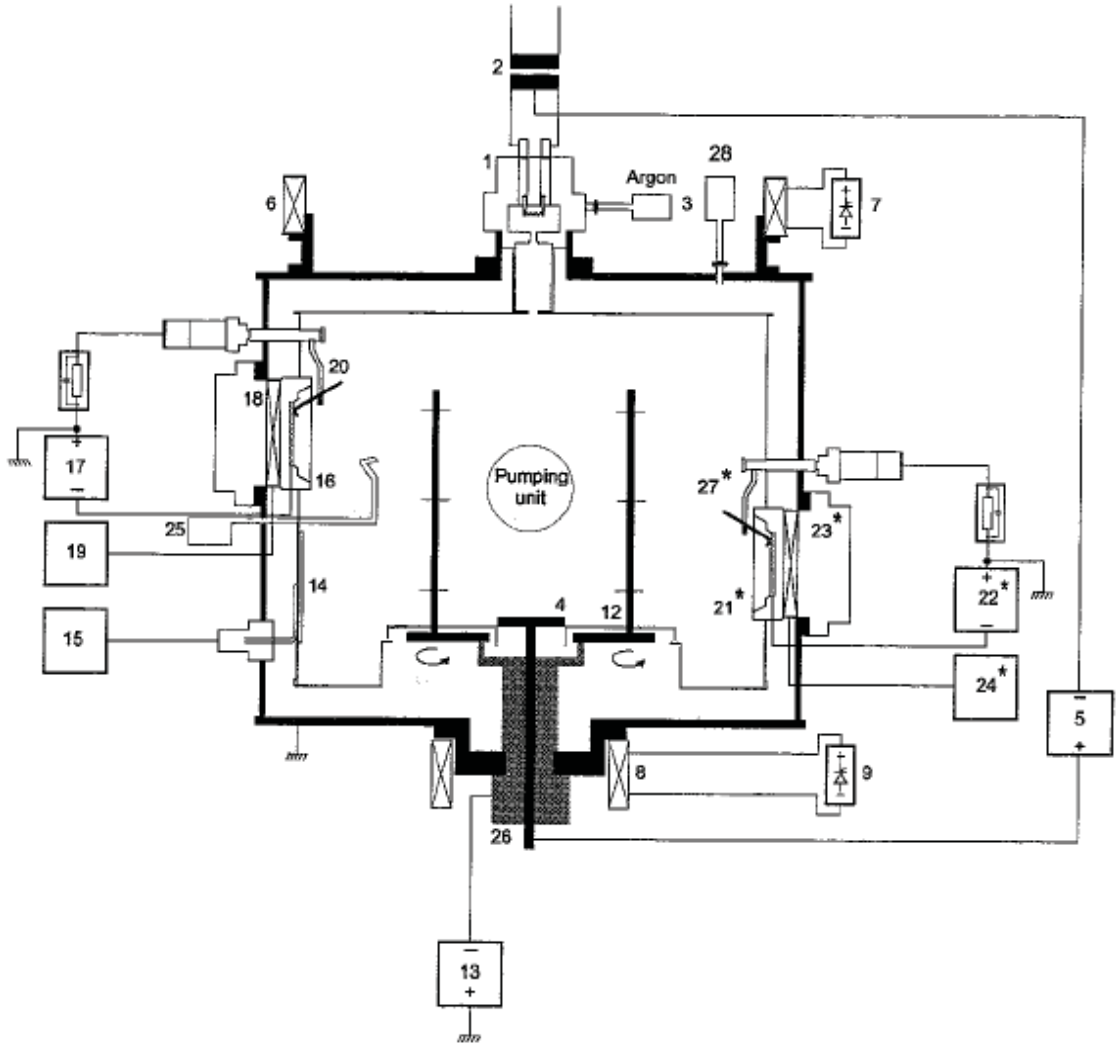

Figure 5.2: Main components of the process chamber of the *Balzers RCS* [62]

1) Ionization chamber, 2) Power supply for filament current, 3) Argon inlet, 4) Auxiliary anode for low voltage discharge, 5) Power supply for low voltage discharge, 6) Upper main coil, 7) Upper main coil DC current supply, 8) Lower main coil, 9) Lower main coil DC current supply, 12) Carousel, 13) Power supply for bias voltage, 14) Radiation heaters (total 10 elements), 15) Heating current control unit, 16) Arc sources (2, 3, 5, 6), 17) Power supply for arc sources, 18) Coils in the arc sources, 19) Power supplies for coil current, 20) Igniter (2, 3, 5, 6), 21) Arc sources (1,4), 22) Power supplies for arc sources, 23) Coils in the arc sources, 24) Power supplies for coil current, 25) Gas inlet distributor system, 26) Main feed through assembly (MFA), 27) Igniter (1,4), 28) Gas inlet for Nitrogen into the process chamber [62]

5.2 Coating Characterization

5.2.1 Film Thickness Measurement

The coating thickness influences film properties like residual stress and coating adherence, and represents an important parameter for further experiments, such as microhardness measurement. Thus, there are several methods for determining film thickness t_c. In this work, a Calowear® tester of CSM applying the so called ball-crater-test was used. A schematic view of this test is shown in Figure 5.3. A steel ball is rotating on the sample surface while a liquid diamond suspension as an abrasive wear medium is dropped on. As a result, a circular wear crater is created on the sample. If the wear crater is deep enough to reach trough the coating thickness, two concentric diameters appear (see Figure 5.3). The size of these outer (D_o) and inner (D_i) diameters can be determined in a light optical microscope. Thus, due to the mathematical correlation between D_o, D_i, the diameter of the ball *(D)* and the coating thickness t_c, the equation

$$t_c = \frac{D_o^{\,2} - D_i^{\,2}}{4D} \qquad \text{eq. [1]}$$

provides a good estimation for the film thickness [63].
Within this thesis, the steel ball diameter D used was 25.4 mm and a 3 µm diamond suspension was chosen as abrasive liquid.

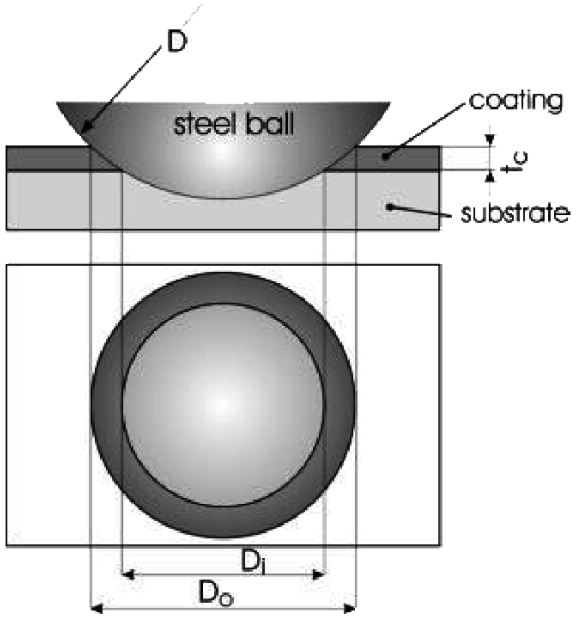

Figure 5.3: Schematic view of the ball-crater-technique [15]

5.2.2 X-Ray Diffraction Analysis (XRD)

An XRD analysis is a non-destructive material characterization method which offers a wide range for microstructural investigations (phase analyses, evaluation of residual stresses and determination of grain or particle sizes). Thereby, the sample is irradiated by an X-ray beam (K_0), in an angle θ to the sample surface. When the beam impinges on lattice planes (Q) of the sample, it is reflected. This diffracted beam (K) is detected at an angle of 2θ with respect to the incident beam. This mode is referred to as θ - 2θ scan (see Figure 5.4a). The maximum intensity at the detector at an angle 2θ arises if Bragg's law (eq. [2]) is fulfilled and constructive interference occurs.

$$n \cdot \lambda = 2 \cdot d_{hkl} \cdot \sin\theta \qquad \text{eq. [2]}$$

n……class of diffraction
λ……wavelength of X-rays
d_{hkl}…interplanar spacing of lattice plane (hkl stands for Miller indices)
θ……diffraction angle

These 2θ angle positions are characteristic for distinct interplanar lattice spacings d_{hkl}, thus can be related to crystal structures by comparing them with data from the Joint Committee on Powder Diffraction Standards (JCPDS). In this way, occurring phases in the coating can be identified. Peak height and broadness of the respective peak provide information about grain (particle-)size, and peak displacement is associated with residual stresses [64]. When thin films are investigated by XRD, undesired peaks from the substrate often appear. To avoid this phenomenon, GAXRD (Grazing Angle X-Ray Diffraction) can be employed (Figure 5.4b). In this modification of conventional XRD, the incoming X-ray beam (K_0) irradiates the sample in a small angle α of only a few degrees, which is kept constant, while the detector is moved along the 2θ circle. Similar to conventional XRD method, 2θ defines the angle between the outgoing beam and the elongation of the incoming beam [65].

In the framework of this thesis, GAXRD was used to specify different phases, which are present in the investigated coating systems. The analyses were carried out by *Ceratizit Luxembourg* employing a *Philips X'pert Pro* diffractometer. The scan was done from 20° to 140° using Cu-K_α radiation.

(a)

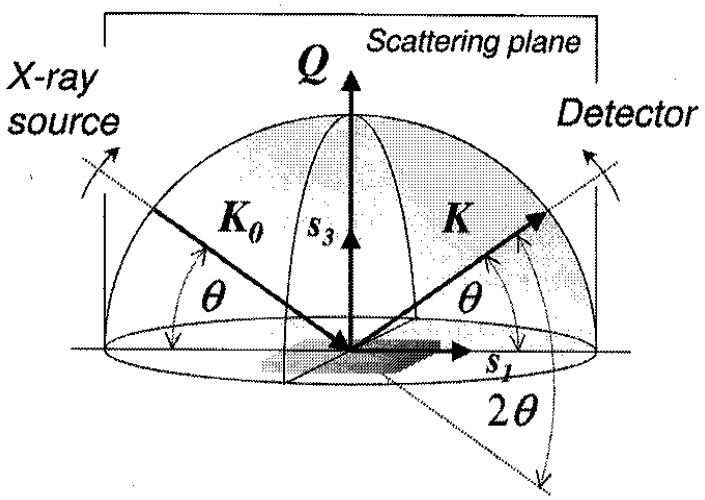

(b)

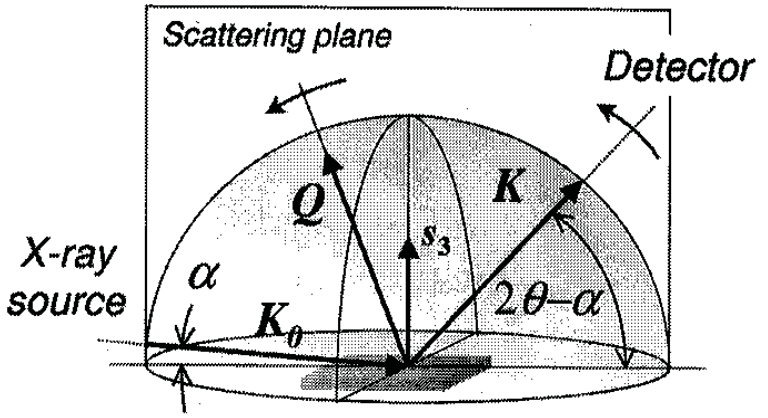

Figure 5.4: (a) Schematic representation of a θ - 2θ *scan* , (b) Schematic geometry of grazing incidence diffraction. The incidence angle α is kept constant during the measurement [65]

5.2.3 Evaluation of Microhardness and Young's Modulus

For the measurement of the microhardness, a Vickers microhardness tester (Fischerscope® H100C) was used. The instrument employs a Vickers pyramid out of diamond and measures universal hardness according to DIN EN ISO 14577. While indenting, the equipment measures the force F and the indentation depth h during the whole loading and unloading process resulting in the loading-unloading curve, shown in Figure 5.5 [66]. The microhardness can be calculated from the ratio of the load *F* to the created area of indent *A*, whereas this area is calculated from the indentation depth h_{max} and a constant, which is correlated to the geometry of the indenter.

$$HU = \frac{F}{A} = \frac{F}{26.43 \cdot h_{\max}{}^2} \qquad \text{eq. [3]}$$

HU contains elastic as well as plastic deformation, thus h_{max} is the indentation depth of elastic and plastic indentation. Therefore, the plastic indentation depth h_{min} is calculated from the loading–unloading curve (see Figure 5.5) and HU_{pl} is restricted to only plastic deformation. Thus, the plastic universal hardness is given as

$$HU_{pl} = \frac{F}{26.43 \cdot h_{\min}{}^2} \qquad \text{eq. [4]}$$

For the determination of Young's modulus an approximation, the so-called unloading modulus is calculated by

$$E^* = \frac{S[N/mm]}{\sqrt{A'}[mm]} \quad , \qquad \text{eq. [5]}$$

where S is the slope of the unloading curve at maximum indentation depth ($S = \partial F / \partial h(h_{\max})$) and A' is the surface under perfect elastic unloading ($A' = f(h_r)$) [67][68].

The microhardness measurement is quite sensitive to the surface roughness. Especially in case of cathodic arc evaporated coatings, which show a high surface roughness due to the formation of droplets, the samples had to be polished prior to the hardness measurement. For polishing, at first a 3 *µm* and afterwards a 1 *µm* diamond suspension was used so that roughness could be smoothed without influencing the film. Prior to the measurement, the calibration of the indenter has been performed on a sapphire plate. To avoid the influence of the substrate material on the hardness measurement, the indentation depth was limited to a maximum of 10% of the film thickness. During loading, the load was raised constantly within 20 seconds until the maximum indentation depth was reached. To ensure representative values for hardness and elastic modulus, 16 loading-unloading cycles (indents) were recorded for each sample. Since vibrations and shocks may cause a sudden change in slope of the curves, such curves were not taken into account. At least 10 curves were taken to calculate an average value for hardness and Young's modulus. The calculation was done computer controlled by the software WIN-HCU®.

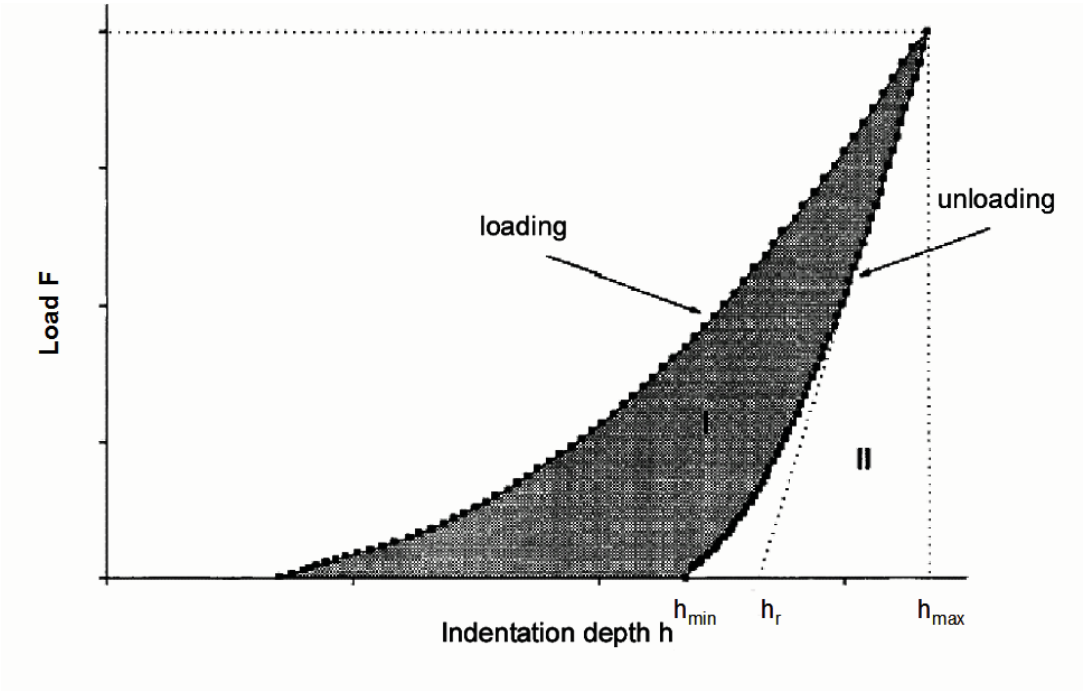

Figure 5.5: Recorded curve for one loading – unloading cycle of a microhardness indent.

5.2.4 Tribological Testing

Tribological tests are widely used to gain information about the friction behavior of thin films on the one hand, on the other hand to enable a subsequent evaluation of wear tracks and oxidation products.

Within this thesis, a ball-on-disc tribometer (*CSM Instruments High-Temperature Tribometer*) was used. A schematic illustration of the test facility can be seen in Figure 5.6. The sample, a cc disk (∅30 x 4 *mm*), is fixed by a locking ring on a rotating panel. An Al_2O_3 ball, acting as counter body, is fixed in a holder, which is loaded with a specific load. The tests can be carried out up to a temperature of 700°C. The radius of the wear track as well as the rotation speed can be adjusted. During the whole test, the software records the friction coefficient, which is calculated from the friction force, detected by a linear displacement transducer. The system is controlled by a software, which automatically stops the test when the default sliding distance is reached. The applied testing parameters used within this work are summarized in Table 5.2.

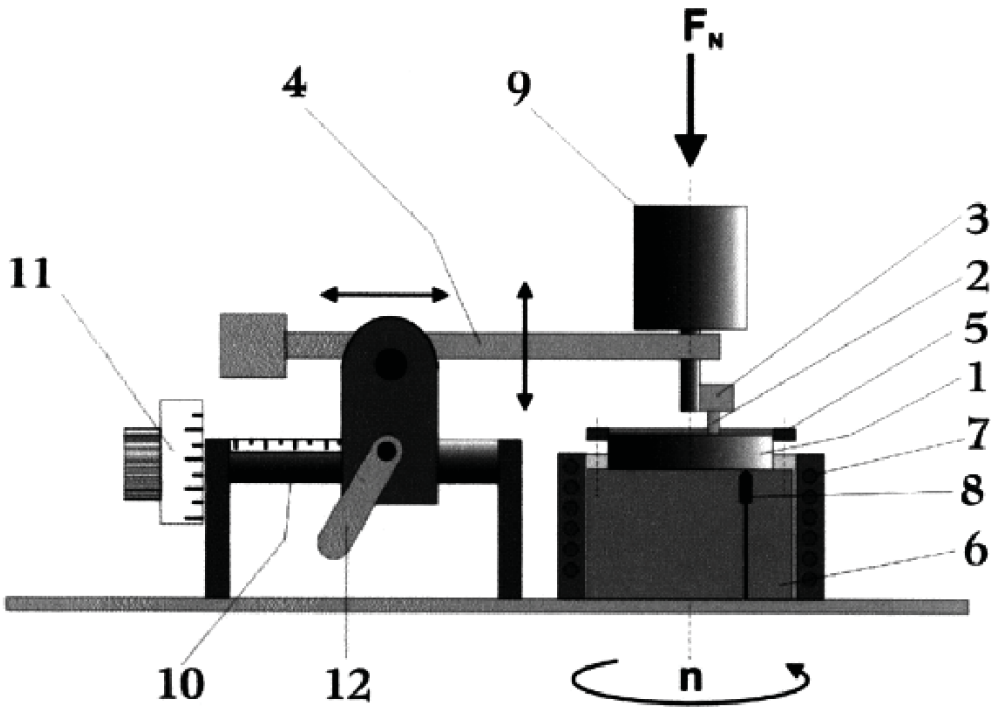

Figure 5.6: Schematic image of a CSM high temperature tribometer, 1) sample, 2) pin/ball, 3) pin/ball holder, 4) lever, 5) locking ring, 6) rotation cylinder, 7) resistance heating, 8) thermocouple, 9) cylindrical load, 10) variable axis for adjustment of radius, 11) adjusting screw for radius, 12) lock for the lever arm

Table 5.2: Parameters of the tribological tests

counter body	Al_2O_3
radius of wear track	5 mm
load	5 N
sliding distance	300 m
testing temperatures	25°C, 500°C, 700°C
linear speed	10 cm/s

5.2.5 Profilometer Analysis

The evaluation of wear tracks as well as the determination of surface roughness was carried out by a Veeco Wyco NT 1000 optical profilometer. An optical profilometer works as an interferometer, whose principle is shown in Figure 5.7. Light, produced by an illuminator, is split into two beams: one reference beam, which is reflected at a reference mirror and a second beam, which is reflected at the sample. Interference fringes occur when both beams are recombined at best focus and best contrast. A

number of these scans are made at positions above and below the focus and the interference fringes are scanned by a camera. Via the software, a 3D image of the surface is generated and 2D cross sections at distinct positions can be plotted. Using the recorded data, the software can calculate the worn volume (negative as well as positive) of the wear track. Since only some representative points of the wear track can be measured, the total wear volume of the whole track has to be calculated by geometric correlation. For these worn volumes the so-called wear coefficient *K* can be calculated.

For the determination of the wear coefficient, the partially worn volume was measured on five points for each wear track. After calculating the average partial worn volume and the total worn volume, the wear coefficient was determined. Moreover, different values for the surface roughness can be calculated [69][70]. Within this thesis, the average roughness R_a has been used.

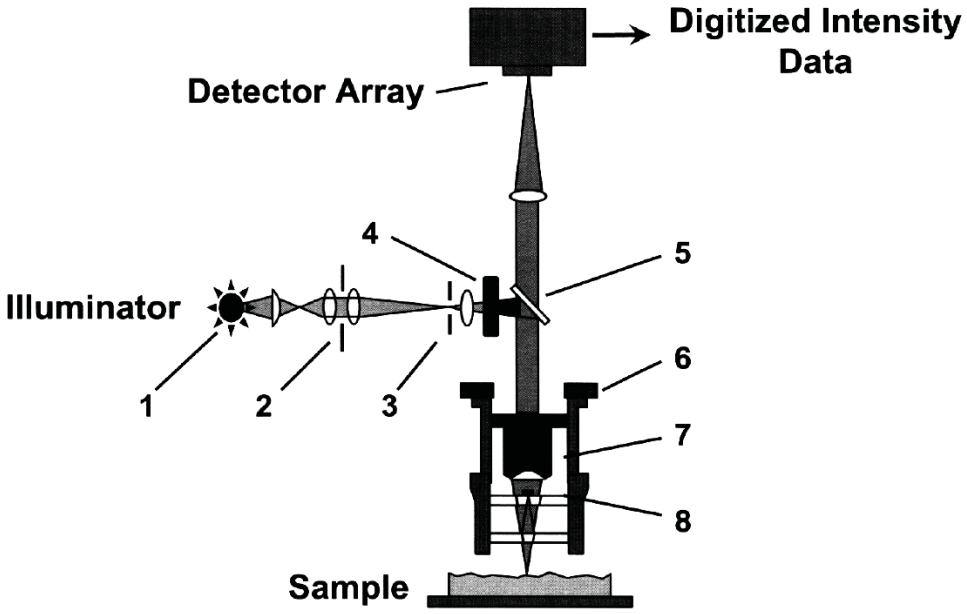

Figure 5.7: Principle beam path of the profilometer. 1) light source, 2) aperture stop, 3) field stop, 4) filter, 5) beam splitter, 6) translator, 7) microscope objective, 8) Mirau interferometer [70]

5.2.6 Further Investigations

After running tribological tests scanning electron microscopy (SEM) investigations have been performed to get high resolution micrographs of the wear tracks and to investigate the surface of the coating in the as-deposited state, as well as after tribological tests. For the investigations, a *Zeiss EVO50* was applied. Furthermore, an

attached energy dispersive X-ray analyses facility was used to gain qualitative information on chemical composition of the coatings and oxidation products.

Since the exact composition of the target and the resulting coating is not equal, due to the influence of several parameters, the compositions of the coatings have been determined by glow discharge optical emission spectroscopy (GDOES). The investigations were carried out at Ceratizit Luxembourg, applying a Horiba /Jobin – Yvon JY – 10000 RT facility.

6 Results and Discussion

Within this thesis, mechanical and tribological properties of (Ti,Al)N coatings, with two different Al/Ti ratios (1.5 and 2) were investigated. Moreover, keeping the Al/Ti ratio constant, Ta was alloyed. Each of these coating systems were deposited at different bias voltages (compare Table 5.1). Thus, the effect of three parameters, the Al content, the alloying element Ta and the bias voltage on the coating properties was investigated.

6.1 GDOES Analysis

In sputter processes, the targets contain the desired elemental composition, which determines the composition of the resulting film. However, the exact composition of the resulting film is influenced by several deposition parameters (e.g. the bias voltage). Thus, GDOES measurements were employed to determine the actual composition of the investigated films. Figure 6.1 shows the results of the GDOES analysis of the film compared with the target compositions of the coating systems without Ta. The N content has not been investigated by this measurement method. For the $Ti_{40}Al_{60}$ target (Figure 6.1a), the fraction of Al in the coating is lower than in the target whereas the Ti fraction is higher. A significant influence of the bias voltage can not be detected. For coatings deposited from the $Ti_{33}Al_{67}$ targets an opposite behavior can be observed (Figure 6.1b). The Al fraction in the coating exceeds the target composition at both bias voltages (-40V and -160V). The Ti content is lower than in the target and stays constant at a higher bias voltage.

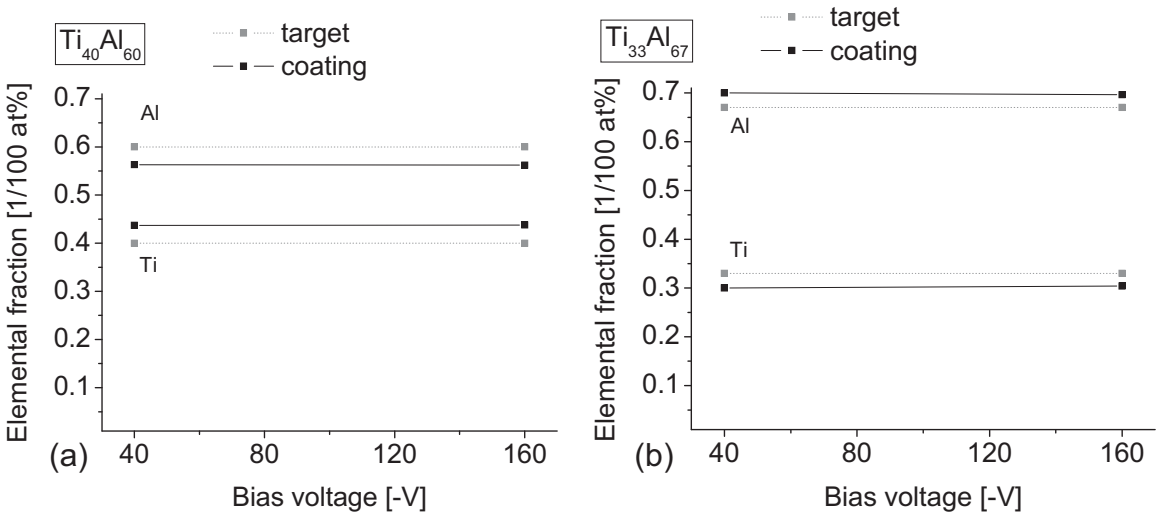

Figure 6.1: GDOES analysis of the films compared with the target composition of coatings deposited from a (a) $Ti_{40}Al_{60}$ target, (b) $Ti_{33}Al_{67}$ target.

In Figure 6.2, the results of the Ta containing coating systems are displayed. In both cases, the Al content was higher in the coating than in the target. A large deviation is observed for the coating deposited from the $Ti_{38}Al_{57}Ta_5$ target at -40V bias voltage (Figure 6.2a). The Al content in this film was 62.7 at% while the according target only consists out of 57 at% Al. With increasing bias voltage, the Al content slightly increases up to a value of 63.5 at% at -80V. In case of the coatings deposited at -120V and -160V, the Al content decreases, although, it is still higher compared to the target. The elemental content of Ti was lower in the coating than in the target, especially for the coatings deposited at -40V and -80V. Also for Ti, the highest deviation is observed for the coating deposited at -80V bias voltage, i.e. the coating shows a Ti content of 34.8 at% while the target consisted out of 38 at% Ti.

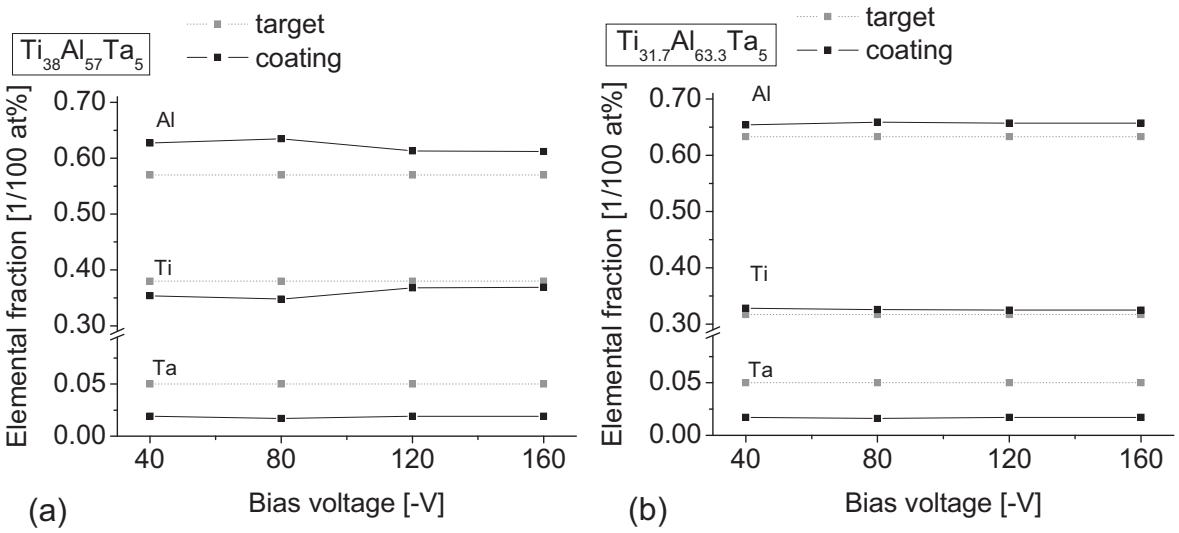

Figure 6.2: GDOES analysis of the films compared to the target composition of coatings deposited from a (a) $Ti_{38}Al_{57}Ta_5$ target, (b) $Ti_{31.7}Al_{63.3}Ta_5$ target.

In the $Ti_{31.7}Al_{63.3}Ta_5$ system, the Al content was also found to be higher in the coating than in the target, but it remains nearly constant over the bias voltage (Figure 6.2b). Nevertheless, a slight increase of Al can be detected in the coating deposited at -80V bias voltage, which exhibits the maximum value (65.9 at%) in this coating system. Different to the coating system with lower Al/(Ti+Ta) fraction ($Ti_{38}Al_{57}Ta_5$, Figure 6.2a) the Ti content is slightly higher in the coatings than in the targets. With increasing bias voltage, the difference of the Ti content between the coating and the target decreases and results in a deviation of only 0.8 at% at -160V. Moreover, in both coating systems the Ta content is determined to be much lower in the coating (in the range of 1.7 to 1.9 at%) than in the target (5 at%). The variation of the bias voltage during the deposition does not significantly influence the resulting Ta content in the films. However, for all coating systems the composition of the film

differs from that of the target. Therefore, within this thesis for the denotation of the investigated coatings their target compositions are chosen.

6.2 Coating Thickness

Although the process time was constant for all deposition runs, the film thickness differs from the expected calculated values of 4 µm. All coating thicknesses are in the range of 4.4 to 7.2 µm. The detailed results of the thickness measurement are shown in Table 6.1. The main reason for the deviation is due to the varying bias voltage. There is a slight tendency to lower film thicknesses with increasing bias voltage. This effect may be explained by enhanced resputtering of loosely bonded atoms in high bias conditions (see chapter 2.2.5) [17].

Table 6.1: Resulting film thickness for the different coating systems and bias voltages. The denotation of the coating systems refers to the target compositions.

	Film thickness [µm]			
Bias voltage	*-40 V*	*-80 V*	*-120 V*	*-160 V*
$Ti_{40}Al_{60}$	5.4			5.0
$Ti_{33}Al_{67}$	6.2			4.4
$Ti_{38}Al_{57}Ta_5$	5.2	4.8	5.3	5.2
$Ti_{31.7}Al_{63.3}Ta_5$	7.2	4.9	4.7	4.4

6.3 Surface Roughness

Films produced by cathodic arc evaporation generally show a high surface roughness, due to enhanced droplet formation compared to other PVD techniques, such as sputtering. This high surface roughness of the coatings may lead to a high friction coefficient [1]. For the calculation of the average roughness values, the roughness was measured by an optical profilometer on three different areas (120.8 x 91.9 µm) of each sample. A 3-dimensional image of an investigated area is shown in Figure 6.3, offering a large number of higher (red) and lower (orange) roughness tips.

The results of the investigated (Ti,Al)N and (Ti,Al,Ta)N coatings show similar roughness values for every Al/(Ti+Ta) ratio. Thus, no influence of the Al content or the incorporation of Ta could be detected. However, Figure 6.4 shows that the measured surface roughness value R_a strongly increases with increasing bias voltage for all coating system.

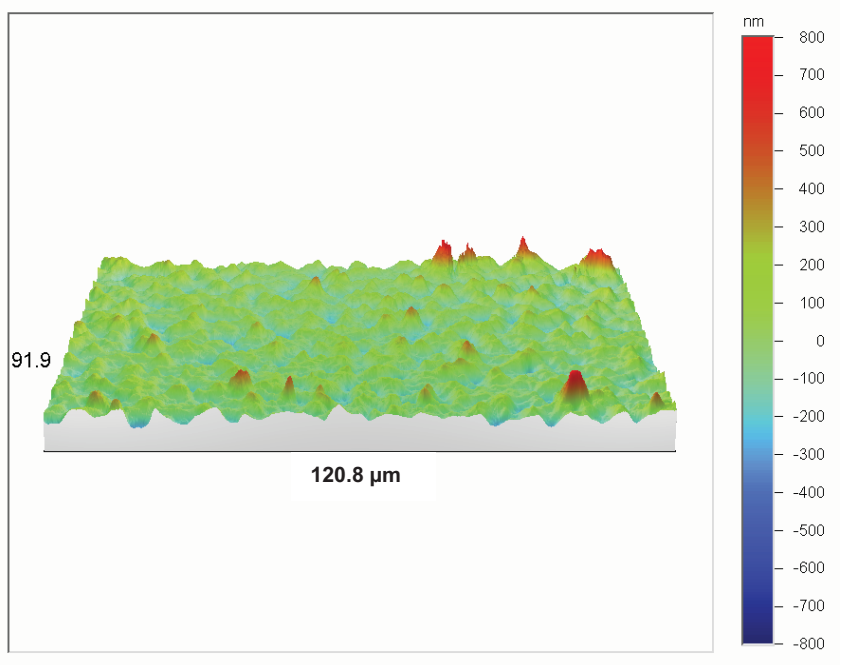

Figure 6.3: 3-dimensional plot of a surface area, investigated in the profilometer (target: $Ti_{40}Al_{60}$; applied bias voltage: -40V).

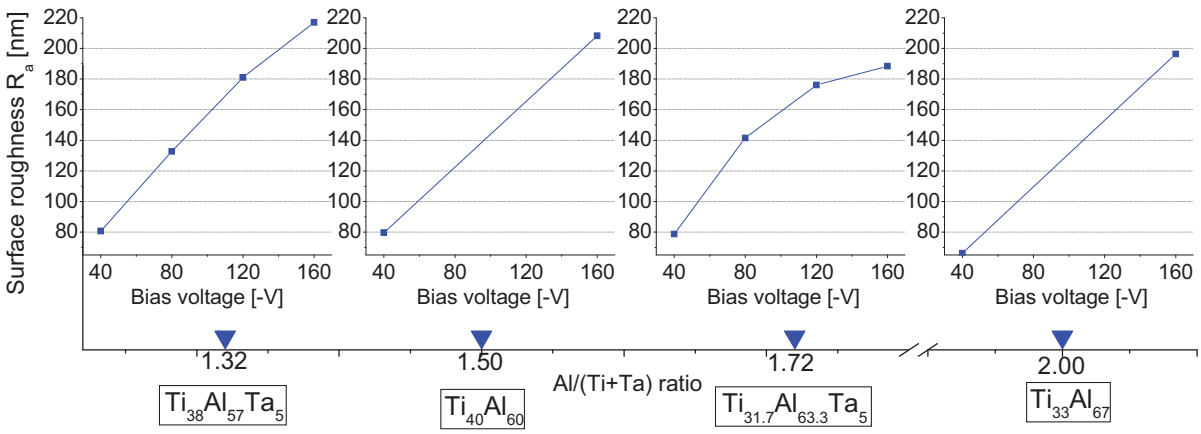

Figure 6.4: Surface roughness R_a, measured by an optical profilometer, depending on the negative substrate bias voltage for each coating system. The lower x-axis differs all four systems by the Al/(Ti+Ta) ratio. The denoted compositions are the target compositions.

The results of the roughness measurement in the optical profilometer show a completely different behavior than it could be expected. The influence of applied bias voltage has already been discussed in chapter 2.3.2. According to this, an enhanced ion bombardment (enhanced bias voltage) leads to a smoother surface. The reason for this deviation can be found in the average roughness value R_a. The measurement of R_a does not distinguish between peaks and valleys nor consider the spatial structure of the surface. Thus a great amount of droplets in average lead to a smaller value of R_a, because the average plane between all peaks and valleys is taken as ground level. Therefore, a smoother surface with single droplets leads to a higher average roughness due to a lower estimated basic level and resulting more pronounced height differences [71].

Thus, to gain more information about the surface morphology, the droplets on the surface have been further investigated by SEM. Analyses of the surfaces of all coating systems deposited at -40V and -160V bias voltage have been conducted (see Figure 6.5). The left row shows the coatings deposited at -40V and the right row at -160V bias voltage with increasing Al/(Ti+Ta) ratio. For all coatings deposited at -40V bias voltage, a great amount of droplets is seen, strongly decreasing for an applied bias voltage of -160V. Thus, the effect of smoothing the surface with increasing bias voltage is clearly seen. Moreover, both coating systems resulting from the targets with higher Al content (Al/(Ti+Ta) = 1.72 and 2.00) show a significant higher amount of droplets. Since the droplet formation depends on the melting points of the evaporated elements (compare chapter 2.2.4), the reason for this effect might originate from the higher content of low melting Al compared to Ti and Ta.

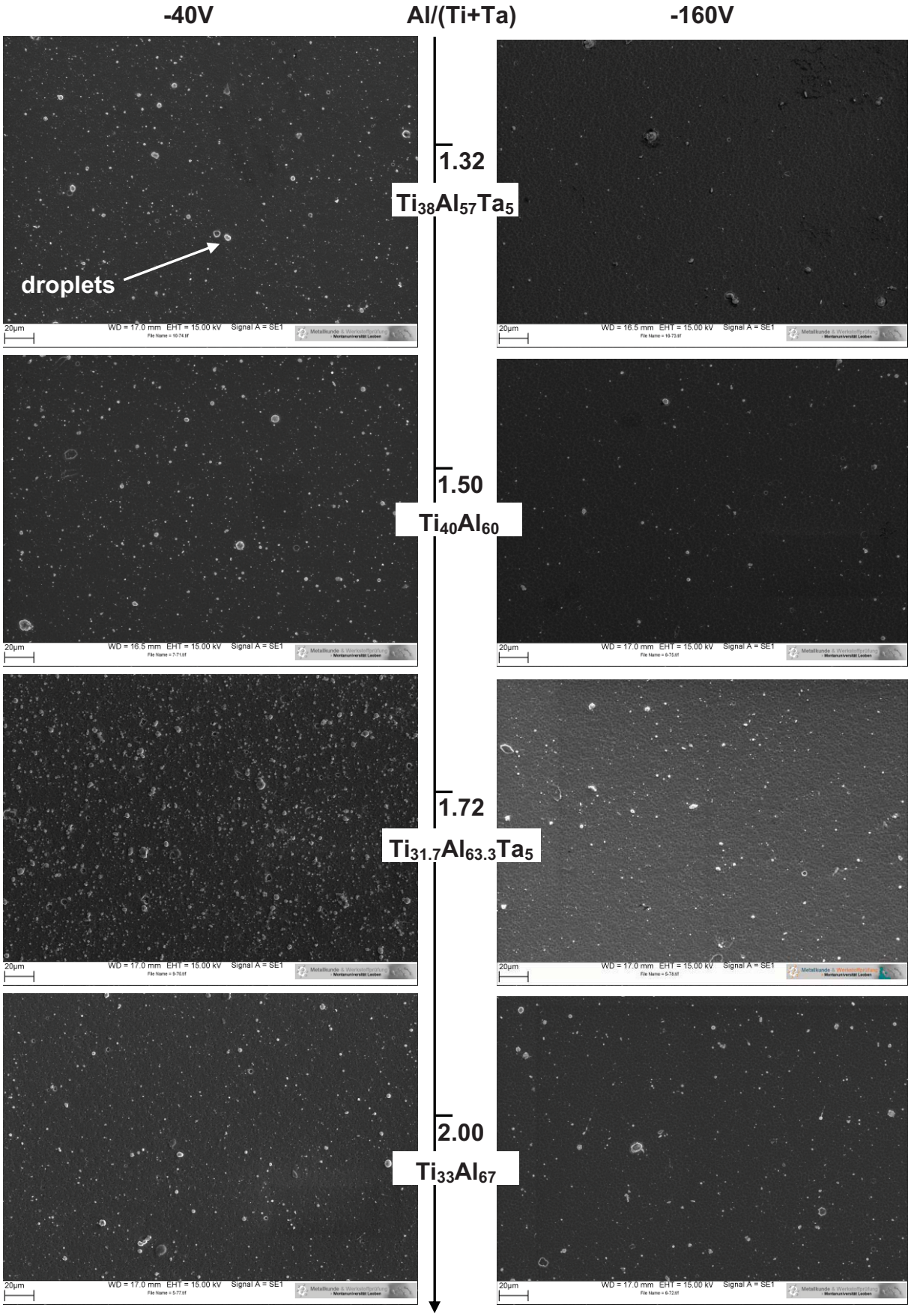

Figure 6.5: SEM micrographs of all coating systems deposited at -40 and -160V bias voltage.

6.4 Phase Composition (XRD)

Within this chapter, the results of the XRD analyses are shown for each coating system at different bias voltages (Figure 6.6 - Figure 6.9). The according target composition and bias voltage for each pattern is given on the right side and reflex positions are marked by drop-lines. Blue solid lines denote the fcc- TiN phases; red dashed lines mark the fcc- AlN phases and orange dash-dot lines show the hcp- AlN peaks. In Ta containing systems, the position of fcc- TaN peaks are marked by green dotted lines. Generally, in all patterns it can be observed that the peaks are shifted compared to the marked phase positions. Neither TiN nor AlN and TaN phases occur in their basic pure binary structures. Due to the incorporation of the smaller Al atom into the fcc- TiN cell, the peaks are shifted to higher angles (compare 2θ = 37.1°, 43.2° and 63.1°), observable between the standard positions of fcc- TiN and fcc- AlN. Thus, the peaks originate from an fcc- (Ti,Al)N solid solution. The same explanation can be given for the shifted hcp- AlN peaks. If the larger Ti is incorporated in the hcp-AlN cell, the XRD peaks are shifted to lower angles [72].

In Figure 6.6, the XRD pattern of the coating deposited from the $Ti_{40}Al_{60}$ target (Al/Ti ratio of 1.5) is shown. At a bias voltage of -40V a relatively high amount of hcp-phase is observed (2θ=34.7°, 80.1°) next to the fcc- (Ti,Al)N peaks at 2θ = 37.7°, 42.2° and 63.1°. The increase of the bias voltage up to -160V leads to a significant decrease of the hexagonal phase. Mayrhofer et al. reported that the stability of the fcc- $Ti_{1-x}Al_xN$ phase not only depends on the Al content, but also on the distribution of Al [36]. With an increasing level of disorder of the incorporated Al atoms in the fcc-$Ti_{1-x}Al_xN$ cell, which may be reached by enhanced ion bombardment, a higher amount of Al atoms can be incorporated into the fcc- TiN cell. The enhancement of the ion bombardment can be reached by increasing the bias voltage during deposition. Furthermore, the fcc- (Ti,Al)N peak intensity at the angle of 37.7° increases at the expense of the peak intensity at 42.2°. Thus, the preferred texture changes with increasing bias voltage from (200) to (111) orientation.

The XRD pattern of the coating deposited from the target with the Al/Ti = 2 ($Ti_{33}Al_{66}$) is shown in Figure 6.7. The higher Al amount obviously leads to a dominating hcp structure with a much lower amount of fcc phases at the bias voltage of -40V, compared to the coating with the lower Al fraction (Al/Ti=1.5, see Figure 6.6). At a higher bias voltage (-160V), the hexagonal phase nearly disappears, while the cubic (Ti,Al)N phase dominates the structure. The intensity of the small peaks at 37.1° (111) and 63.1° (220) strongly increases with increasing bias voltage, while the intensity of the fcc peak at 43.2° (200) decreases, similar to the behavior, which has been observed for the coating with the lower Al content (Figure 6.6). Additionally it

can be observed that at higher angles (95.3°, 112.4° and 131.2°) further fcc- (Ti,Al)N phase peaks occur.

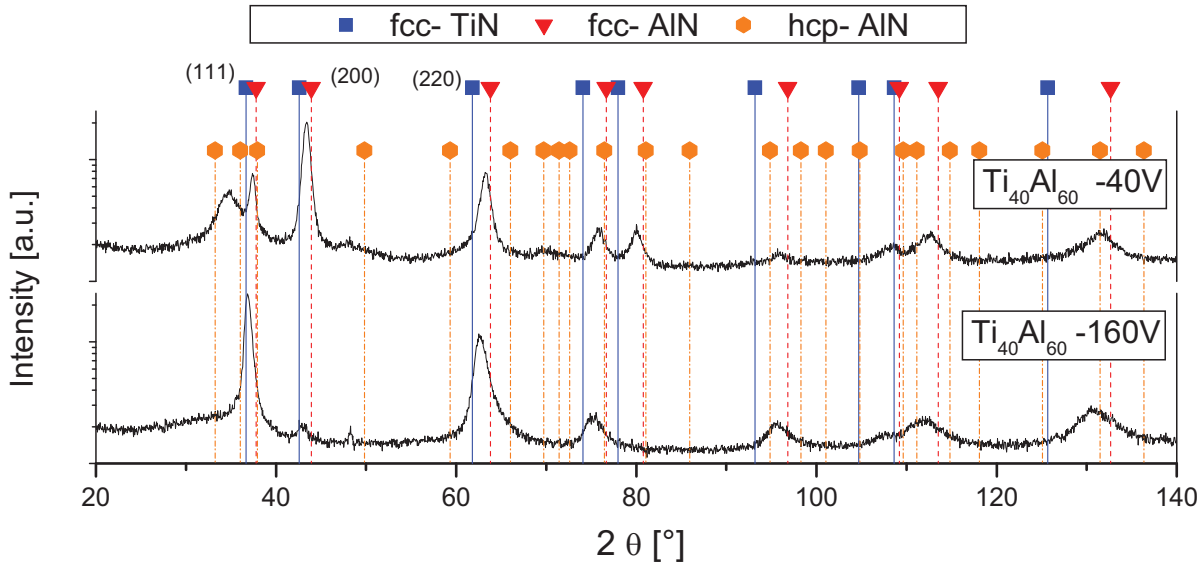

Figure 6.6: XRD patterns of the coatings, deposited from the $Ti_{40}Al_{60}$ target, at negative bias voltages of -40V and -160V.

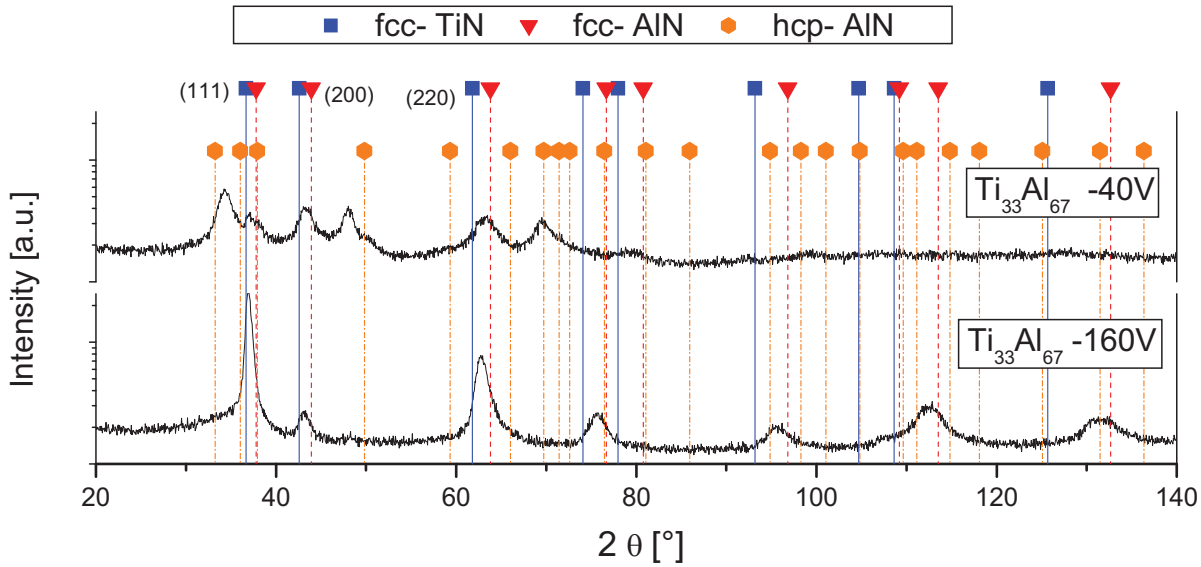

Figure 6.7: XRD patterns of the coatings, deposited from the $Ti_{33}Al_{67}$ target, at negative bias voltages of -40V and -160V.

Moreover, two coating systems containing Ta have been investigated. The Al/Ti ratio in the target was the same as for the reference TiAl target compositions, discussed above. However, due to the incorporation of Ta, the Al/(Ti+Ta) ratio correspond to 1.32 and 1.72, respectively. Figure 6.8 shows the XRD pattern of the Ta containing coatings deposited from the target with the Al/(Ti+Ta) ratio of 1.32 (low Al content). The occurring peaks are similar to the reference coating (compare Figure 6.6). The intensity of the fcc- (Ti,Al)N peaks in case of -40V bias voltage is higher compared to the system without Ta, whereas the hcp phase is less pronounced. Thus, it can be suspected that Ta stabilizes the fcc- (Ti,Al)N phase [60]. At the bias voltage of -40V, the (200) as well as the (220) peak are dominating, but there is also a low intensity cubic (111) peak detectable. An increase of the applied bias voltage (-80V) results in broader fcc peaks, while the hexagonal peak (at 2θ=34.7°) nearly disappears. Further increasing the bias voltage from -80V to -120V changes the preferred orientation from (200) to (111), similar to the reference system without Ta. This behavior is pronounced with the enhancement of the applied bias voltage to -160V. A pure fcc structure, with dominating (111) and (220) peaks is observed.

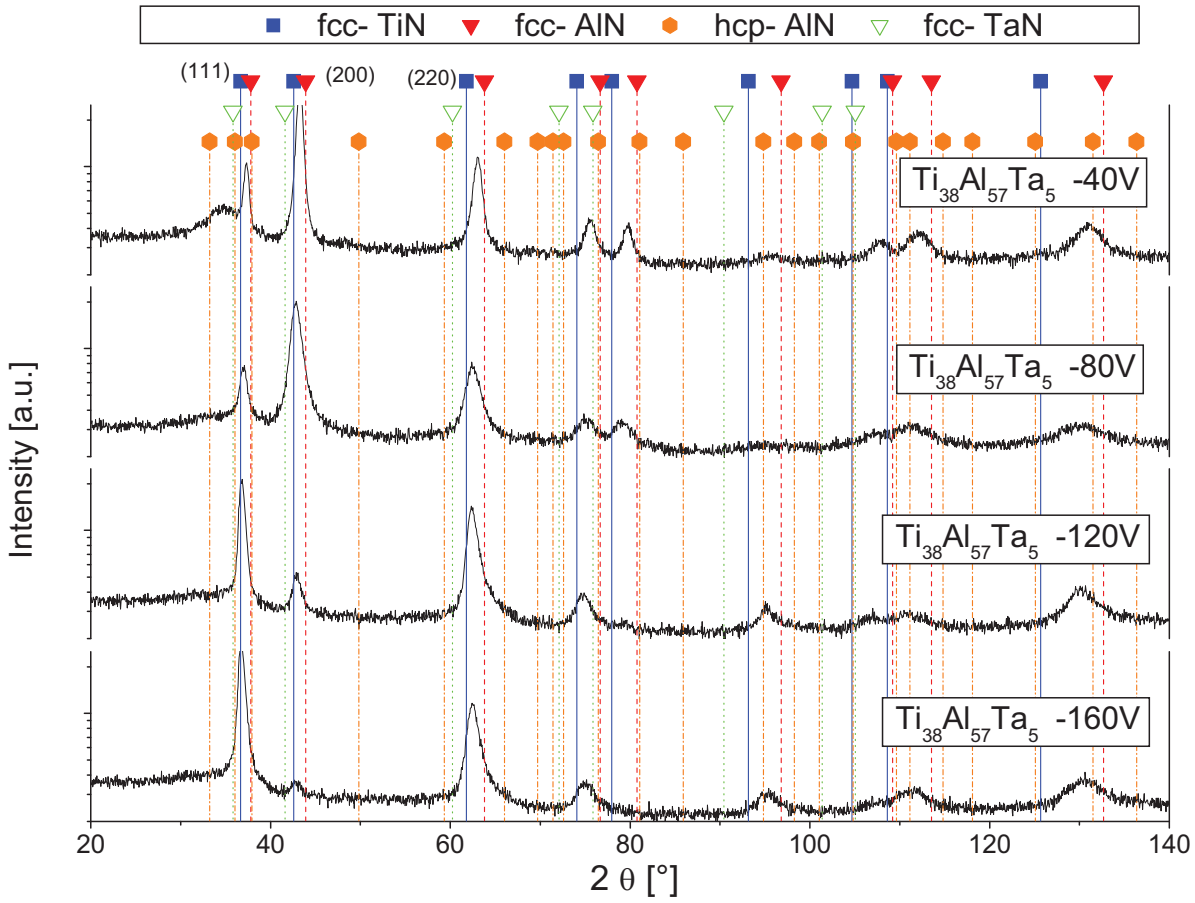

Figure 6.8: XRD patterns of the coatings, deposited from the $Ti_{38}Al_{57}Ta_5$ target (Al/(Ti+Ta) = 1.32), at negative bias voltages of -40V, -80V, -120V and -160V.

The Ta containing coating system with higher Al/(Ti+Ta) ratio (1.72) is clearly dominated by the hcp- AlN phase at a low (-40V) bias voltage (see Figure 6.9). With enhanced bias voltage, the amount of the fcc- (Ti,Al)N phase increases rapidly. A more pronounced (200) peak at the expense of the hexagonal peak (2θ=34.7) appears. The development of the fcc structure within the increasing bias voltages is similar to the other investigated systems. At a bias voltage of -80V, the structure is dominated by the (200) and a lower (220) peak. Between -80V and -120V, the texture changes from the preferred (200) orientation into a (111) while the (220) peak further grows with increasing bias voltage. Moreover, at high bias voltages (-120V and -160V) a more equiaxed structure appears, indicated by further cubic peaks at higher orientations.

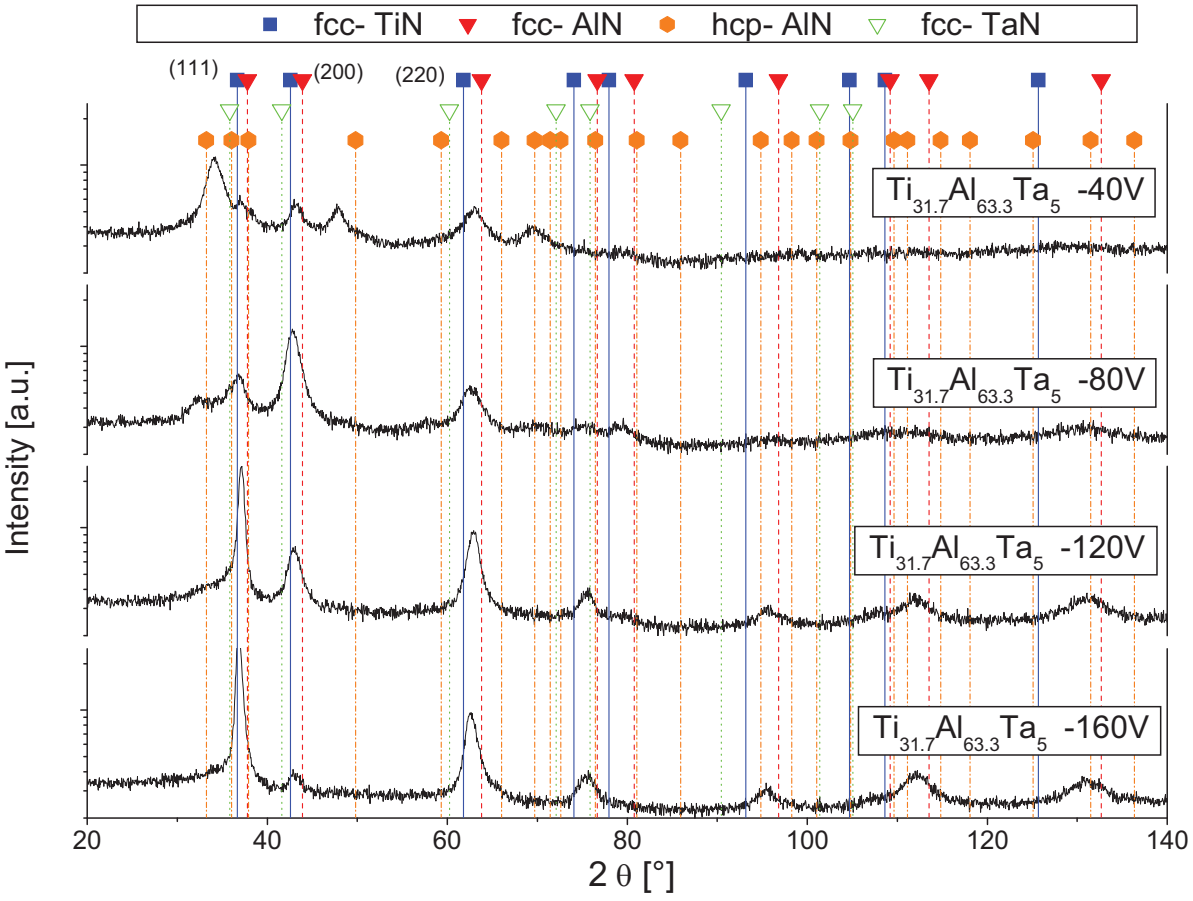

Figure 6.9: XRD patterns of the coatings, deposited from the $Ti_{31.7}Al_{63.3}Ta_5$ target, at negative bias voltages of -40V, -80V, -120V and -160V.

Both samples with higher Al ratio (with and without Ta) show a low peak intensity at higher angles (higher orientations), when a bias of only -40V is applied during deposition. However, all investigated coating systems result in very similar phase

composition when -160V bias was applied, a pronounced (111) and (220) orientated cubic (Ti,Al)N phase. The occurrence of a pure TaN phase in the Ta containing coatings could not be detected. Here, it has to be mentioned that only a low Ta content, of about 1.7÷1.9 at% instead of the desired 5 at% (in the target) was detected by GDOES. Nevertheless it is figured out that Ta seems to stabilize the fcc-(Ti,Al)N phase, although it is not able to totally change the structure from hexagonal into cubic with that low alloying content. Moreover, the bias voltage significantly influences the structure of the resulting film. Applying an enhanced bias voltage (-160V) to the substrate during the deposition process, a pure fcc structure can be reached, even at higher Al contents. Furthermore, the bias voltage changed the dominated orientation in all four coating systems from (200) to (111).

6.5 Microhardness

In the previous chapter, a correlation between the Al/(Ti+Ta) fraction, the bias voltage, the Ta addition and the resulting microstructure could be detected. The effects on the mechanical properties of this interaction are now demonstrated by means of Microhardness measurement. Figure 6.10 shows the microhardness results depending on the applied bias voltage. The X-axis sorts the coating systems by the target composition, in particular by their Al/(Ti+Ta) ratio. The coatings from the $Ti_{38}Al_{57}Ta_5$ target exhibit the highest hardness values of 28 GPa, increasing with increasing bias voltage up to 32 GPa at -160V. The XRD pattern of this coating already showed that the fcc- (Ti,Al)N phase clearly dominates the microstructure of this coating system, the small amount of hexagonal phase at -40V completely disappeared with increasing bias voltage. Moreover, a texture transition from (200) to (111) preferred orientation between -80V and -120V may give rise to higher hardness values. The corresponding reference coating (target: $Ti_{40}Al_{60}$) with the same Al/Ti ratio of 1.5 shows a lower hardness value for coatings deposited at -40V; this can be explained by the higher amount of hcp phase. At -160V the hardness stays nearly constant with respect to the error bars, although the XRD pattern of this coating shows a similar phase composition as the Ta containing sample. Thus, it can be speculated that Ta influences the microhardness by a solid solution hardening effect, which is caused by the incorporation of Ta into the fcc- (Ti,Al)N cell. Both systems with higher Al fraction show a lower microhardness of around 21 GPa at -40V which corresponds to the dominating hexagonal structure. With increasing bias voltage, the phase analysis showed that the amount of fcc- (Ti,Al)N strongly increases at the expense of hcp- (Al,Ti)N, resulting in a significant hardness increase for both coating systems. The Ta alloyed sample reaches a maximum hardness of 32 GPa at -120V. However, at -160V a significant drop-down in hardness occurs. Nevertheless, also

the microhardness of the reference coating without Ta ($Ti_{33}Al_{66}$ target) reaches a remarkable hardness of more than 30 GPa at a bias voltage of -160V.

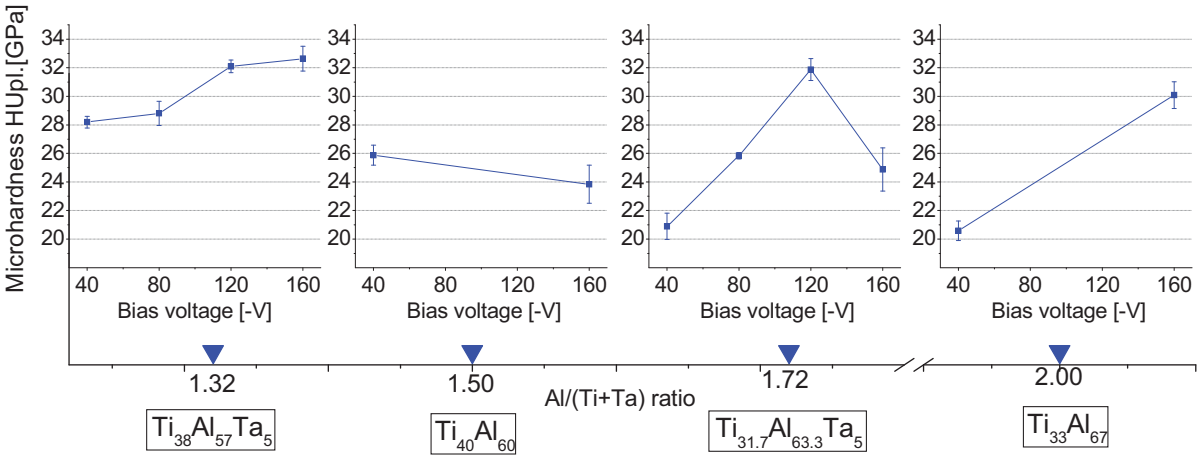

Figure 6.10: Microhardness of all coating systems depending on the bias voltage. The lower X-axis sorts all four systems by the Al/(Ti+Ta) ratio in the target. The denoted compositions are the target compositions.

6.6 Tribology

The tribological investigations have been carried out to characterize the friction and wear behavior of (Ti,Al)N and (Ti,Al,Ta)N coating systems, deposited at different bias voltages. The tribological tests have been performed at three different temperatures (25°C, 500°C and 700°C) against an alumina ball as counter body. The results of these tests are explained in detail for each temperature.

6.6.1 Tribological Tests at Room Temperature (25°C)

The determined friction coefficients for all coating systems depending on the bias voltage are shown in Figure 6.11. The systems are sorted by their Al content (X-axis) and denoted by their corresponding target composition. Both systems with lower Al/(Ti+Ta) ratio, especially $Ti_{40}Al_{60}$, show a higher friction coefficient with increasing bias voltage. The Ta containing system (target: $Ti_{38}Al_{57}Ta_5$) exhibits a lower friction coefficient (0.729 to 0.887), compared to the reference sample without Ta, which reaches the maximum friction coefficient of 1.0 for the coating deposited at -160V bias voltage. Moreover, this is the highest friction coefficient of all coating systems at room temperature. For the systems with a higher amount of Al (Al/(Ti+Ta) = 1.72 and 2.00), the friction behavior is nearly constant over the bias voltage. The coatings

deposited from the $Ti_{31.7}Al_{63.3}Ta_5$ target showed values of 0.85 to 0.91, whereas the coating deposited from the reference targets with the same Al/Ti ratio even displayed lower friction values of 0.73 to 0.76. All coatings offered huge scattering of the friction curves resulting in large error bars. Representative for all coating systems, Figure 2.9 shows the friction curves of the coatings deposited from the $Ti_{40}Al_{60}$ target at -40V and -160V bias voltage. After a short running-in distance, a steady-state friction coefficient is reached, with high scattering over the whole sliding distance.

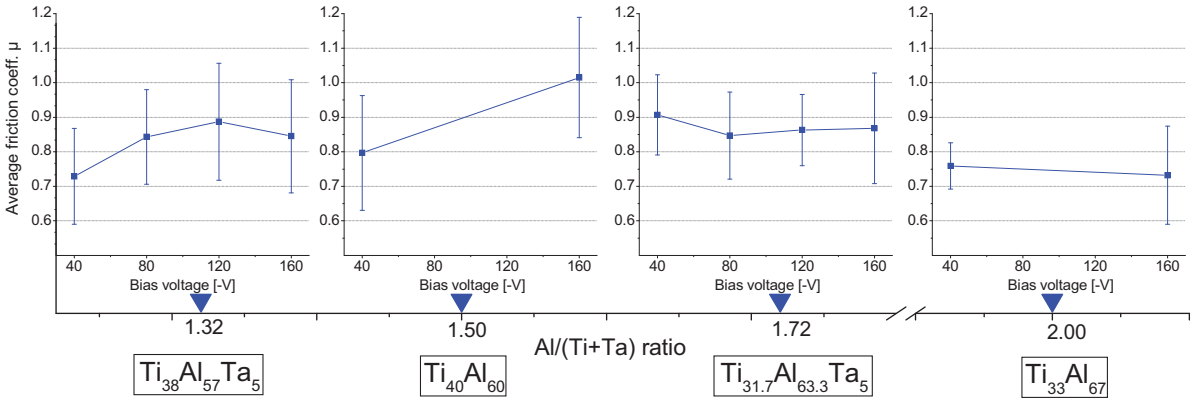

Figure 6.11: Friction coefficients as a function of the applied bias voltage for all coating systems at room temperature (25°C). The X-axis shows the corresponding Al/(Ti+Ta) ratios and the exact target compositions are given below the graph.

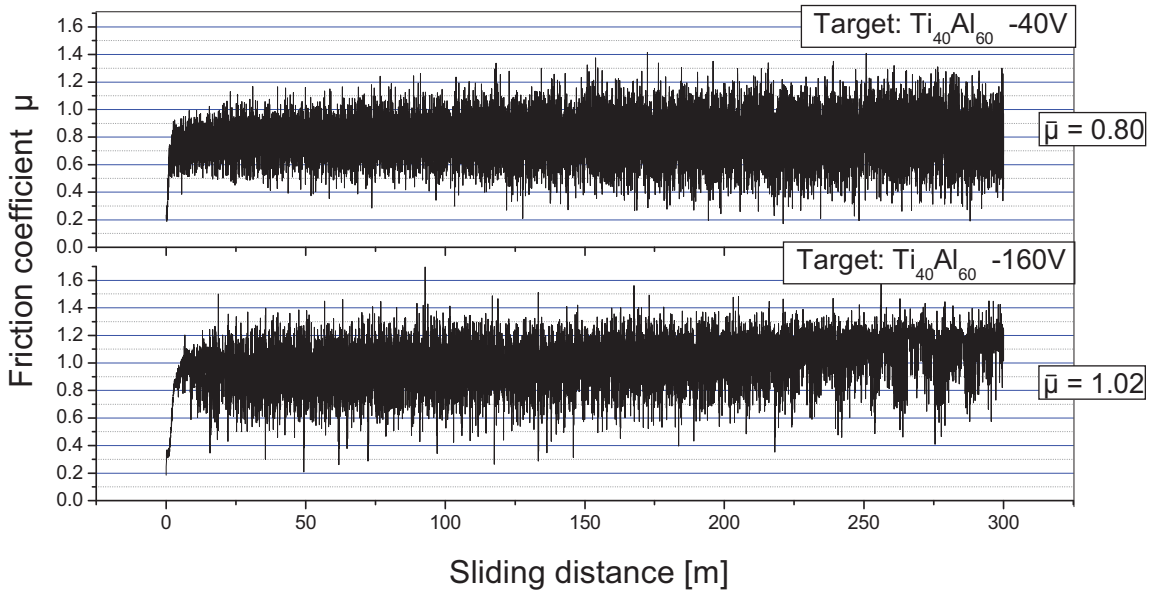

Figure 6.12: Friction curves of coatings deposited from the $Ti_{40}Al_{60}$ target at -40V and -160V bias voltage tribologically tested at room temperature against an alumina ball.

After the tribological tests, all samples have been investigated with the optical profilometer to gain information about the wear behavior. To characterize the wear behavior, the so-called negative wear coefficient has been calculated which represents the worn material during the sliding test with respect of the influencing sliding parameters, like load and sliding distance. These wear coefficients of several coating systems as a function of the applied bias voltage are demonstrated in Figure 6.13. At a lower bias voltage, the coatings with lower Al contents (Al/(Ti+Ta) = 1.32 and 1.50)) show a much better wear behavior than the samples with a higher Al fraction. For example, the films deposited from the $Ti_{38}Al_{57}Ta_5$ and the $Ti_{40}Al_{60}$ target at -40V bias voltage show a wear coefficient of -11.4 $.10^{-15}$ and -13.4 $.10^{-15}$ m^3/Nm, while the wear coefficients of the coatings deposited from the $Ti_{31.7}Al_{63.3}Ta_5$ and the $Ti_{33}Al_{66}$ targets range between -19.8 $.10^{-15}$ and -24.2 $.10^{-15}$ m^3/Nm. With increasing bias voltage (-80V and -120V), the wear coefficient increases in case of coating deposited from the $Ti_{38}Al_{57}Ta_5$ target, but at a bias voltage of -160V the wear behavior improves resulting in a coefficient of -12.3 $.10^{-15}$ m^3/Nm. Also the corresponding reference sample (Al/Ti = 1.5) shows a slightly increasing wear coefficient with increasing bias voltage. Both samples with higher Al content (Al/(Ti+Ta) = 1.72 and 2.00) show a quite more significant change of the wear coefficient with increasing bias voltage. Between -80V and -120V applied bias voltage, the wear coefficient of the Ta containing coating (Al/(Ti+Ta)=1.72) again increases to a value of -21.2 $.10^{-15}$ m^3/Nm until the determining the lowest wear coefficient of this system (-13.5 $.10^{-15}$ m^3/Nm) is reached at -160V. For the reference coating without Ta (Al/Ti = 2.00) the wear behavior was also improved with higher bias voltage.

These results can be related to the microstructure (compare chapter 6.4). The coatings deposited from the $Ti_{38}Al_{57}Ta_5$ target as well as the $Ti_{40}Al_{60}$ target are dominated by a fcc phase, even at a bias voltage of -40V. Thus the bias voltage seems to play a minor role in these coating systems. The coatings containing more Al (Al/(Ti+Ta) = 1.72 and 2.00)) show a predominant hcp phase at -40V. With increasing bias voltage, the amount of fcc phase strongly increases at the expense of the hcp phase, resulting in an enhanced wear behavior (see Figure 6.13). Between an applied bias voltage of -80V and -120V, the corresponding XRD pattern showed a texture transition, which may be suggested to be responsible for the sudden increase of the wear coefficient in case of the coating deposited from the $Ti_{31.7}Al_{63.3}Ta_5$ target. However, the wear coefficient significantly decreased to half the value between -40V and -160V bias voltage. Additionally, Figure 6.14 shows the 2-dimensional plot of the wear tracks of the coatings deposited from the $Ti_{31.7}Al_{63.3}Ta_5$ target, representative for all coating systems. The depth of the wear track, i.e. the worn volume, significantly decreases from -40V to -160V bias voltage.

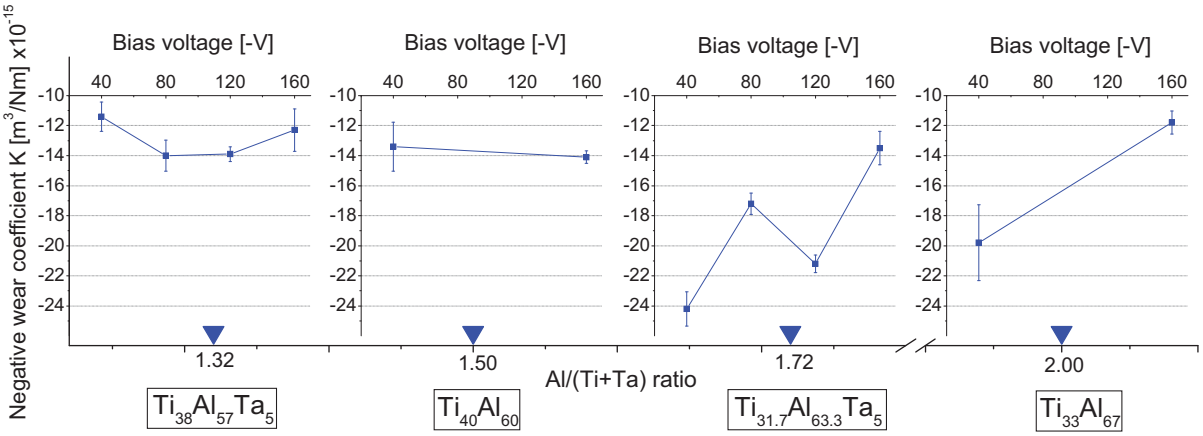

Figure 6.13: Negative wear coefficients as a function of the bias voltage for all coating systems. The X-axis shows the corresponding Al/(Ti+Ta) ratios and the exact target compositions are given below the graphs.

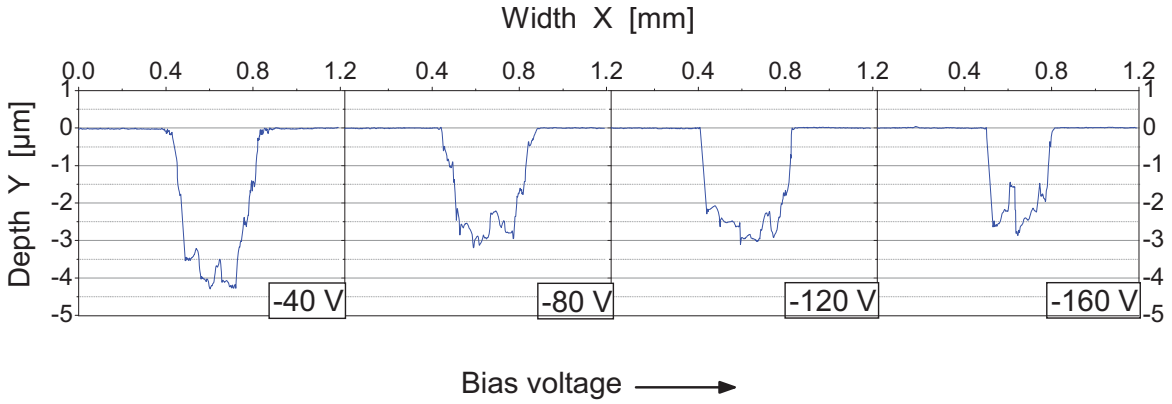

Figure 6.14: 2-dimensional plots of the wear tracks of the coating deposited from the $Ti_{31.7}Al_{63.3}Ta_5$ target at -40, -80, -120 and -160 V applied bias voltage.

6.6.2 Tribological Tests at 500°C

Figure 6.15 shows the friction behavior of the investigated coating systems at 500°C. At -40V applied bias voltage, the friction coefficients of all coatings are between 0.8 and 1.0, where the Ta containing coating systems show a lower coefficient compared to the reference samples without Ta. In case of the Ta containing system with lower Al content (Al/(Ti+Ta) = 1.32), the coefficient of friction increases at -80V and -120V. However, at a bias voltage of -160V this system results in the lowest average friction coefficient of all coating systems (μ=0.66). The corresponding friction curves are displayed in Figure 6.16. For the coating deposited at -40V bias voltage, a huge scattering can be seen, resulting in a large error bar in the diagram in Figure 6.15. At higher bias voltages, the friction coefficient proceeds constantly after a short running-in distance of about 50 meters. A different behavior can be observed at -160V, where the coefficient of friction suddenly increases after about 170 m and additionally shows a huge scattering.

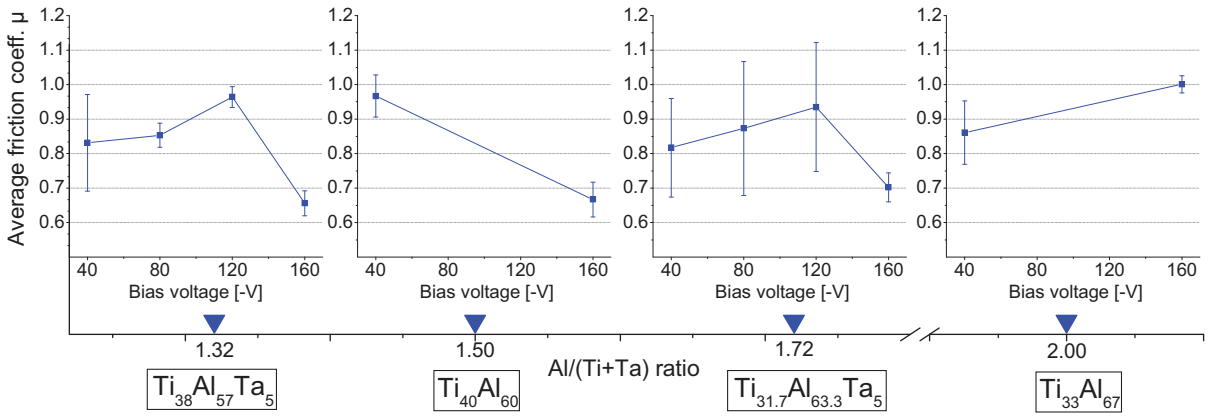

Figure 6.15: Friction coefficients as a function of the applied bias voltage for all coating systems at 500°C. The X-axis shows the corresponding Al/(Ti+Ta) ratios and the exact target compositions are given below the graphs.

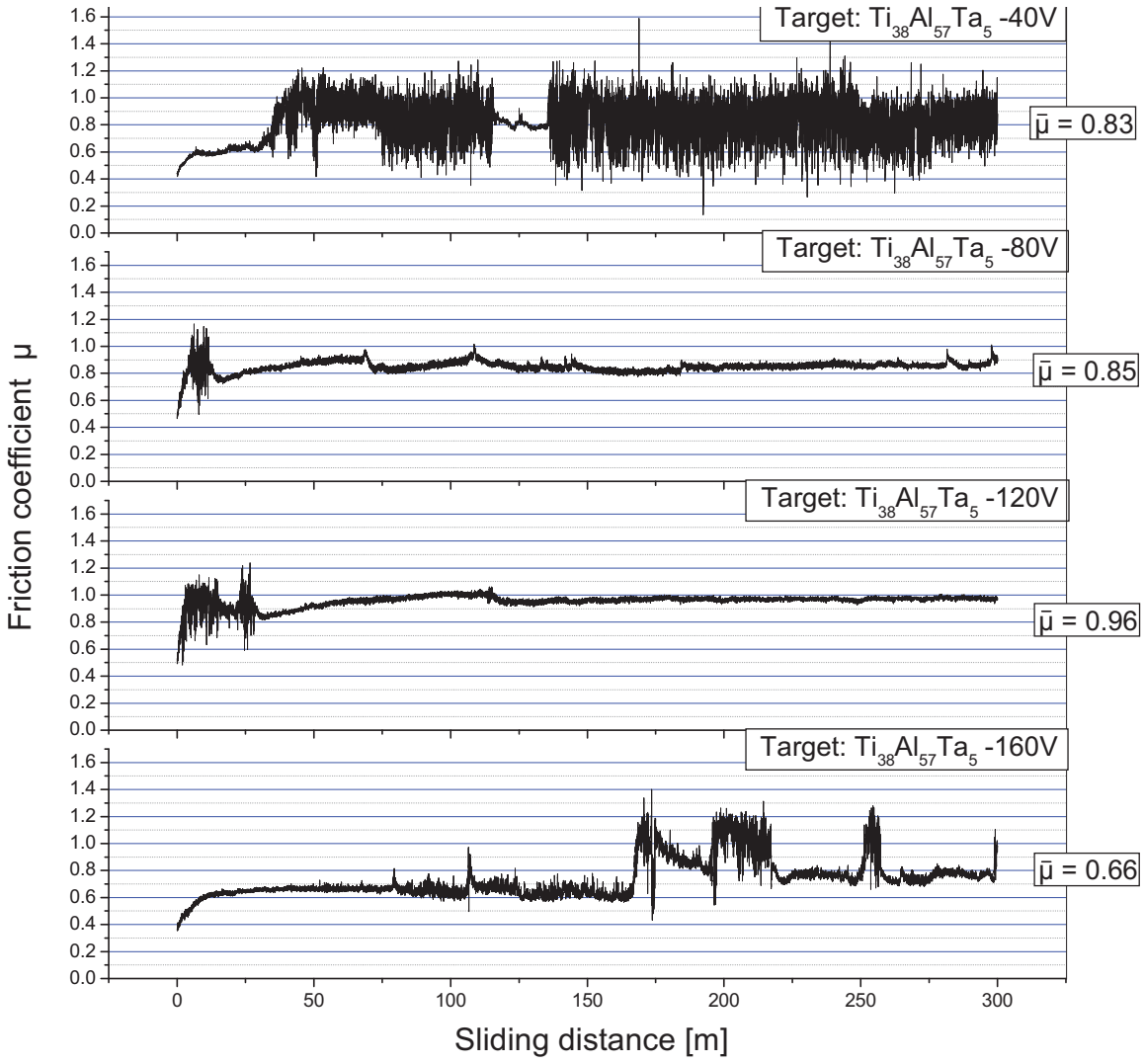

Figure 6.16: Friction curves of the coatings deposited from the $Ti_{38}Al_{57}Ta_5$ target at -40V, -80V, -120V and -160V bias voltage, tribologically tested at 500°C against alumina.

Detailed SEM investigations of the coatings deposited at -40V and -80V bias voltage have been done to determine the reason for the different friction and scattering behavior. Figure 6.17 shows the SEM micrograph in secondary electron (SE) mode (left row) of the wear tracks from the coating deposited from the $Ti_{38}Al_{57}Ta_5$ target (Al/(Ti+Ta)=1.32) at -40V bias voltage. This mode has been employed to gain topographical information of the wear track. Different heights are seen as dark and bright contrasts, whereby dark areas correspond to crater whereas the bright ones are hills. In the wear track, a high amount of bright area can be observed, which is assumed to be attached material, e.g. oxides, resulting from adhesive wear. For the identification of this attached material, additionally back scatter diffraction (QBSD) scans were employed. In this mode, heavy and light weight elements can be detected via bright and dark contrast, thus, oxides can be distinguished from metal containing phases. The investigations suggest that worn areas (e.g. due to ploughing

or fatigue) are filled up with alumina from the ball, observable as a large amount of dark areas (oxides) in the QBSD micrographs (right row) in Figure 6.17.

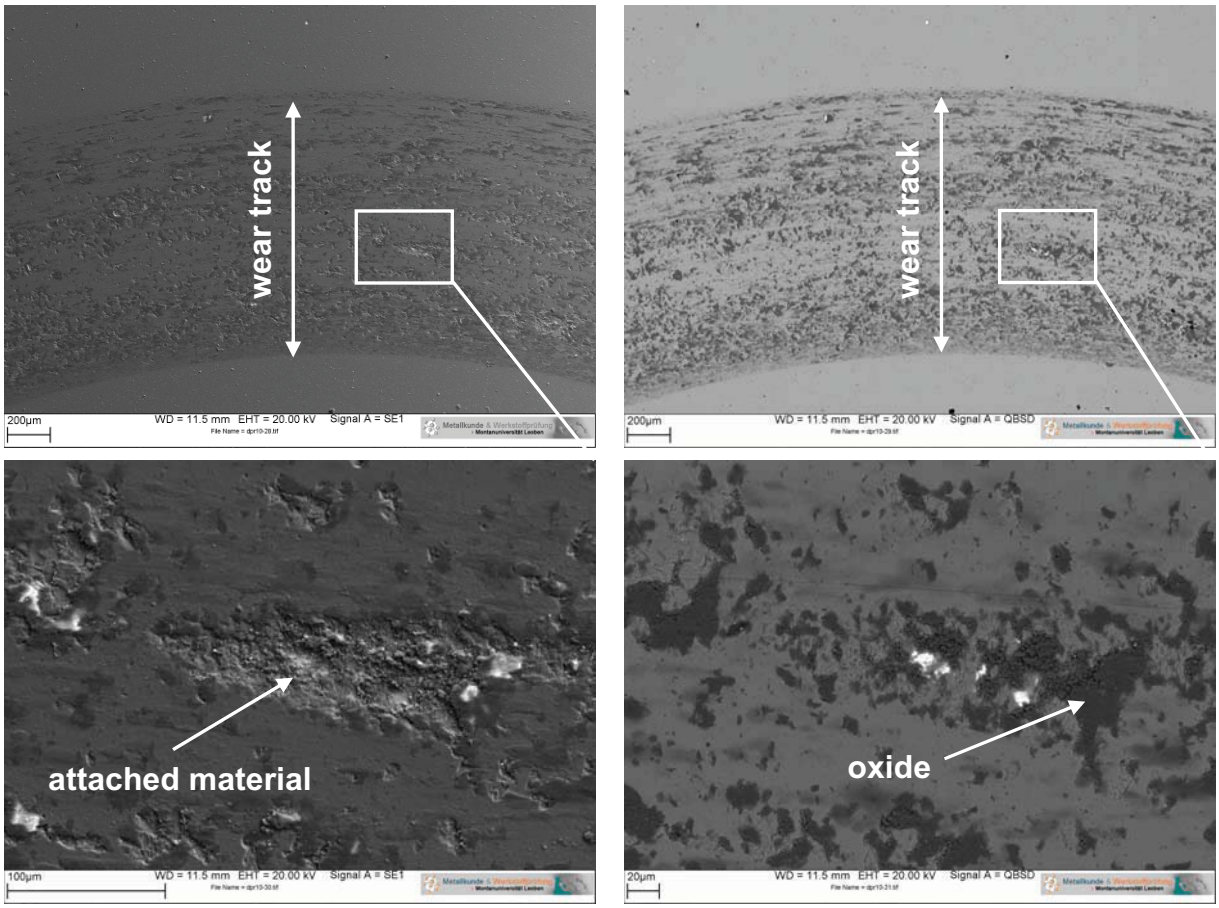

Figure 6.17: SEM micrographs in SE mode (left row) and QBSD mode (right row) of the wear track of the coating deposited from the $Ti_{38}Al_{57}Ta_5$ target at -40V bias voltage after tribological testing at 500°C against alumina.

The same analysis has been carried out for the wear track of the corresponding coating (target: $Ti_{38}Al_{57}Ta_5$) deposited at -80V bias voltage. The friction curve of this sample showed only low scattering compared to the corresponding coating deposited at -40V bias voltage (compare Figure 6.16). The SEM micrographs in SE mode as well as in QBSD mode (Figure 6.18) show no attached material. Moreover, the SE micrographs show clear ploughing in the wear track as wear mechanism. Thus, from the different wear tracks and scattering behavior it can be concluded that for the coatings deposited at different bias voltages of -40V and -80V different wear mechanism occurred.

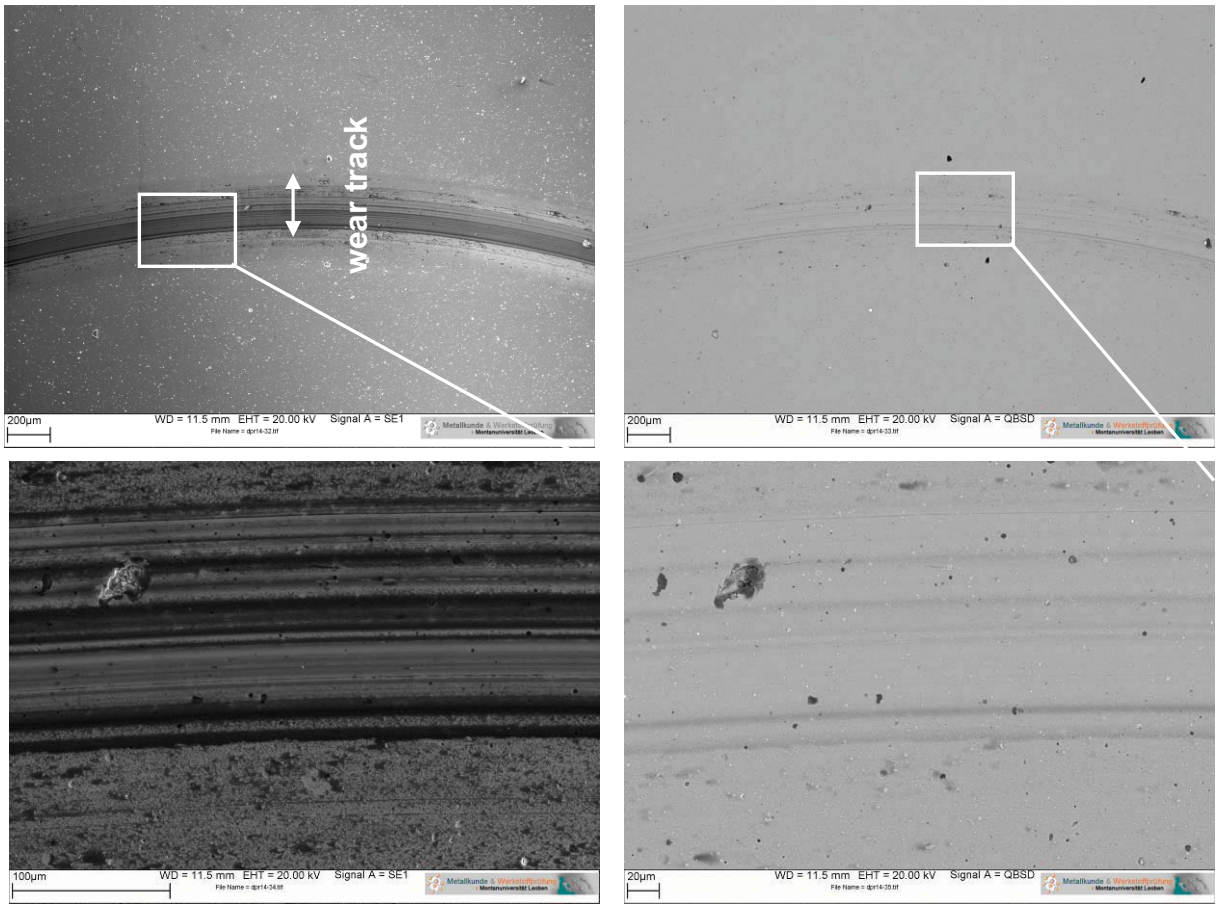

Figure 6.18: SEM micrographs in SE mode (left row) and QBSD mode (right row) of the wear track of the coating deposited from the $Ti_{38}Al_{57}Ta_5$ target at -80V bias voltage after tribological testing at 500°C against alumina.

Figure 6.19 shows the friction curves of the corresponding reference sample without Ta (Ti/Al = 1.52). At a bias voltage of -40V, only narrow scattering is detected after a short running-in distance while the average friction coefficient (0.97) is higher compared to the sample containing Ta (0.83). However, the friction behavior at -160V is very similar to the Ta containing system, very low but slightly increasing over the whole distance, resulting in an average friction coefficient of 0.67. Also for this coating system, SEM micrographs have been taken, which are shown in Figure 6.20. The SE micrograph (left row) shows ploughing in the wear track, similar to the coating deposited from the $Ti_{38}Al_{57}Ta_5$ target at -80V (compare Figure 6.18). Less attached oxides can be detected in the QBSD mode (right row).

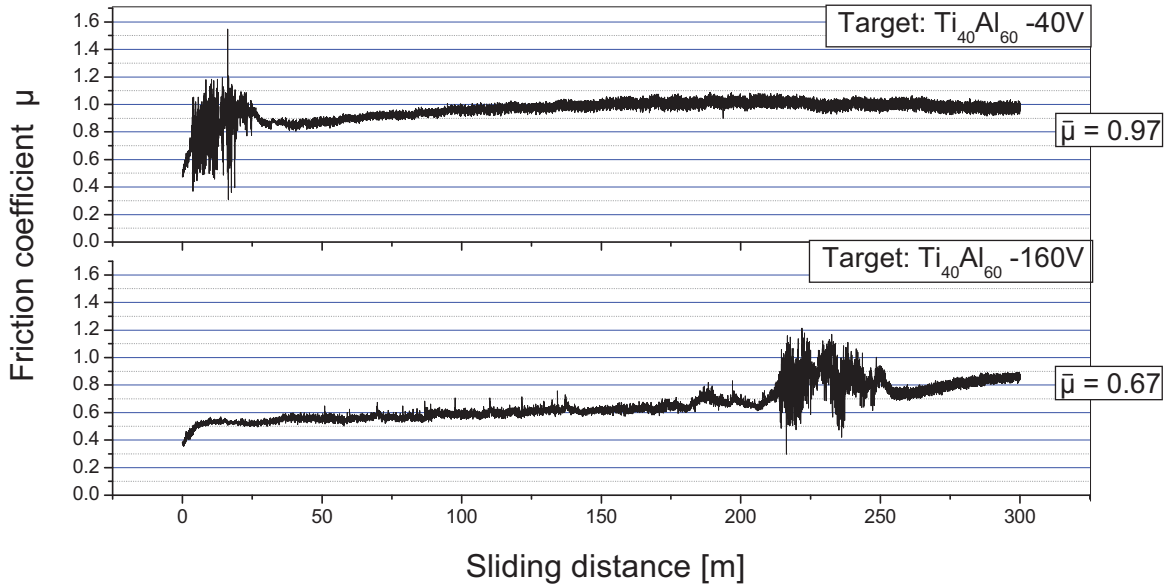

Figure 6.19: Friction curves of the coating deposited from the $Ti_{40}Al_{60}$ target at -40V and -160V bias voltage, tribologically tested at 500°C against alumina.

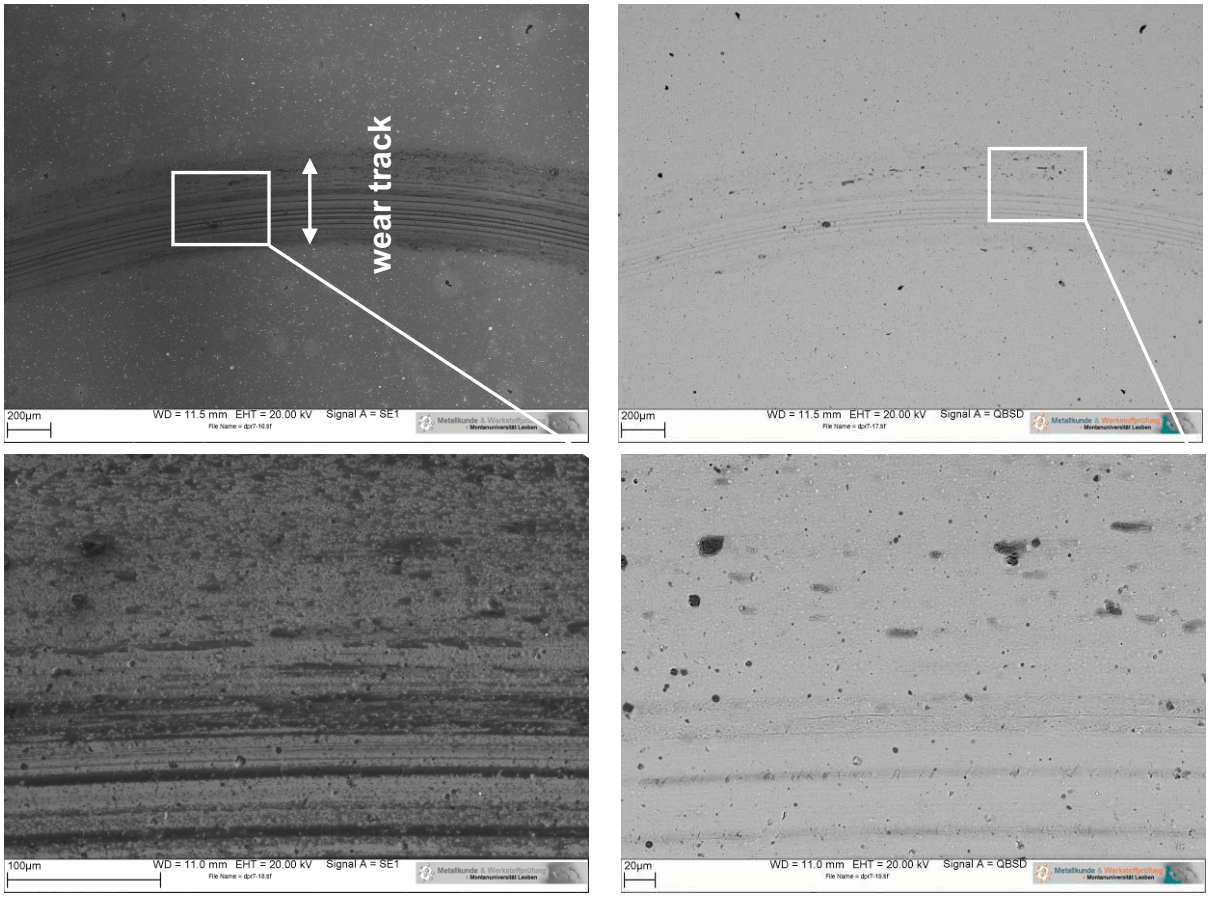

Figure 6.20: SEM micrographs in SE mode (left row) and QBSD mode (right row) of the wear track of the coating deposited from the $Ti_{40}Al_{60}$ target at -40V bias voltage after tribological testing at 500°C against alumina.

The friction curves of the coatings resulting from the$Ti_{31.7}Al_{63.3}Ta_5$ target (Figure 6.21) show an increasing friction coefficient with huge scattering for -40V, -80V and -120V. At -160V bias voltage, the coefficient of friction significantly decreases, similar to the Ta containing coating system with the lower Al content (Al/(Ti+Ta) = 1.32, see Figure 6.15) and the friction curve indicates only a small scattering.

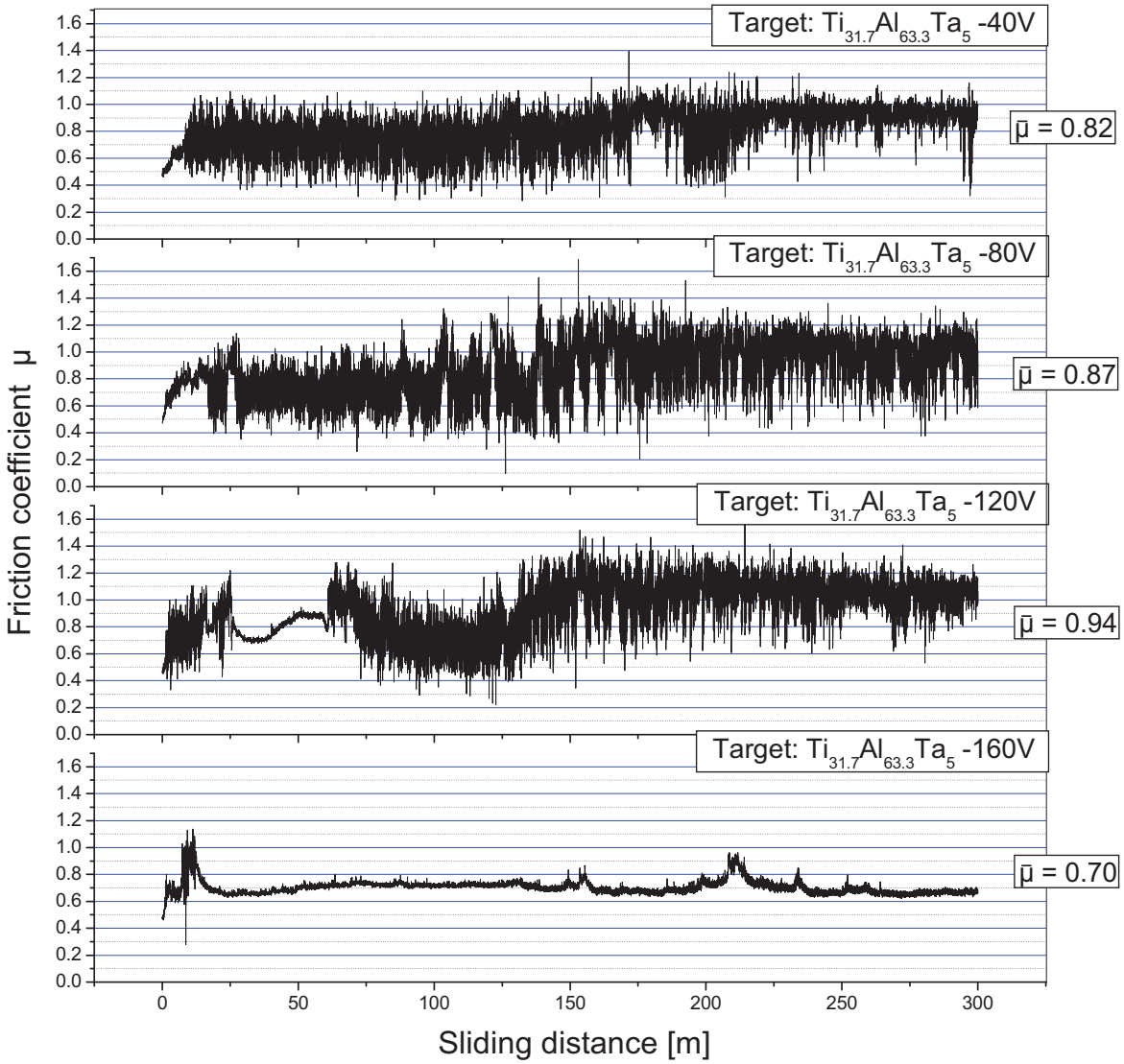

Figure 6.21: Friction curves of the coatings deposited from the $Ti_{31.7}Al_{63.3}Ta_5$ target at -40V, -80V, -120V and -160V bias voltage, tribologically tested at 500°C against alumina.

Again the different friction and scattering behavior of the coatings deposited at -40V and -160V bias voltage has been investigated. For the sample deposited at -40V bias voltage, the SEM micrographs (SE mode and QBSD mode) of the wear track are displayed in Figure 6.22. Within the wear track, a huge amount of attached material, identified as oxides by QBSD, can be detected. Moreover, in the QBSD micrograph

there are very bright spots seen, which can be suspected to be areas containing a larger concentration of heavy atoms such as Ta. The SE and QBSD micrographs of the sample deposited at -160V bias voltage is shown in Figure 6.23. Compared to the sample deposited at -40V applied bias voltage, the amount of attached oxides is very low. However, ploughing can be detected in the wear track.

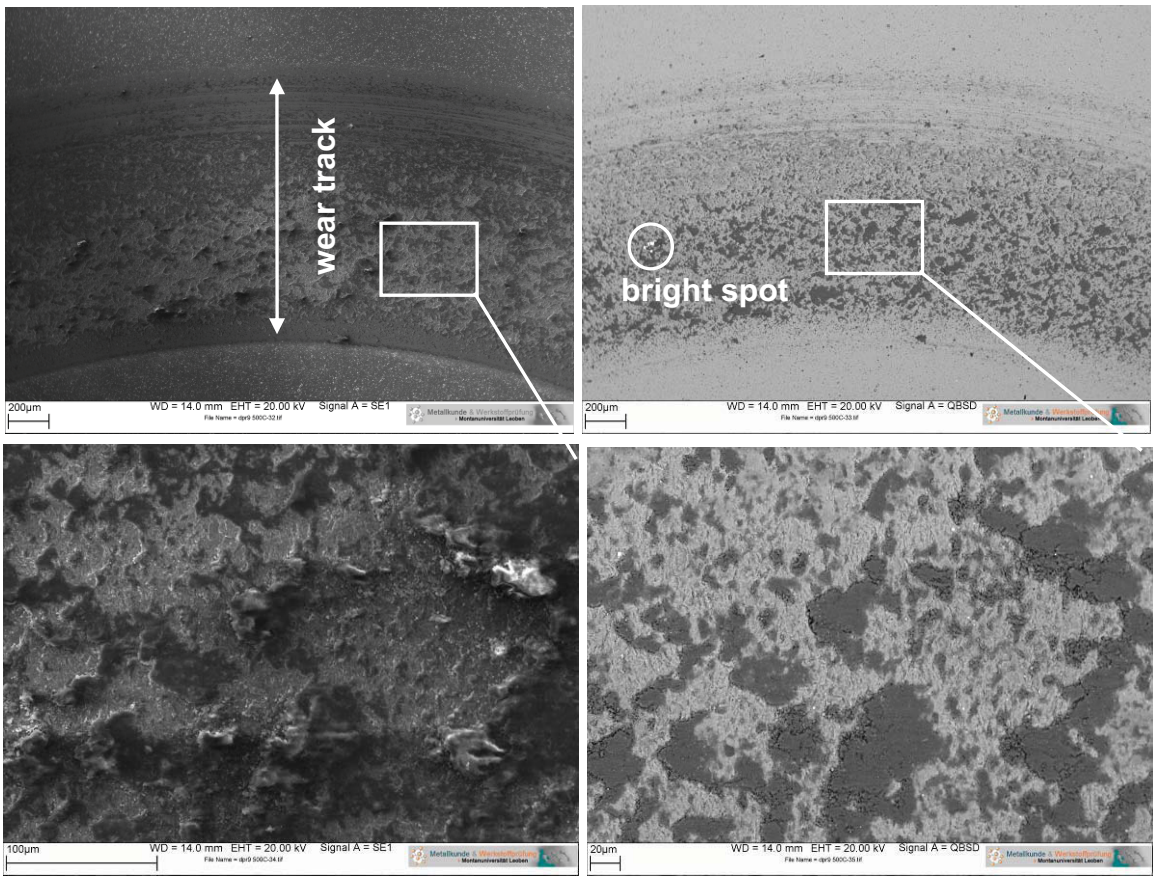

Figure 6.22: SEM micrographs in secondary electrons mode (left row) and QBSD mode (right row) of the wear track of the coating deposited from the $Ti_{31.7}Al_{63.3}Ta_5$ target at -40V bias voltage after tribologically testing at 500°C against alumina.

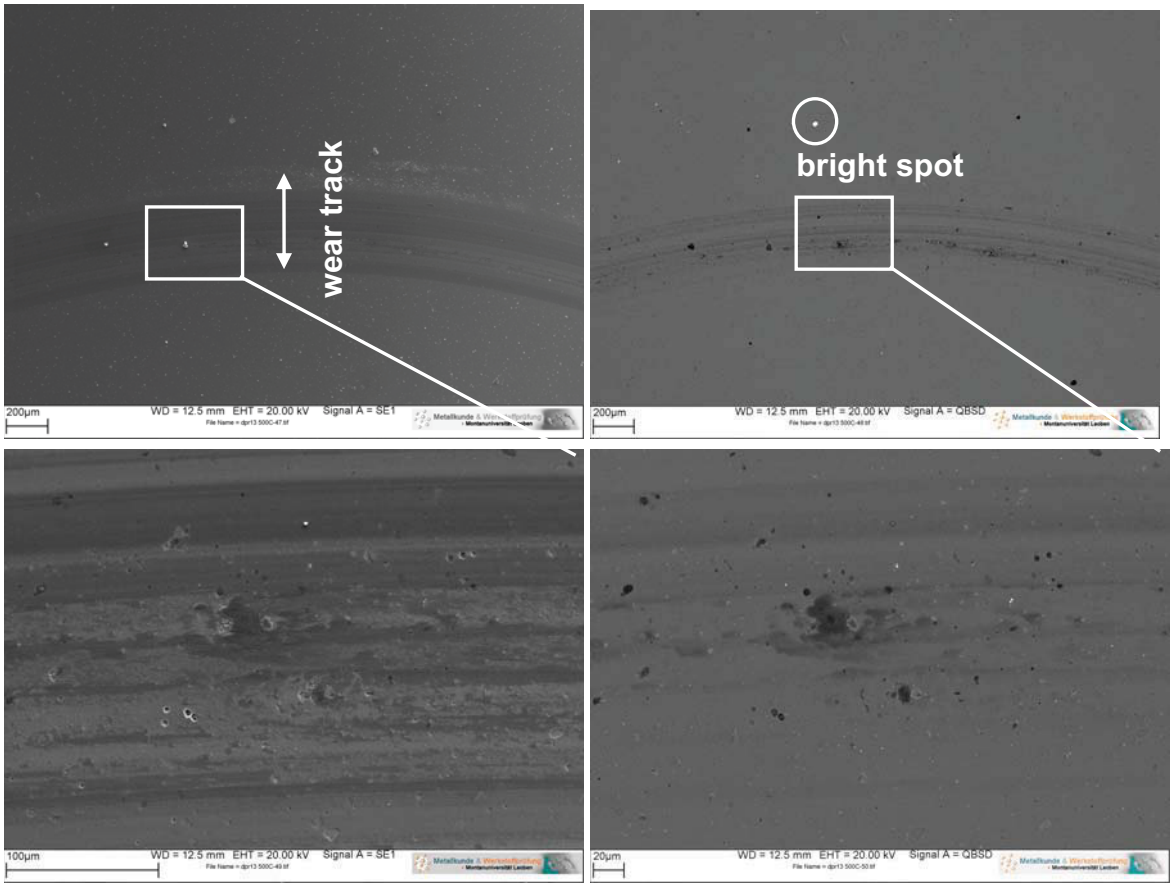

Figure 6.23: SEM micrographs in secondary electrons mode (left row) and QBSD mode (right row) of the wear track of the coating deposited from the $Ti_{31.7}Al_{63.3}Ta_5$ target at -160V bias voltage after tribologically testing at 500°C against alumina.

Moreover, 2-dimensional and 3-dimensional plots have been generated by the optical profilometer. All these illustrations are shown for the coating deposited from the $Ti_{31.7}Al_{63.3}Ta_5$ target for each bias voltage in Figure 6.24. The 2-dimensional (left row) and the 3-dimensional (middle row) pattern show a huge amount of attached material on the wear track at -40V. With increasing bias voltage, this amount decreases significantly and at a bias voltage of -160V less attached material can be detected. The QBSD micrographs (right row) again show the decreasing amount of attached material, namely oxides, with increasing bias voltage. The sample deposited at -160V bias voltage shows nearly no oxides attached in the wear track. Thus, Figure 6.24 indicates that the wear mechanism must have changed from adhesive to abrasive wear, which can be clearly seen in the 2- and 3-dimensional displays.

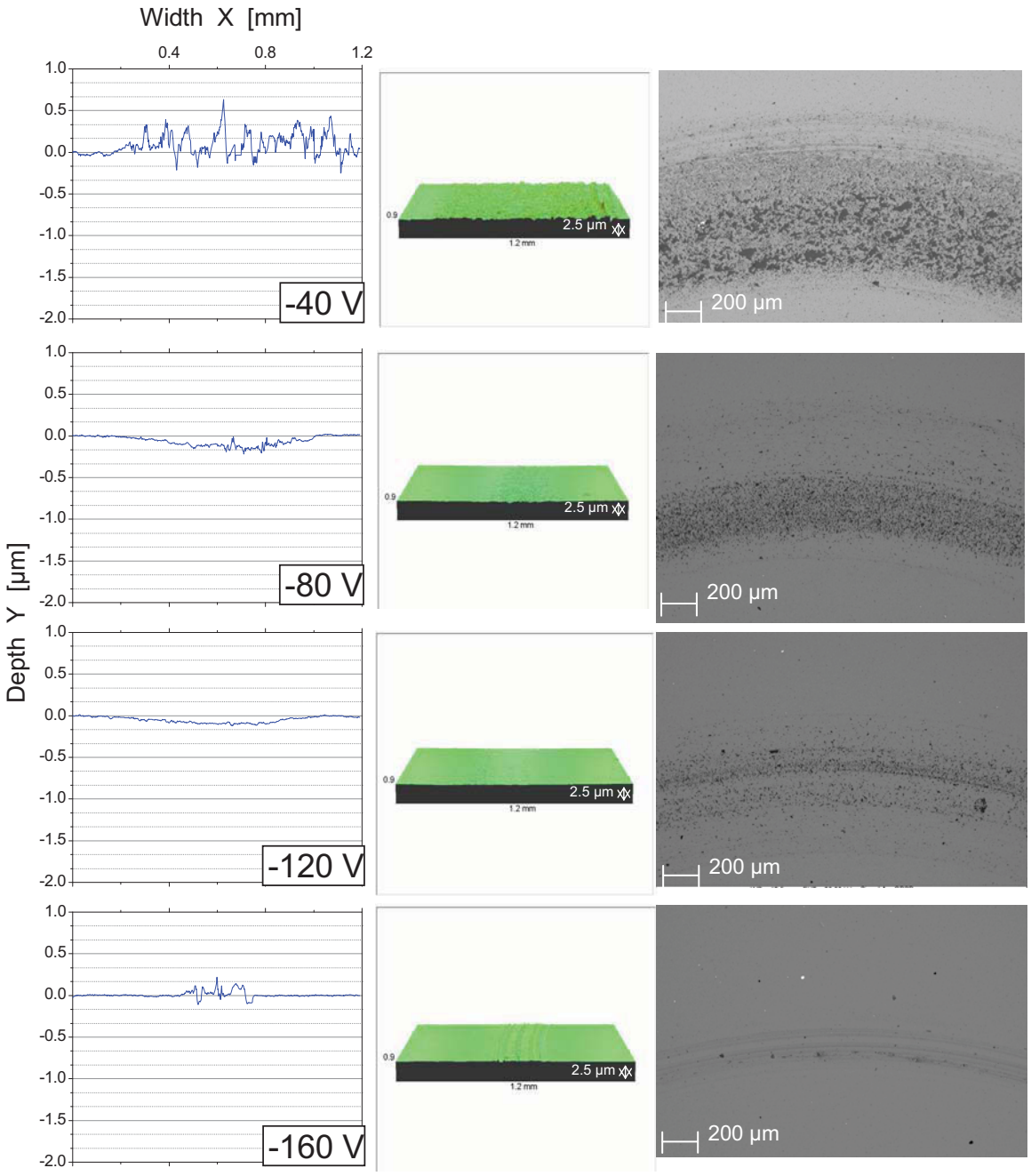

Figure 6.24: Characterization of the wear tracks on the coatings deposited from the $Ti_{31.7}Al_{63.3}Ta_5$ target with increasing bias voltage. The left row shows the 2-dimensional plot, the middle row the 3-dimensional plot. The right row shows the QBSD images of the wear tracks.

In addition, EDS scans have been performed on the sample deposited at -40V to determine the predominant elements in the wear track as well as on the coating surface. These scans are summarized in Figure 6.25. The yellow curve has been scanned on the surface outside of the wear track and the blue pattern represents the non-oxidic areas in the wear track. Both patterns show a very similar element composition of Ti, Al and a small amount of Ta. The green pattern, resulting from oxide areas in the wear track (dark areas in Figure 6.22), shows a huge amount of Al and O. Thus, the detected oxides can be identified as alumina, which most likely originates from the Alumina ball. The red line represents the element analysis of the bright spots on the surface, which have been observed in the QBSD image (see Figure 6.22). These spots could be identified as Ta rich areas.

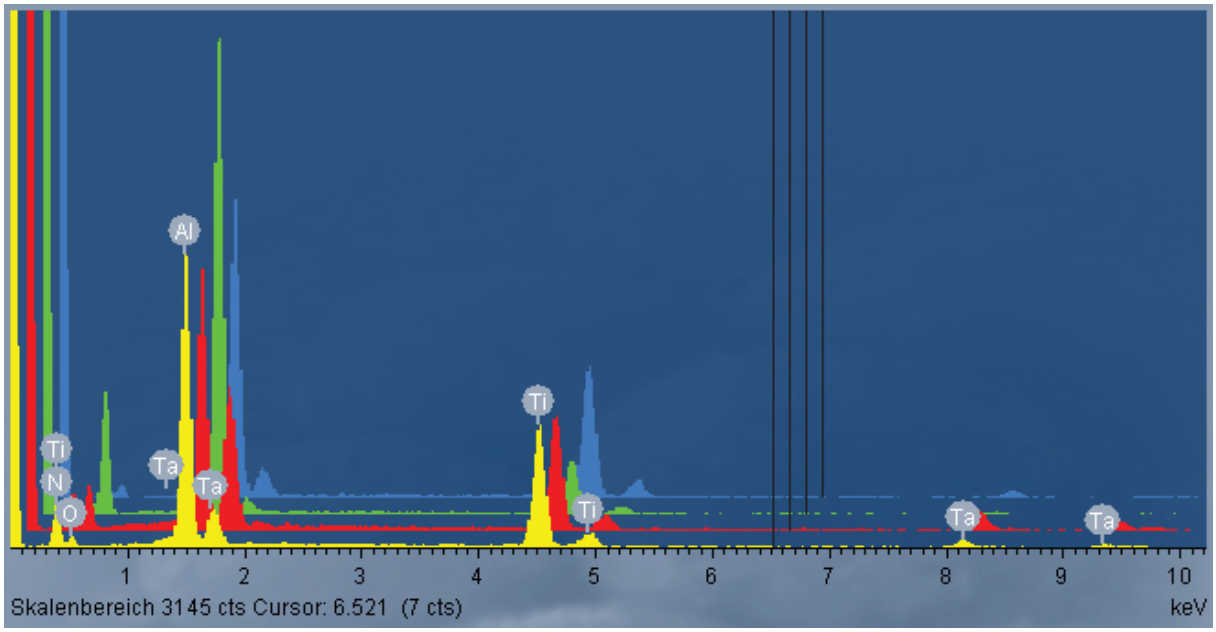

Figure 6.25: EDS analysis of the coating deposited from the $Ti_{31.7}Al_{63.3}Ta_5$ target at -40V bias voltage.
yellow.....coating surface outside the wear track
blue ….....non-oxidized areas in the wear track
green ……oxidized areas in the wear track
red …….Ta rich spots

The friction curves of the corresponding reference sample (Ti/Al =2.00) are shown in Figure 6.26. Only this coating system shows an increasing coefficient of friction with increasing bias voltage, i.e. from 0.87 (-40V) to 1.00 (-160V), while the scattering observed is similar to the other coating systems: huge scattering at -40V and low scattering at -160V. Additionally, SEM analyses have been done to get further information on the wear tracks. The micrographs in SE as well as QBSD mode are shown in Figure 6.27 for the sample deposited at -40V bias voltage and in Figure 6.28 for the sample deposited at -160V bias voltage. At -40V, a huge amount of

attached oxidic material can be detected, while at -160V only few oxides can be seen in the wear track.

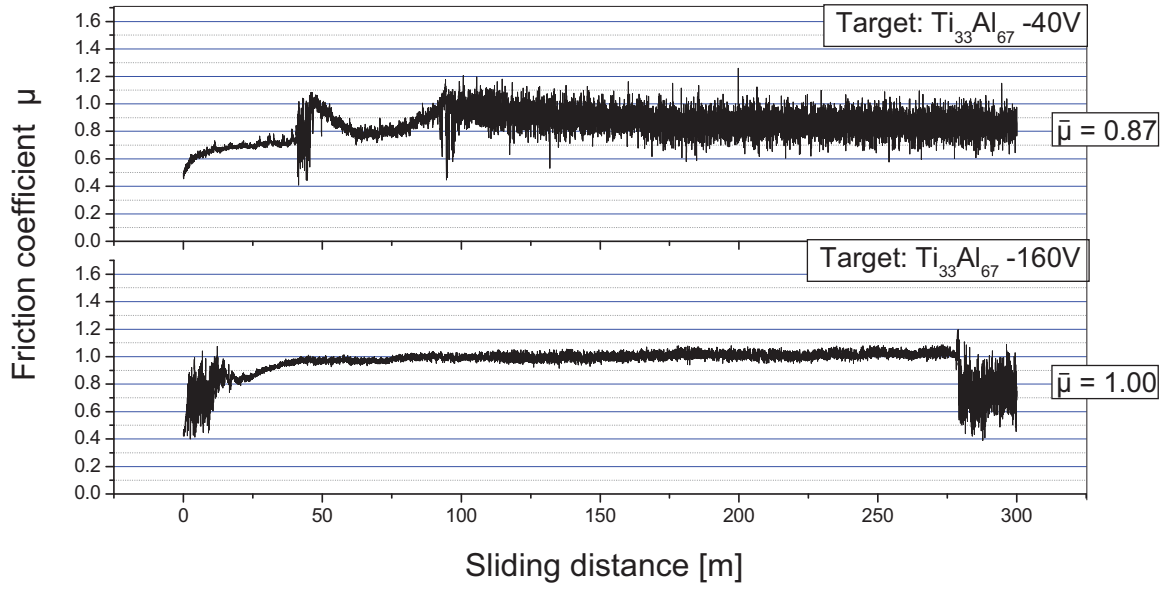

Figure 6.26: Friction curves of the coating deposited from the $Ti_{33}Al_{67}$ target at -40V and -160V bias voltage, tribological tested at 500°C against alumina.

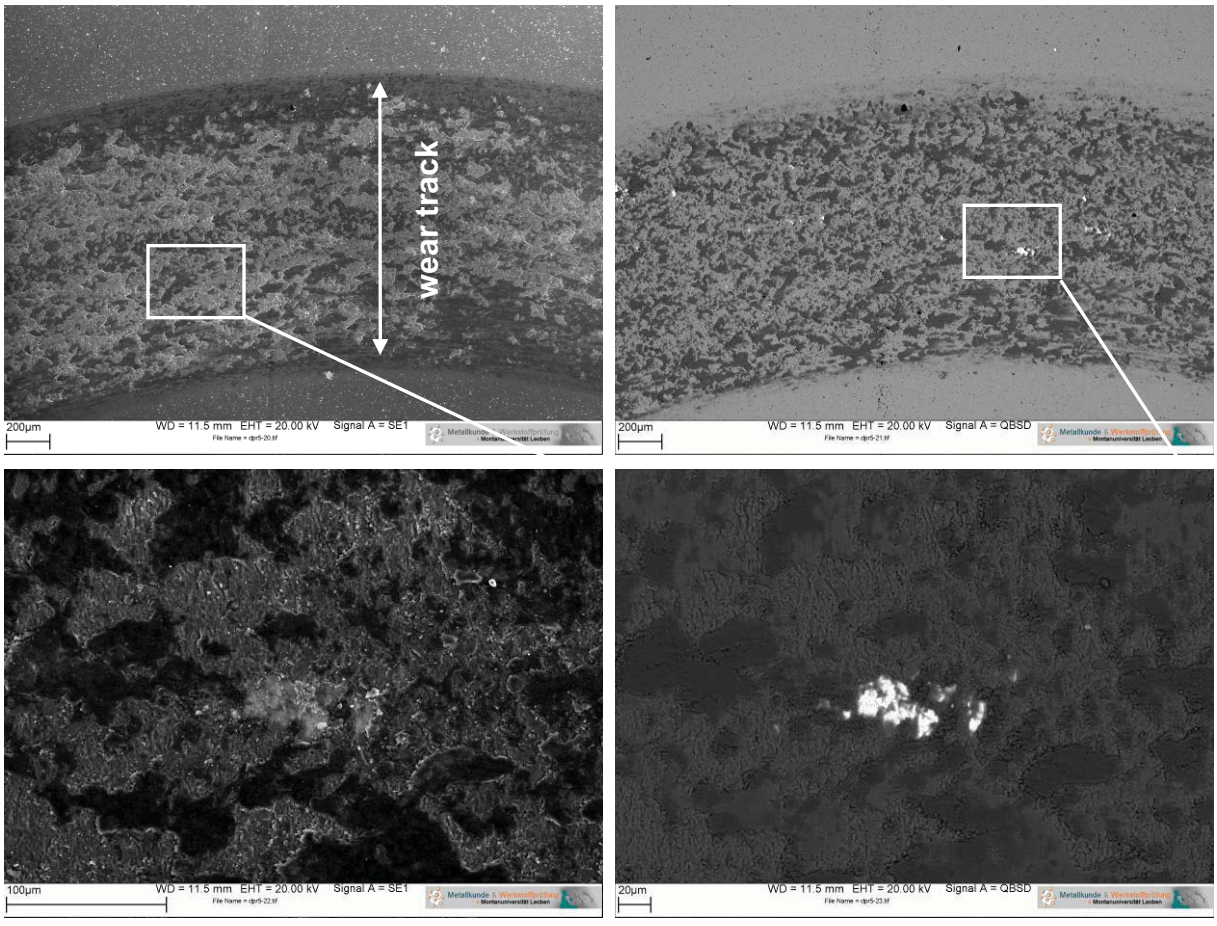

Figure 6.27: SEM micrographs in SE mode (left row) and QBSD mode (right row) of the wear track of the coating deposited from the $Ti_{33}Al_{67}$ target at -40V bias voltage after tribological testing at 500°C.

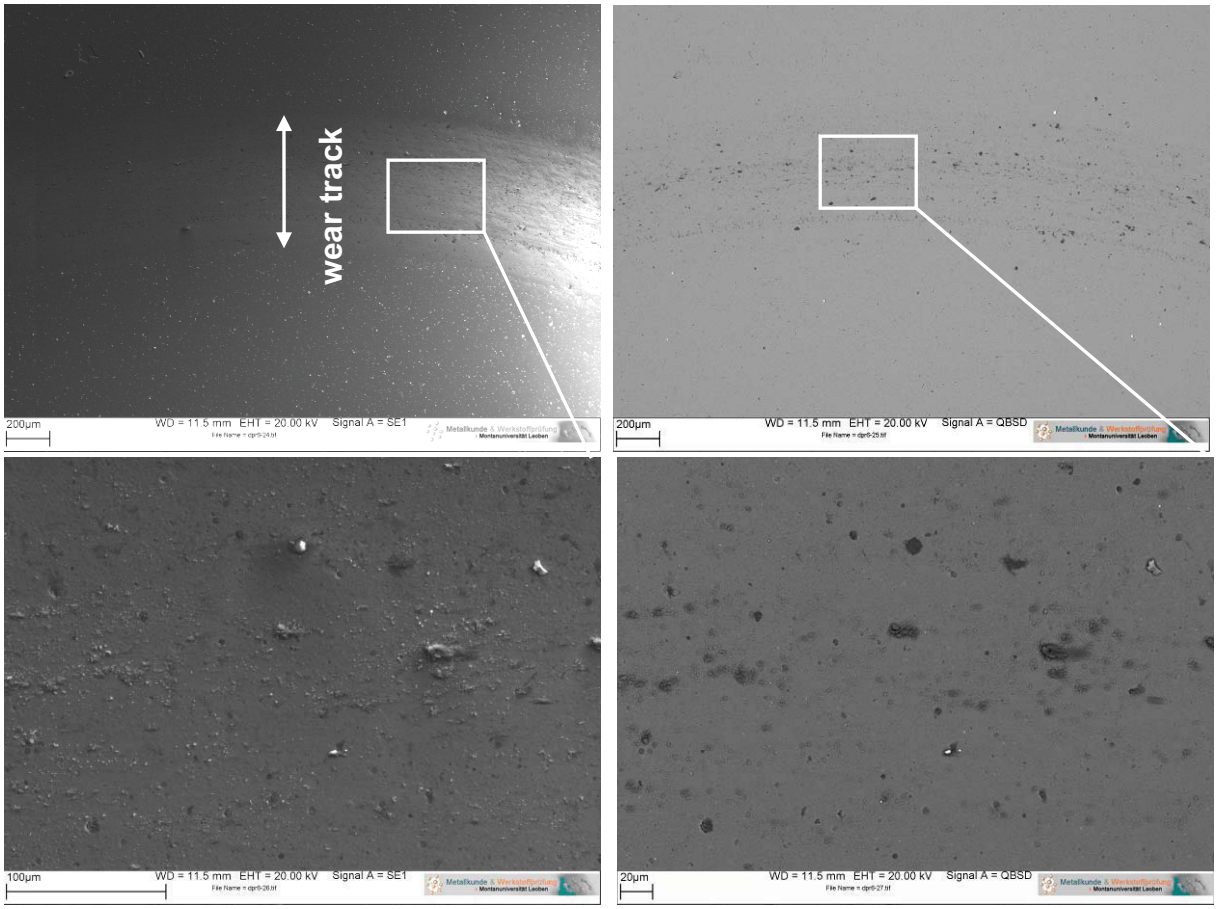

Figure 6.28: SEM micrographs in SE mode (left row) and QBSD mode (right row) of the wear track of the coating deposited from the $Ti_{33}Al_{67}$ target at -160V bias voltage after tribological testing at 500°C against alumina.

Generally, it is seen that in most coating systems the wear mechanism must have changed with increasing bias voltage. The high scattering and the huge amount of attached oxides in the wear track indicates that adhesive wear is the dominating wear mechanism at lower bias voltages. At higher bias voltages, instead of attached oxides in most coating systems ploughing was detected resulting in low scattering of the friction curve. Hence, it is suggested that abrasive wear is dominateing during tribological testing.

The wear behavior of all investigated films is summarized in Figure 6.29. Generally, the wear coefficients at 500°C are much lower compared to the from room temperature results. However, the trends over the different bias voltages show a similar behavior to the trends at room temperature. The coatings with lower Al content ($Ti_{40}Al_{60}$ and $Ti_{38}Al_{57}Ta_5$), which are dominated by the cubic phase even at lower bias voltage, show superior wear coefficients at -40V (-2.19 $.10^{-15}$ m^3/Nm) and -80V (-0.21 $.10^{-15}$ m^3/Nm). The low wear coefficient of $Ti_{40}Al_{60}$ at -40V may result from a longer heating time (2h 50min) than the others (1h 50min). It can be assumed that due to longer heating a thin oxide film has been formed, which improves the wear behavior. The coating systems, grown from the target with higher Al contents, show higher wear coefficients of -4.88 $.10^{-15}$ m^3/Nm in case of the Ta alloyed sample (Al/(Ti+Ta) = 1.72) and even a worse behavior in case of the reference sample (Ti/Al = 2.00) without Ta (-12.7 $.10^{-15}$ m^3/Nm) at lower bias voltages, due to the huge amount of hexagonal phase. With increasing bias voltage, the amount of hexagonal phase decreases in expense of the cubic phase and as a result the coefficient of wear strongly decreases. Obviously, the Ta containing coating shows a superior wear behavior even at low applied bias voltages compared to the coatings without Ta. Generally, at -160V all coating systems result in a similar wear coefficient of about -0.2 $.10^{-15}$ m^3/Nm. However, at this point it has to be mentioned, that especially at lower bias voltages SEM investigations displayed that a high amount of alumina, most probably from the ball, sticks in the wear track, minimizing the measured negative wear volume.

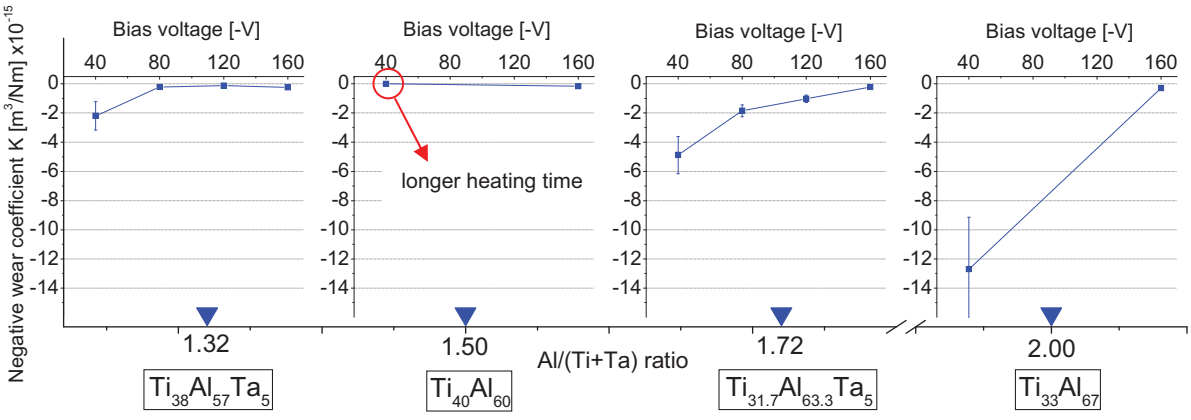

Figure 6.29: Negative wear coefficients as a function of the bias voltage for all coating systems tribologically tested at 500°C against alumina. The X-axis shows the corresponding Al/(Ti+Ta) ratios. The exact target compositions are given below the graphs.

6.6.3 Tribological Tests at 700°C

Finally, the friction and wear behavior has been investigated at a temperature of 700°C. The calculation of the average friction coefficients was difficult, since most of the friction curves at 700°C showed a very discontinuous friction behavior. As an example, the friction curves of the coatings deposited from the $Ti_{31.7}Al_{63.3}Ta_5$ target at different bias voltages are shown in Figure 6.30. At -40V bias voltage, a relatively constant coefficient of friction with narrow scattering is observed. However, after about 150m the coefficient increases from around 0.8 up to around 1.0, resulting in an average friction coefficient of 0.9. The friction coefficient of the coating deposited at -80V proceeds completely inconstant for about 180m, followed by a constant value with high scattering. Also the friction curves for -120V and -160V show a significant break after about 160 meters. Thus, the average friction coefficient has been calculated from the constant section of the curves, which is indicated by arrows in Figure 6.30. The reason for these breaks in the mentioned friction curves may be found in changing wear mechanism during the test run. Moreover, tribo-oxidation may play an important role at these temperatures.

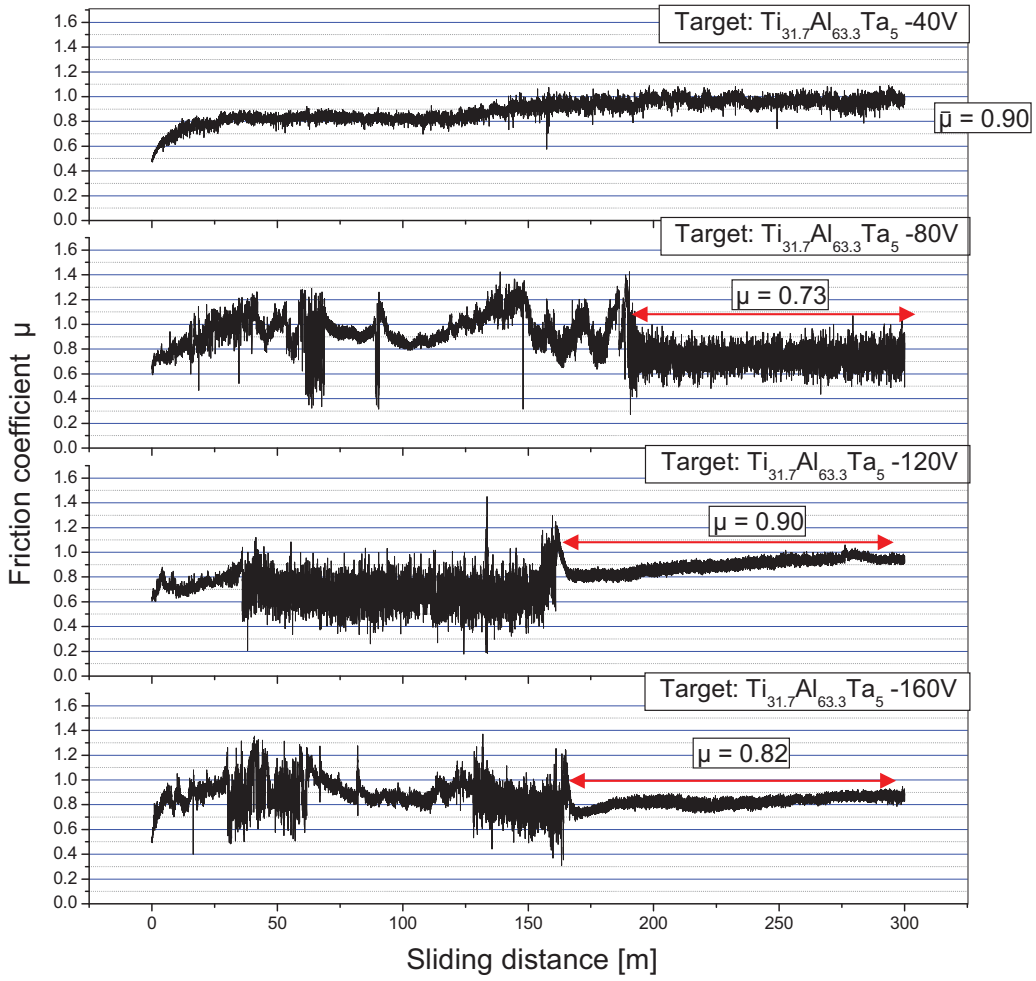

Figure 6.30: Friction curves of the coatings deposited from the $Ti_{31.7}Al_{63.3}Ta_5$ target at -40V, -80V, -120V and -160V bias voltage, tribologically tested at 700°C against alumina.

The friction curves of all other coating systems are shown in Figure 6.31 - Figure 6.33. Due to the discontinuous course of the friction coefficients, the overview given in Figure 6.34 only describes the ranges of occurring friction coefficients. Generally, both (Ti,Al)N coatings exhibit a higher friction coefficient at enhanced bias voltages, while the Ta containing coatings show a better friction performance with lower values at high bias voltages.

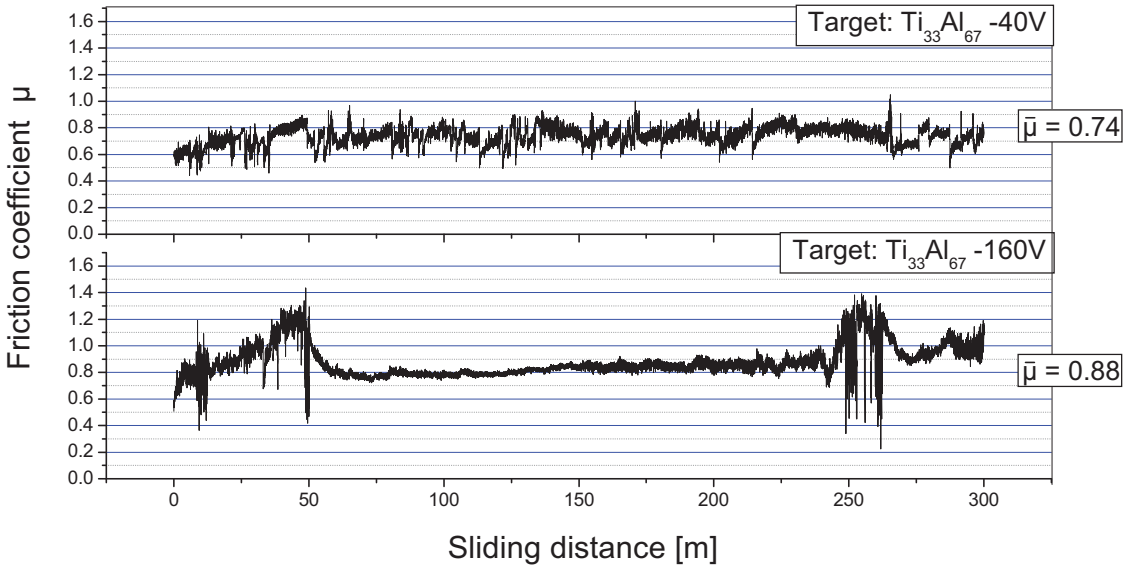

Figure 6.31: Friction curves of the coatings deposited from the $Ti_{33}Al_{67}$ target at -40V and -160V bias voltage, tribologically tested at 700°C against alumina.

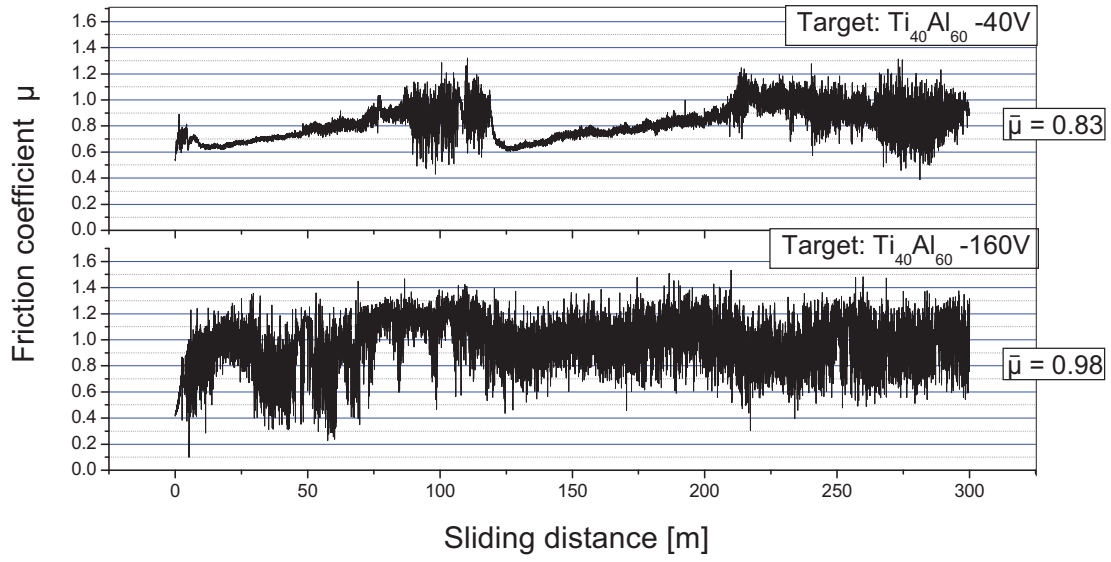

Figure 6.32: Friction curves of the coatings deposited from the $Ti_{40}Al_{60}$ target at -40V and -160V bias voltage, tribologically tested at 700°C against alumina.

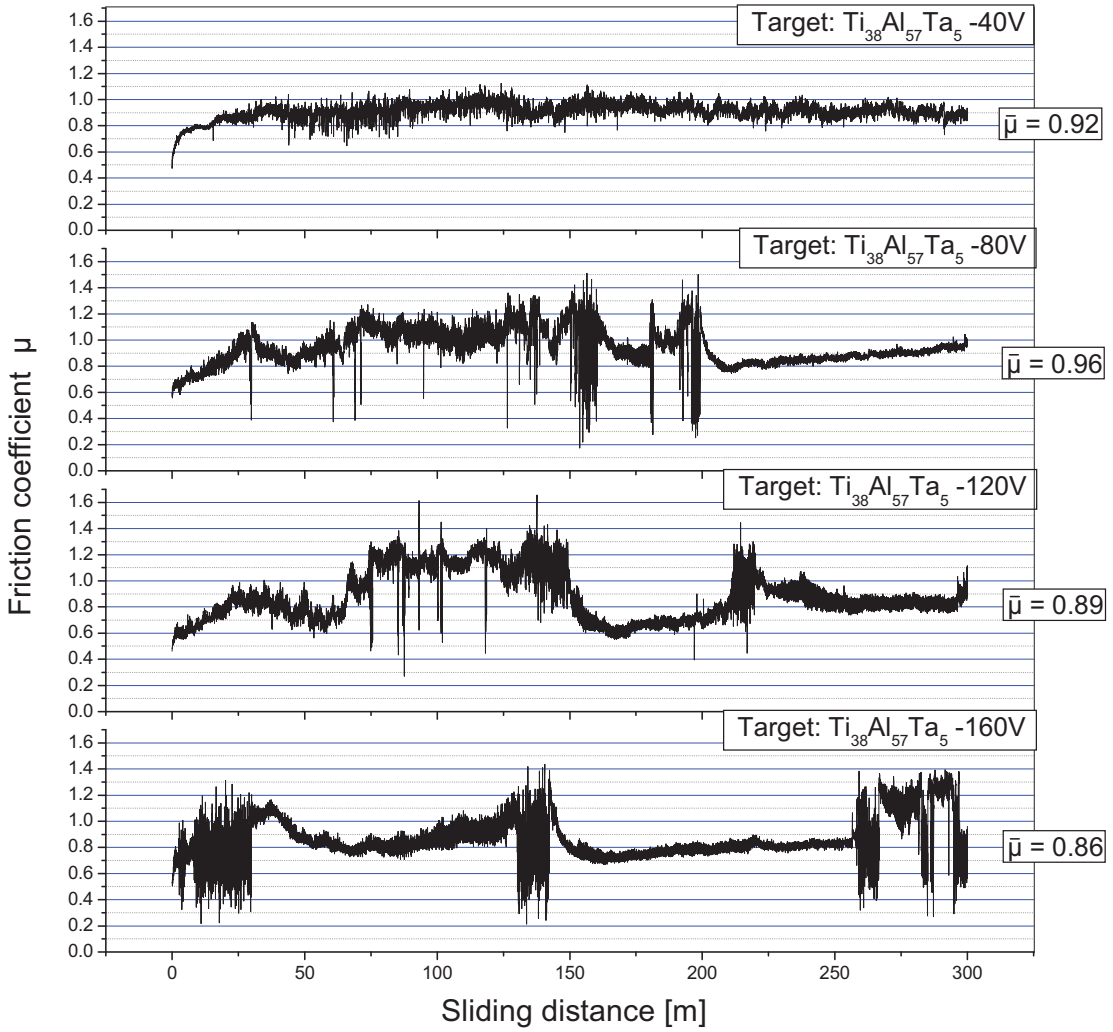

Figure 6.33: Friction curves of the coatings deposited from the $Ti_{38}Al_{57}Ta_5$ target at -40V, -80V, -120V and -160V bias voltage, tribologically tested at 700°C against alumina.

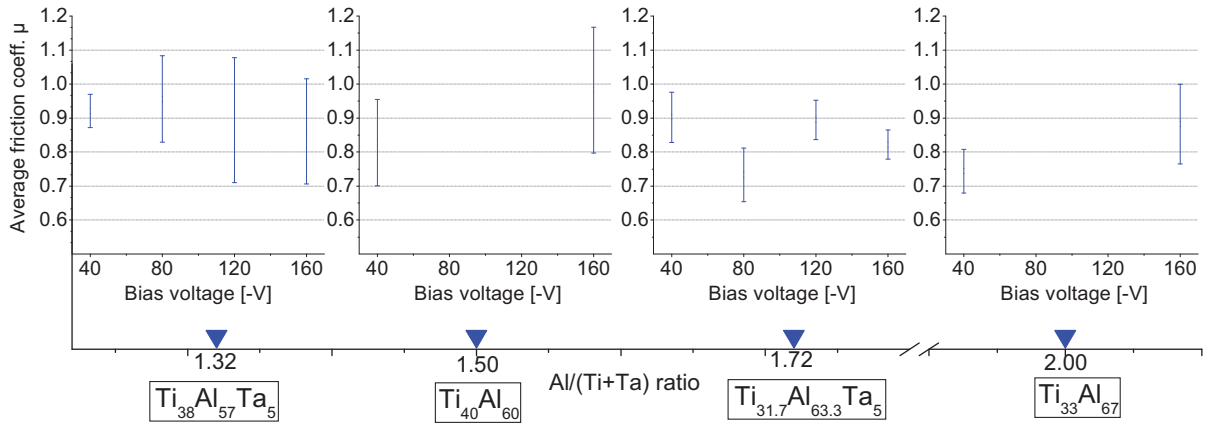

Figure 6.34: The friction coefficients of the coatings investigated as a function of the bias voltage tribologically tested at 700°C. In case of the $Ti_{31.7}Al_{63.3}Ta_5$ system the friction coefficients have been calculated from only short constant sections of the curves and therefore only the range of the estimated friction coefficients is shown. The target compositions are given below the graphs.

The wear performance of the investigated coating systems at 700°C was similar to the 500°C tests. The enhanced wear behavior may be correlated with a decreasing amount of the hcp phase in the films (Figure 6.35). The coatings with lower Al content (Al/(Ti+Ta) = 1.32 and 1.50) consist of only a low amount of hexagonal phase, thus, show a lower wear coefficient at low bias voltages, compared to the samples with higher Al content (Al/(Ti+Ta) = 1.72 and 2.00). With increasing bias voltage, the amount of hexagonal phase decreases, resulting in a distinct decreasing wear coefficient. The Ta alloyed coating with higher Al content ($Ti_{31.7}Al_{63.3}Ta_5$) is dominated by the hcp phase at -40V, thus, showing the worst wear behavior. At -80V and -120V, the microstructure of this coating consist predominately of fcc-(Ti,Al,Ta)N. This transition causes a significantly improved wear performance. At -160V, this Ta containing coating system shows the best wear coefficient (about -0.23 $.10^{-15}$ m^3/Nm), while all other coatings show a two times higher wear coefficient at -160V (around -0.5 $.10^{-15}$ m^3/Nm). Generally, it is demonstrated that an enhanced bias voltage improves the wear behavior of all investigated coating systems. As mentioned above, this can be correlated with the microstructure, however, tribo oxidational effects have to be taken in account.

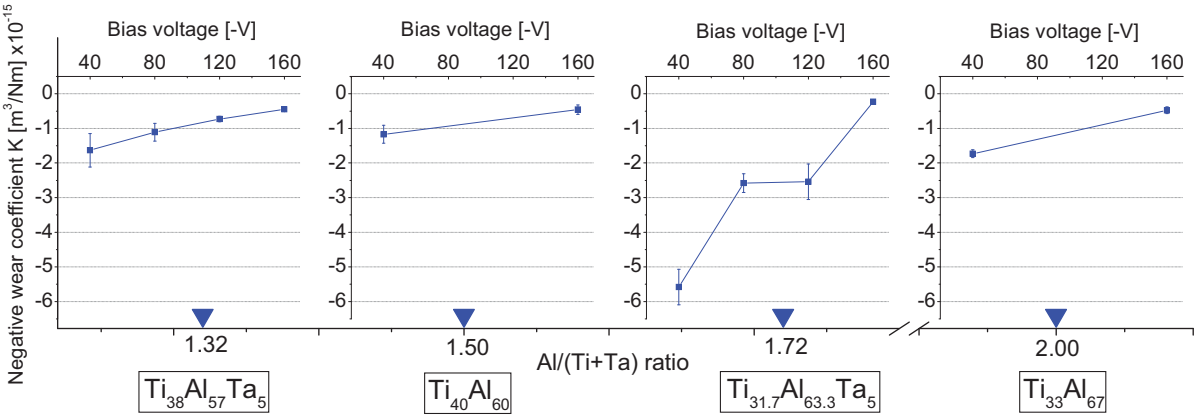

Figure 6.35: Negative wear coefficients as a function of the bias voltage for all coating systems, tribologically tested at 700°C against alumina. The X-axis shows the corresponding Al/(Ti+Ta) ratios. The exact target compositions are given below the graphs.

Moreover, a detailed illustration of the wear tracks of the coating deposited from the $Ti_{31.7}Al_{63.3}Ta_5$ target after running the tribo-test is seen in Figure 6.36, showing the 2- and 3- dimensional views of the wear tracks and SEM micrographs. The coating deposited at -40V bias voltage shows a significant wear track with a depth of more than 1.5 µm compared to the coating systems deposited at higher bias voltages (-80V and -120V). Here, the wear track depths are between 0.25 µm and 0.6 µm. The

sample deposited at -160V bias voltage shows an even lower depth of the wear track, about 0.15 µm and a great amount of attached material, which can be identified as oxides in the QBSD micrograph (right row). Generally, the QBSD micrographs show that the amount of attached oxides increases with increasing bias voltage. Hence, the different wear mechanisms of abrasive wear for -40V and dominating adhesive wear for higher bias voltages can be seen.

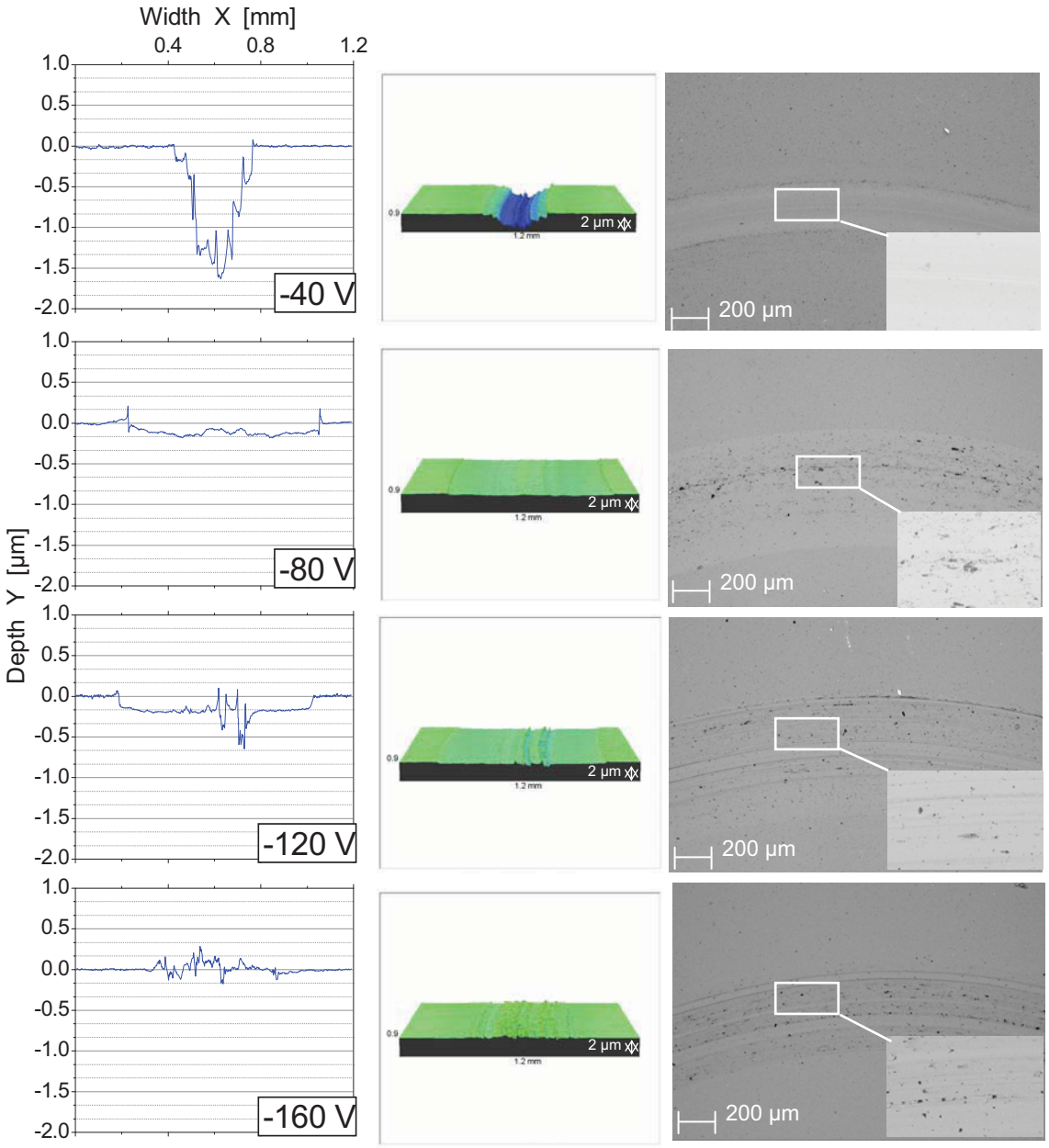

Figure 6.36: Characterization of the wear track on the coatings deposited from the $Ti_{31.7}Al_{63.3}Ta_5$ target with increasing bias voltage. The left row shows the 2-dimensional plot, the middle row the 3-dimensional plot. The right row shows the QBSD images of the wear tracks

7 Conclusions

Within this thesis, the structural, mechanical and tribological properties of (Ti,Al)N and (Ti,Al,Ta)N coatings have been investigated. The films were deposited by cathodic arc evaporation in an industrial scale facility from targets containing two different Al/Ti ratios (1.5 and 2) and 5 at% Ta in case of Ta containing coatings. Different coating systems have been deposited using several bias voltages (-40, -80, -120 and -160 V) in the different deposition runs.

The film compositions showed significant differences (up to 5.7 at%) of the Al and Ti contents in the film compared to the target. In case of the Ta containing coatings, the Ta content in the films (i.e. 1.7 ÷ 1.9 at% Ta) is much lower than in the target (5 at% Ta).

Microstructural analyses showed that both, the (Ti,Al,Ta)N and (Ti,Al)N systems, deposited at the lowest bias voltage of -40 V consist of two phases, the fcc-$Ti_{1-x}Al_x$(Ta)N and the hcp-$Ti_{1-x}Al_x$(Ta)N. Moreover, at higher Al content (Al/Ti ratio = 2) the amount of hcp-$Ti_{1-x}Al_x$(Ta)N increases. With increasing bias voltage, the amount of hexagonal phase strongly decreases, and especially for the coatings with Al/Ti ratio of 2 the preferred orientation changes from (200) to (111) and (220). All coatings deposited at -160V bias voltage show a predominant fcc phase structure. These structural transitions affect the microhardness of the films. Especially (Ti,Al,Ta)N coatings showed superior hardness values up to 32 GPa at bias voltages of -120 and -160 V compared to the (Ti,Al)N reference samples (23 - 30 GPa) These high values result on one hand from solid solution hardening effects, due to the incorporation of Ta atoms in the $Ti_{1-x}Al_xN$ cell. On the other hand, structural investigations showed a shift to a more pronounced fcc phase structure with the incorporation of Ta.

For all coating systems, significantly scattering friction coefficients between 0.7 and 1.0 at room temperature were obtained. Since all samples with low Al content (Al/Ti = 1.5) yielded low wear values at room temperature between 10.10^{-15} and 14.10^{-15} m³/Nm, the wear behavior of the coatings with higher Al content (Al/Ti = 2) seems to depend strongly on the microstructure. The wear coefficient of the Ta containing sample, for example, decreased from $-24.2 .10^{-15}$ to $-13.5 .10^{-15}$ m^3/Nm between -40 and -160 V bias voltage. This may be explained by the decreasing amount of hexagonal phase.

The tribological tests at 500°C displayed friction coefficients of all coating systems deposited at -40, -80 and -120 V between 0.8 and 1.0, while, especially for the Ta containing films deposited at -160V bias voltage, lower friction coefficients of 0.66 to 0.71 were reached. All coating systems showed high scattering of the friction curves

at low bias voltages, which decreases with higher bias voltages. SEM analyses revealed a huge amount of attached alumina, most likely from the ball, sticking in the wear track of the samples deposited at low bias voltages, while for the samples deposited at higher bias voltage this amount as well as the wear track depth significantly decreases. This indicates different wear mechanisms, occurring at different bias voltages. This transition between the two wear mechanisms depends on the different applied bias voltage in the coating systems. However, the wear behavior could be significantly improved in all coating systems with increasing bias voltage.

During tribological testing at 700°C, very discontinuous friction curves occur, also indicating different wear mechanisms during testing. Thus, no mean friction values could be calculated. Similar to the tribological tests at 25 and 500°C, the wear behavior seems to strongly depend on the bias voltage i.e. the amount of hexagonal phase in the film. Thus, the negative wear coefficient decreases with increasing bias voltage, resulting in superior wear coefficients of about 0.5 $.10^{-15}$ m^3/Nm for all coating systems deposited at -160 V bias voltage.

Thus, the results within this thesis show a positive influence of the increased bias voltage on the mechanical and tribological properties, especially at higher temperatures. The results obtained clearly provide evidence that it is possible to improve the properties of (Ti,Al)N coatings by alloying Ta as well as by adjusting the bias voltage during deposition.

References

[1] **S. PalDey, S.C. Deevi**, Mater. Sci. Eng. A342 (2003) 58.

[2] **K. Kutschej, P.H. Mayrhofer, M. Kathrein, P. Polcik, C. Mitterer**, Surf. Coat. Technol. 200 (2005) 113.

[3] **J. Patscheider, T. Zehnder, M. Diserens**, Surf. Coat. Technol. 146 –147 (2001) 201.

[4] **P.H. Mayrhofer**, Lecture Script Materials Science of Hard Coatings, University of Leoben (2004).

[5] **R.F. Bunshah**, Deposition Technologies for Films and Coatings, Noyes Publications, New Jersey (1982).

[6] **R.A. Haefer**, Oberflächen und Dünnschicht-Technologie, Teil I, Springer Verlag, Berlin (1987).

[7] **R.K. Waits**, J. Vac.Sci. Technol. A19 (2001) 1666.

[8] **Fr.-W. Bach, T Duda**, Moderne Beschichtungsverfahren, Wiley-VCH, Weinheim (2000).

[9] **D. L. Smith**, Thin Film Deposition, McGraw-Hill, USA (1995).

[10] **B. Rother, J. Vetter**, Plasma-Beschichtungsverfahren und Hartstoffschichten, Dt. Verlag für die Grundstoffindustrie, Leipzig (1992).

[11] **I. Petrov, P.B. Barna, L. Hultman, J.E. Greene**, J. Vac. Sci. Technol. A21/5 (2003) 117.

[12] **A. Anders**, Surf. Coat. Technol. 120-121 (1999) 319.

[13] **E.S. Machlin**, Materials Science in Microelectronics, Giro Press, New York, (1995).

[14] **D.S. Rickerby, P.J. Burnett**, Thin Solid Films 157 (1988) 195.

[15] **P.H. Mayrhofer**, Materials Science Aspects of Nanocrystalline PVD Hard Coatings, PhD-Thesis, University of Leoben (2001).

[16] **K.L. Lin, M.Y. Hwang, C.D. Wu**, Mater.Chem. Phys. 46 (1996) 77.

[17] **J.L. Vossen**, Thin Film Processes II, Acad. Press, Boston (1991).

[18] **M. Pfeiler**, The influence of deposition temperature on $Ti_{1-x}Al_xN$ coated heat resistant high speed steels, Diploma thesis, University of Leoben (2005).

[19] **D.M. Sanders, A. Anders**, Surf. Coat. Technol. 133-134 (2000) 78.

[20] **H. Fischmeister, H.-A. Jehn**, Hartstoffschichten zur Verschleißminderung, DGM Informationsgesellschaft Verlag, Oberursel (1987).

[21] **J.A. Thornton**, Ann.Rev. Mater. Sci. 7 (1977) 239.

[22] **B.A. Movchan, A.V. Demchishin**, Phys. Met. Metallogr. 28 /4 (1969) 83.

[23] **J.A. Thornton**, J. Vac. Sci. Technol. 11(4) (1974) 666.

[24] **R. Messier, A.P. Giri, R.A. Roy**, J. Vac. Sci. Technol. A 2/2 (1984) 500.

[25] **B. Bhushan**, Handbook of Micro/Nano Tribology 2nd edition, CRC Series, Boca Raton, FL (1995).

[26] **DIN 50281**, Materialprüfnormen für metallische Werkstoffe 2, Beuth Verlag, Berlin (1983).

[27] **N. Suh, H. Sin**, Wear 69 (1981) 91.

[28] **B. Bhushan**, Principles and Applications of Tribology, John Wiley, New York (1999).

[29] **E. Rabinowicz**, Friction and Wear of Materials, 2nd edition, John Wiley, New York (1995).

[30] **K. Holmberg, A. Matthews**, Coatings Tribology, Properties, Techniques and Applications in Surface Engineering, Elsevier, Amsterdam (1994).

[31] **A.N. Kalea, K. Ravindranath, D.C. Kotharia, P.M. Raole**, Surf. Coat. Technol. 145 (2001) 60.

[32] **F.-R. Weber, F. Fontaine, M. Scheib, W. Bock**, Surf. Coat. Technol. 177-178 (2004) 227.

[33] **O. Knotek, A. Barimani, B. Bosserhoff, F. Löffler**, Thin Solid Films 193/194 (1990) 557.

[34] **J.C. Schuster, J. Bauer**, J. Solid State Chem. 53 (1984) 260.

[35] **H. Holleck**, Surf. Coat. Technol. 36 (1988) 151.

[36] **P.H. Mayrhofer, D. Music, J.M. Schneider**, J. Appl. Phys. 100 (2006) 094906

[37] **A. Kimura, H. Hasegawa, K. Yamada, T. Suzuki**, Surf. Coat. Technol. 120-121 (1999) 438.

[38] **A. Hörling, L. Hultman, M. Oden, J. Sjölen, L. Karlsson**, J. Vac. Sci. Technol. A 20 (2002) 1815.

[39] **P. H. Mayrhofer, A. Hörling, L. Karlsson, J. Sjölen, T. Larsson, C. Mitterer, L. Hultman**, Appl. Phys. Let. 83 (2003) 2049.

[40] **M. Zhou, Y. Makino, M. Nose, K. Nogi**, Thin Solid Films 339 (1999) 203.

[41] **G. Gottstein**, Physikalische Grundlagen der Materialkunde, 2. Auflage, Springer Verlag, Berlin (2001).

[42] **R. W. Cahn, P. Haasen**, Physical Metallurgy, Elsevier, Amsterdam (1996).

[43] **P. Haasen**, Physical Metallurgy, Cambridge University Press, London (1978).

[44] **R. W. Siegel, G. E. Fougere**, Nanostr. Mat. 6 (1995) 205.

[45] **H. Hahn, K.A. Padmanabhan**, Nanostr. Mat. 6 (1995) 191.

[46] **J. Musil, H. Hrubý**, Thin Solid Films 365 (2000) 104.

[47] **J. Schiøtz**, Proceeding of the 22nd Riso International Symposium on Materials Science, Roskilde, Denmark (2001) 127.

[48] **O. Knotek, M.Böhmer, T. Leyendecker, F. Jungblut**, Mater. Sci. Eng. A105-106 (1988) 481.

[49] **D. McIntyre, J.E. Greene, G. Hakansson, J.-E. Sundgren, W.-D. Münz**, J. Appl. Phys 67 (1990) 1542.

[50] **W.-D. Münz**, J. Vac. Sci. Technol. A4 (1986) 2717.

[51] **Kwang-Lung Lin, Ming-Yeong Hwang, Cheng-Dau Wu**, Mat. Chem. Phys. 46 (1996) 77.

[52] **O. Knotek, W.D. Münz, T. Leyendecker**, J. Vac. Sci. Technol. A 5 (1987) 2173.

[53] **O. Knotek, M. Böhmer, T. Leyendecker**, J. Vac. Sci. Technol. A 4 (1986) 2695.

[54] **J. Gühring, J. Ebberink, T. Leyendecker**, Ind.-Anz. 65-66 (1989) 68.

[55] **K. Kutschej, P.H. Mayrhofer, M. Kathrein, P. Polcik, C. Mitterer**, Surf. Coat. Techn. 188-189 (2004) 358.

[56] **I. J. Smith, W.D. Münz, L.A. Donohue, I. Petrov, J.E. Greene**, Surface Eng. 14 (1) (1998) 37.

[57] **O. Knotek, F. Löffler, G. Krämer**, Int. J. Refractory Metals Hard Mater. 14 (1996) 195.

[58] **A. Niederhofer, P. Nesládek, H.-D. Maennling, K. Moto, S. Veprěk, M. Jílek**, Surf. Coat. Technol. 120–121 (1999) 173.

[59] **S. Veprěk, S. Reiprich**, Thin Solid Films 268 (1995) 64.

[60] **K. Kutschej, P. H. Mayrhofer, M. Kathrein, C. Michotte, P. Polcik, C. Mitterer**, Proceedings of the 16th International Plansee Seminar, Reutte (2005), 774.

[61] **Balzers** RCS Coating System, Advertisment from *www.oerlikon.com*

[62] **Balzers** RCS Coating System Documentation 3rd edition (2004).

[63] **K. Nitsche**, Schichtmesstechnik, Vogel Buchverlag (1997).

[64] **B.D. Cullity**, Elements of X-Ray Diffraction 2nd edition, Addison-Wesley, Reading, Mass. (1978).

[65] **M. Birkholz**, Thin Film Analysis by X-Ray Scattering, Wiley-VHC, Weinheim (2006).

[66] **Fischerscope** H100C, Operating Manual, Hünenberg (2002).

[67] **H.-H. Behncke**, Härterei-Technische Mitteilungen 48 (1993).

[68] **C. Heermant, D. Dengel**, Materials Testing 38 (1996).

[69] **Veeco** – Metrology Group, WYCO NT1000 Setup Guide Tucson (2000).

[70] **Veeco** – Metrology Group, WYCO Surface Profilers Technical Reference Manual Tucson (1999).

[71] **M. Zeccino**, Characterizing Surface Quality: Why Average Roughness is Not Enough, Veeco - Metrology Group, USA (2006) *www.veeco.com.*

[72] **K. Kutschej, N. Fateh, P.H. Mayrhofer, M. Kathrein, P. Polcik, C. Mitterer**, Surf. Coat. Technol. 200 (2005) 113.